Chiral Metamaterials

Von der Fakultät Chemie der Universität Stuttgart
zur Erlangung der Würde eines Doktors der
Naturwissenschaften (Dr. rer. nat.) genehmigte Abhandlung

vorgelegt von

Sahand Eslami

aus Florenz

Hauptberichter:	Prof. Dr. Peer Fischer
Mitberichter:	Prof. Dr. Joris van Slageren
Prüfungsvorsitzender:	Prof. Dr. Guido Schmitz

Tag der mündlichen Prüfung: 29. April 2016

Max Planck Institut für Intelligente Systeme

Institut für Physikalische Chemie der Universität Stuttgart

2016

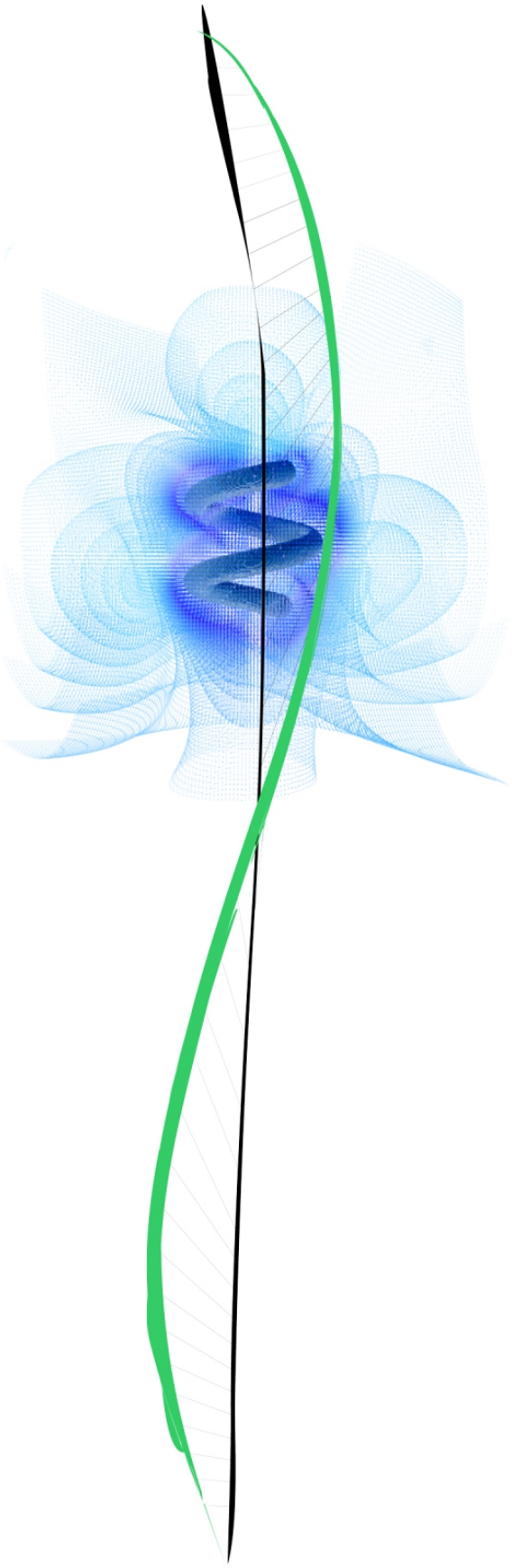

Zusammenfassung

Ich arbeite seit dem September des Jahres 2012 in der Forschungsgruppe Mikro-, Nano- und Molekulare Systeme des Max-Planck-Instituts in Stuttgart. Die Forschungsgruppe hat zuletzt eine Technik zur physikalischen Gasabscheidung verbessert, die auch als Glanzwinkeldeposition bekannt ist. Diese Technik ermöglicht die gleichzeitige Ausbreitung von Nanostrukturanordnungen auf nano-strukturierten Substraten via mizellarer Blockcopolymer-Nanolithographie mit einer programmierbaren, dreidimensionalen Kontrolle über die Formgebung in einem Maßstab im Nanometerbereich.

Aus der breiten Auswahl an Materialien, die mit dieser Technik angeordnet werden können, weisen Metalle einzigartige Eigenschaften in ihrer Interaktion mit elektromagnetischen Feldern auf. Die Plasmaresonanzen, die durch die hohe Dichte freier Elektronen hervorgerufen werden, können dazu genutzt werden, die Interaktion mit optischen Wellen zu intensivieren. Als Teil meiner Promotion habe ich die Effekte der Lichtabsorption mit zirkularer Polarisation auf kolloidalen Suspensionen und Beschichtungen untersucht, die als Anordnung spiralförmiger Nanopartikel auftreten, welche durch die Nutzung von plasmon aktive Metallen angeordnet werden. Wir haben gezeigt, dass diese Nanopartikel sehr ausgeprägte chirooptische Eigenschaften haben können. Mithilfe spezifischer Anordnungen verschiedener Metalle wie Gold, Silber und Kupfer können diese spektral justiert werden. Hierzu werden die geometrischen Formparameter der spiralförmigen Nanostrukturen der verwendeten Metalle angepasst.

Des Weiteren habe ich das Zusammenspiel von Magnetismus und Plasmonen untersucht. Da die Streuung freier Elektronen und das ferromagnetische Feld in der selben größen ordnung liegen, wird der Eintritt interessanter Phänomene erwartet. Es ist mir gelungen, ein Metamaterial herzustellen, in dem zum ersten Mal die Präsenz eines magnetochiralen Dichroismus in Raumkonditionen nachgewiesen werden konnte.

Das finale Ziel zukünftiger Forschungsprojekte in diesem Bereich wäre es festzustellen, ob die dünnen Filme plasmonischer Nanohelices dazu verwendet werden können, ein Metamaterial herzustellen, das einen negativen Brechungsindex für sichtbares Licht hat.

List of symbols and abbreviations

L-,$\mathscr{L}$-/R-,$\mathscr{R}$-	left/right handed
OR	optical rotation
ORP	optical rotatory power
CB	circular birefringence
CD	circular dichroism
CP	circular polarization
NCD	natural circular dichroism
MCD	magnetic circular dichroism
MChD	magneto-chiral dichroism
i	imaginary unit
`	complex variable
$\Re$ / $'$	real component of a complex number
$\Im$ / $''$	imaginary component of a complex number
GLAD	glancing angle deposition
DDA	dipole-dipole approximation
UV	ultra-violet
VIS	visible

IR	infra-red
$\times$	vector multiplication
$\cdot$	scalar multiplication
$\vec{}$	3-dimensional vector
$\leftarrow$	3x3 tensor
∇	3-dimensional vector gradient operator
$\Box$	d'Alembert or wave operator
$\rightarrow$	variable substitution
ϵ_0	vacuum permittivity
μ_0	vacuum permeability
c	speed of light in vacuum
SmA	smectic-A phase
π	Pitagora's constant
μ-	micro-, 10^{-6}
n-	nano-, 10^{-9}
°C	Celsius degrees
°K	Kelvin degrees
ppm	1 part per million
NP	nano-particle
σ	electrical conductivity or scattering cross section
Q	efficiency of a cross section
FFT	fast-Fourier transformation

CCG	complex conjugate gradient optimization method
BCML	block copolymer micellar nano-lithography
I	intensity of an electromagnetic wave
SEM	scattering electron microscopy
TEM	transmission electron microscopy or transverse electric mode
KK	Kramers-Kronig
laser	light amplification by stimulated emission of radiation
HWP	half-wave plate
QWP	quarter-wave plate
LC/LCC	liquid crystal/ LC compensator
BD	beam displacer
SQUID	superconducting quantum interference device
HAADF	high angle annular dark field
PMT	photo-multiplier tube

Contents

Preface

Chirality

"I call any geometrical figure, or group of points, 'chiral', and say that it has chirality if its image in a plane mirror, ideally realized, cannot be brought to coincide with itself", Lord Kelvin [1]

Chirality is a geometrical property. Something which is chiral is not invariant under parity, and can be distinguished in its left (L-) and right (R-) handed enantiomers.

The fundamental forces of the universe are not invariant under parity [2, 3] and life itself is also not. In fact, almost all biological matter is made of L-amino acids and R-sugars. Parity violation in the weak force may be the reason for homochirality of life on Earth, but this is still being debated as the force is very weak [4]. Most theories of the chirality of life assume that homochirality is a combination of chance and self amplification.

In terms of biological functionality, two enantiomers of the same molecule can present quite remarkable differences. The enantiomer of a chiral molecule may bind differently to a receptor and present different effects. In case of drugs it may be then of crucial importance which one of the enantiomers is present [5]; as an example, one enantiomer of ethambutol is used for the treatment of tubercolosis while the other enantiomer causes blindness [6].

Which methods do we have to differentiate between two enantiomers of the same molecule? One way to analyse and to be able to distinguish between two enantiomers is by their response to light and in particular to

polarized light, which is the basis for optical activity phenomena. However, the interaction of chiral molecules with polarized light is generally weak. Much larger chiroptical effects can be seen in artificial chiral nanostructures, which are the focus of this thesis.

Optical activity

Optically active materials are known since the beginning of the 19th century as materials that are capable of introducing a rotation of the plane of polarization of a linearly polarized beam [7]. However the optical rotation (OR) is only one of the optical activity phenomena which in general should be related to the sensitivity of a material to interact with different states of polarization. Of particular interest is the information about the three dimensional microscopic charge distributions in the structure of matter that can be probed by optical means and plays an important role in chemistry and biochemistry.

The absorption and refraction of electromagnetic waves can be described with the complex material-dependent index of refraction ($\tilde{n} = n' + in''$). A material is optically active when $\tilde{n}$ is different depending on the different states of polarization that are measured. In an isotropic chiral medium the refractive index difference for the two circular polarization components is a signature of a chirality and can be written as $\delta\tilde{n} = \tilde{n}_L - \tilde{n}_R$. For example circular birefringence (CB) will be proportional to the real component ($CB \propto \Re[\delta\tilde{n}]$) and circular dichroism (CD) to the imaginary component ($CD \propto \Im[\delta\tilde{n}]$).

The question that rises naturally is: "How a certain material can be sensitive to the different states of polarization of light?". In case of molecular structures, this question can be addressed with a semiclassical description of the electromagnetic interactions in matter, where electromagnetic fields are modelled classically and the molecules can be described quantum mechanically; a detailed description of this theory can be found in the Chapter

2 of Ref. [7]. The theory permits one to calculate indices of refraction for molecular systems. The electric and magnetic multipolar moments determine the optical activity of a certain material. In most of the cases we are describing light-matter interactions where the interaction energy term is a perturbation with respect the whole energy of the system, therefore the three dimensional structure of molecules or of other scatterers such as nanostructures, determine the multipole moments that can be present.
The microscopic three dimensional shape of scatterers and their arrangement in space determines the difference in refractive indices for left and right circularly polarized light and therefore also the propagation of different circular polarization states. In addition, the size of the constituents of the material are important. Depending on the relative size of the constituents one either observes Rayleigh scattering or for larger structures Mie scattering [8]. We are interested in visible light of the order of $\lambda \simeq 5 \times 10^{-7}$ m, as this is the range of the wavelength of the electromagnetic waves that are visible to the human eye. In comparison, the physical dimensions of a molecule of water (H_2O) is of the order of 10^{-10} m. The optical activity for visible light that is found in molecular systems is usually very small. For example the circular dichroism, the difference of absorbed intensity of the two circular polarization states, is typically not more than of the order of 10^{-3} of the total absorbed intensity. This can be directly related to the difference of more than three orders of magnitude between the scale of the molecule and the wavelength of visible light. Molecules experience very small gradients of the electromagnetic field and therefore therefore the higher order multipolar response (magnetic-dipolar and sometimes also electric-quadupolar) which underlies optical activity phenomena is very small in molecules. It follows that larger structures experience stronger gradients of the fields and can thus show larger multipolar moments and thus optical activity phenomena. Larger structures will give rise to Mie scattering.

Chiral nanostructures for photonics

Most nanostructures are chemically synthesized, but they tend to be highly symmetrical and achiral. A recent advance in physical vapor deposition permits the growth of chiral thin films and chiral nanocolloids. The method is described in more detail in [9]. The method is better known as glancing angle deposition (GLAD) and the improvements that have been implemented in the new system have been published in Ref. [9]. This fabrication technique permits in particular to obtain nanohelices [10] with hybrid material composition and functionalities, deposited on arrays using large substrates (wafer scale) and that can be structured with good uniformity and with geometrical details on the order of ten nanometers.

There is a size difference between molecules and visible wavelengths. Nanofabrication techniques can be adopted to obtain designed meta-molecules [11] or meta-materials [12], with interesting optical properties. One focus of this thesis is the relation between shape of the nanostructured material and the polarization of light [13]. In particular in the case of metals, in the form of nanoparticles that can be shaped with sizes comparable to the mean free electronic collision length, the dynamics of the free electrons at optical frequencies is largely described by the boundaries of the particle itself. The collective motion of the free electron plasma, known as the plasmon resonance, can be excited by visible light [14, 15] and sustain a multipolar resonance. In this sense the nanoparticle can form a potential cavity for the effective electric field experienced by the free electrons. As the electric field is a vectorial field, transversal to the direction of propagation of the electromagnetic wave, the polarization of the field can drive the different resonant modes of the free electron plasma in the nanoparticle. When the symmetry in the shape of the metal nanoparticle is broken (i.e. not spherical), the modes of resonance can be strongly affected by the orientation of the particles with respect to the polarization of the electromagnetic wave [16].

Following these concepts, metal nanoparticles can then concentrate the light far below the diffraction limit [17] and the resonant modes can be tuned with the shape of the nanoparticles [18]. Unique applications have been envisioned for plasmonic devices, such as enhanced photovoltaic devices [19], in high sensitive biological sensors [20, 21]. Since the optical response of a medium depends on its shape, it is possible to design materials with optical properties that are not naturally found. Such metamaterials should also permit the construction of a material with negative index of refraction due to chirality [22]. This requires a very large optical activity in an artificial medium, which is discussed in Chapter 2. In order to characterize the medium a polarization interferometer is developed in Chapter 3, while in Chapter 4, the particular fabrication method and specific measurements are discussed for the first chiral metamaterial to show indications of the possibility to a obtain negative index of refraction.

Outline of the thesis and the results obtained

In this work arrays of metal nanohelices are fabricated with the GLAD technique to explore and optimize chiral metamaterials [10], with an optical activity that is tunable from the UV to the IR.

Chiral metamaterials deposited for example with copper, have been demonstrated to be able to give rise to large circular dichroism (CD) and these results have been reported in the Letter in Ref. [23]. The discrete dipole approximation (DDA) is used to simulate the optical response of these nanohelices.

In order to measure and determine the absolute value of the chiral index of refractions $\tilde{n}_L$ and $\tilde{n}_R$, a polarization interferometer was built, which uses a stabilized laser light at the specific wavelength of 633 nm. In order to test the setup a know optically active liquid crystal was characterized using the interferometer and the results were published in Ref. [24].

Under the assumption that the films are uniaxial (which is only partially

fulfilled), the films for the first time show that a negative refractive index due to chiralty is possible at visible wavelengths. A positive index of refraction for one circular polarization approaching the atmospheric air ($n'_L \simeq 1.1$) and the other polarization is possibly negative ($n'_R \simeq -0.2$).

Finally, using magnetic metals, a thin film with both large natural and magnetic optical activity is grown that permits the detection of magneto-chiral dichroism in absorption for visible light through arrays of ferromagnetic nanohelices. The results were published in Ref. [25]. Conclusions will be drawn in Chapter 6.

Chapter 1

Introduction

1.1 Theoretical background

1.1.1 Classic field theory of electromagnetism.

In vacuum.

Maxwell's equations were the first consistent field theory obtained from the classical laws of electricity and magnetism. In free space the differential Maxwell's equations read as [26]:

$$\nabla \cdot \vec{E} = 0, \tag{1.1}$$

$$\nabla \times \vec{E} = -\frac{\partial \vec{B}}{\partial t}, \tag{1.2}$$

$$\nabla \cdot \vec{B} = 0, \tag{1.3}$$

$$\nabla \times \vec{B} = \mu_0 \epsilon_0 \frac{\partial \vec{E}}{\partial t}. \tag{1.4}$$

where $\vec{E}$ and $\vec{B}$ are the electric and magnetic fields, t is time and $\epsilon_0 = 1/\mu_0 c^2 \simeq 8.854\cdots \times 10^{-12}\ F \cdot m^{-1}$ and $\mu_0 = 4\pi \times 10^{-7}\ H \cdot m^{-1}$ are in turn the vacuum permittivity and permeability, and c the speed of light in vacuum [27]:

$$c = \frac{1}{\sqrt{\epsilon_0 \mu_0}} \simeq\ 299792458\ m \cdot s^{-1}. \tag{1.5}$$

In the presence of matter

In presence of matter and therefore electrical charges ($\rho \equiv$ volume charge density) and currents ($\vec{J} \equiv$ current density), Maxwell's equations read as

$$\nabla \cdot \vec{D} = \rho, \tag{1.6}$$

$$\nabla \times \vec{E} = -\frac{\partial \vec{B}}{\partial t}, \tag{1.7}$$

$$\nabla \cdot \vec{B} = 0, \tag{1.8}$$

$$\nabla \times \vec{H} = \vec{J} + \frac{\partial \vec{D}}{\partial t}. \tag{1.9}$$

where the displacement field $\vec{D}$, the magnetizing field $\vec{H}$ and the current density $\vec{J}$ are additional auxiliary fields that describe the behaviour of particular substances under the influence of the electromagnetic field. These are called the constitutive relations and are determined often through a simple linear relation. In case of isotropic and uniform materials:

$$\vec{D} = \epsilon \vec{E} = \epsilon_0 \vec{E} + \vec{P}, \tag{1.10}$$

$$\vec{H} = \frac{1}{\mu}\vec{B} = \frac{1}{\mu_0}\vec{B} - \vec{M}. \tag{1.11}$$

with σ being the specific conductivity, $\vec{P}$ the polarization and $\vec{M}$ the magnetization. A particular material's response to the external fields is determined then by the dielectric permittivity and permeability associated with it as $\epsilon = \epsilon_0 \epsilon_r$ and $\mu = \mu_0 \mu_r$, where the subscript r respectively indicates the relative permittivity and the relative permeability. These determine the relative proportion to the vacuum constants (ϵ_0, μ_0) and quantify the secondary fields that are generated by the presence of the specific material in presence of the vacuum fields.

In the general case however, the constitutive relations are only approximatively simple and linear. The dispersive relations could still be written as before but with $\overleftrightarrow{\sigma}$, $\overleftrightarrow{\epsilon}$, $\overleftrightarrow{\mu}$ being now tensorial, dispersive and non-linear relations. Some materials can be bianisotropic materials [28] and the fields $\left(\vec{D}, \vec{H}\right)$ will be dependent both on $\left(\vec{E}, \vec{B}\right)$ through two more coupling

tensors $\overleftrightarrow{\xi}$ and $\overleftrightarrow{\zeta}$, as formulated in Ref. [29]:

$$\begin{pmatrix} \vec{D} \\ \vec{H} \end{pmatrix} = \begin{pmatrix} \overleftrightarrow{\epsilon} & \overleftrightarrow{\xi} \\ \overleftrightarrow{\zeta} & \overleftrightarrow{\mu}^{-1} \end{pmatrix} \begin{pmatrix} \vec{E} \\ \vec{B} \end{pmatrix} = \begin{pmatrix} \overleftrightarrow{\epsilon} \cdot \vec{E} + \overleftrightarrow{\xi} \cdot \vec{B} \\ \overleftrightarrow{\zeta} \cdot \vec{E} + \overleftrightarrow{\mu}^{-1} \cdot \vec{B} \end{pmatrix}. \tag{1.12}$$

As the constitutive relations should also satisfy Lorentz reciprocity the following symmetries will be present in the tensors [30]:

$$\overleftrightarrow{\epsilon} = \overleftrightarrow{\epsilon}^{T}, \quad \overleftrightarrow{\mu} = \overleftrightarrow{\mu}^{T}, \quad \overleftrightarrow{\xi} = -\overleftrightarrow{\zeta}^{T}, \tag{1.13}$$

where the superscript T represents the matrix transpose. The permittivity ($\overleftrightarrow{\epsilon}$) and permeability ($\overleftrightarrow{\mu}$) tensors describe in turn the dielectric and magnetic response of the material. Bianisotropic materials are described by the magnetoelectric tensors that relate the polarization to the magnetic field and the magnetization to the electric field [28]. In complex notation $\overleftrightarrow{\xi}$ and $\overleftrightarrow{\zeta}$ will be of the form

$$\overleftrightarrow{\xi} = \overleftrightarrow{\chi} - i\overleftrightarrow{\kappa}, \quad \overleftrightarrow{\zeta} = \overleftrightarrow{\chi} + i\overleftrightarrow{\kappa}, \tag{1.14}$$

In case of a reciprocal medium the real part $\overleftrightarrow{\chi} = 0$, and the constitutive equations will then read as

$$\begin{pmatrix} \vec{D} \\ \vec{H} \end{pmatrix} = \begin{pmatrix} \overleftrightarrow{\epsilon} & -i\overleftrightarrow{\kappa} \\ +i\overleftrightarrow{\kappa} & \overleftrightarrow{\mu}^{-1} \end{pmatrix} \begin{pmatrix} \vec{E} \\ \vec{B} \end{pmatrix}. \tag{1.15}$$

Here the $\overleftrightarrow{\kappa}$ is the chirality parameter and is non-zero if the material lacks mirror and inversion symmetry.

The constitutive equations can also be written in another form known as the Drude-Born-Fedorov (DBF) constitutive equations [31]:

$$\vec{D} = \overleftrightarrow{\epsilon}(\vec{E} + \overleftrightarrow{\beta}\nabla \times \vec{E}), \tag{1.16}$$

$$\vec{H} = \overleftrightarrow{\mu}^{-1}(\vec{B} + \overleftrightarrow{\beta}\nabla \times \vec{B}). \tag{1.17}$$

These are much commonly used in case of reciprocal chiral media and have a

different representation from the canonic constitutive relations in Eq. (1.12). Therefore the permittivity and permeabilities are defined differently, we refer here directly to the Appendix A of Ref. [31] for the relations between the two representations. What is interesting for the subsequent discussion is the explicit connection between the response fields to a perturbing harmonic field in chiral media. The presence of structural chirality in metals for instance is expected to show the full form of the constitutive relations of the Maxwell's equations (1.7) and (1.9).

Wave equations and index of refraction

Let's introduce now the wave equation of a propagating harmonic electromagnetic field, in the form of a d'Alambert equation of the electric and magnetic fields, through which is possible to define an index of refraction that characterizes the response of the medium. From Eq. 1.7 and 1.9 and the definition of the auxiliary fields in Eq. 1.10 and 1.11 the wave equations [26]:

$$\Box\vec{E} = \nabla^2\vec{E} - \epsilon\mu\frac{\partial^2}{\partial t^2}\vec{E} = \nabla^2\vec{E} - \frac{n^2}{c^2}\frac{\partial^2}{\partial t^2}\vec{E} = 0, \tag{1.18}$$

$$\Box\vec{B} = \nabla^2\vec{B} - \epsilon\mu\frac{\partial^2}{\partial t^2}\vec{B} = \nabla^2\vec{B} - \frac{n^2}{c^2}\frac{\partial^2}{\partial t^2}\vec{B} = 0, \tag{1.19}$$

can be obtained for homogeneous, isotropic, and linear media, where $n = \sqrt{\epsilon_r\mu_r}$ stands for the index of refraction of the material. The solutions of these differential equations are given in the general form with a planar wave, in case of the electric field

$$\vec{E}(\vec{r},t) = \vec{E}_0 e^{i(\vec{k}\cdot\vec{r}-\omega t)}, \tag{1.20}$$

where, given the spatial and the time coordinates as $(\vec{r},t)$, $\vec{k} = \frac{2\pi}{\lambda}\hat{k} = \frac{2\pi}{\lambda_x}\hat{x} + \frac{2\pi}{\lambda_y}\hat{y} + \frac{2\pi}{\lambda_z}\hat{z}$ is the wave-vector perpendicular to the plane of constant phase of the propagating field with wavelength $\lambda = \frac{\lambda_0}{n}$ and angular frequency $\omega = c/\lambda_0$. $\vec{E}_0$ is the space-time independent part, which determines the amplitude, the phase and the polarization of the wave. Maxwell's vector

Eq.s (1.7) and (1.9) can be written for harmonic fields, respectively as [32]

$$\begin{aligned} \vec{k} \times \vec{E} - \omega \vec{B} &= 0 && (1.21) \\ \vec{k} \times \vec{H} + \omega \epsilon \vec{E} &= -i\sigma \vec{E} \Leftrightarrow && (1.22) \\ &\Leftrightarrow \quad \vec{k} \times \vec{B} + \mu(\omega \epsilon_0 \epsilon_r + i\sigma)\vec{E} = 0 && (1.23) \end{aligned}$$

Redefining the relative permittivity (ϵ_r) in a new form, which explicitly includes the electric conductivity (σ) of a material where the wave with angular frequency ω is being propagated, with the substitution

$$\hat{\epsilon}_r \longrightarrow \epsilon_r + i\sigma/(\epsilon_0 \omega) \tag{1.24}$$

Eq. (1.23) can be rewritten as

$$\vec{k} \times \vec{B} + \omega \epsilon_0 \hat{\epsilon}_r \mu \vec{E} = 0 \tag{1.25}$$

This parametrization is particularly meaningful for conducting media, for instance metals. In the representation of the fields with complex numbers, the index of refraction is also complex ($\tilde{n}$), with a real component n' and an imaginary component n'':

$$\tilde{n} = n' + i\ n'' \tag{1.26}$$

To understand the effect of the complex index of refraction, let's consider a plane wave being propagated through a certain medium along the $\hat{z}$ direction. The electric field induced by the propagation of the wave will result in [33]:

$$\begin{aligned} \vec{E}(z,t) &= \Re[\vec{E}_0\ e^{i(\tilde{k}z - \omega t)}] = \\ &= \Re[\vec{E}_0 e^{i(2\pi(n' + in'')z/\lambda_0 - \omega t)}] = \\ &= e^{-2\pi n'' z/\lambda_0}\ \Re[\vec{E}_0 e^{i(2\pi n' z/\lambda_0 - \omega t)}] \end{aligned} \tag{1.27}$$

where λ_0 is the wavelength of the wave being propagated in vacuum. The effect of n' and n'' is now evident as the imaginary part will determine the exponential decay of the field's amplitude, where the real part is responsible for a phase change a wave experiences, when it propagates through the material. In general, the index of refraction will also be dispersive, so that $\tilde{n} = \tilde{n}(\omega)$ and so will be its wave-vector $\tilde{k}(\omega) = \frac{2\pi \tilde{n}(\omega)}{\lambda_0}$.

Group and phase velocity

The speed of propagation of the photons, the carriers of the electromagnetic field, is in vacuum equivalent to c in any frame of reference. A different situation is when we consider the propagation in media filled with matter. The electromagnetic charges and currents that are on the way of an incoming radiation, which is intended as a superposition of many photons, are driven by the interaction with the fields induced by the radiation and when accelerated, will generate secondary electromagnetic fields in response to the incoming radiation. The resultant field is then a superposition of both the primary and secondary fields. The secondary field will not only have a different amplitude but also a difference in phase depending on the electrodynamics of the different materials. The real part of the index of refraction, as defined in Eq.s (1.18) and (1.19), determines the speed of propagation of the electromagnetic wave in a certain material. Strictly speaking, in a dispersive medium this implies also that different frequencies will propagate at different velocities. For a wave-packet with a frequency distribution, the electric field for $\omega \in (-\infty, \infty)$ is

$$\vec{E}(\vec{r}, t) = \Re \left[\int_{-\infty}^{\infty} \vec{E}_0(\omega) e^{i(\vec{k}(\omega)\cdot\vec{r} - \omega t)} d\omega \right] \tag{1.28}$$

For electromagnetic waves, the vacuum wavelength λ_0 and the wavelength in a medium are related by:

$$n' = \frac{\lambda_0}{\lambda} = \frac{c}{v_p} \tag{1.29}$$

where $\Re[\tilde{n}] = n'$ and where v_p is the phase velocity of the wave:

$$v_p = \frac{\lambda}{T} = \frac{\omega}{k} = \frac{c}{n'}, \tag{1.30}$$

with the period $T = \frac{2\pi}{\omega}$, the time taken for a complete oscillation of the field at the angular frequency ω. The group velocity (v_g) as discussed for example in Ref. [34] or [32], can be computed as:

$$v_g = \frac{d\omega}{dk} = \frac{c}{n' + \omega \frac{\partial n'}{\partial \omega}}. \tag{1.31}$$

This corresponds to the velocity of propagation of the maximum of the wave-packet.

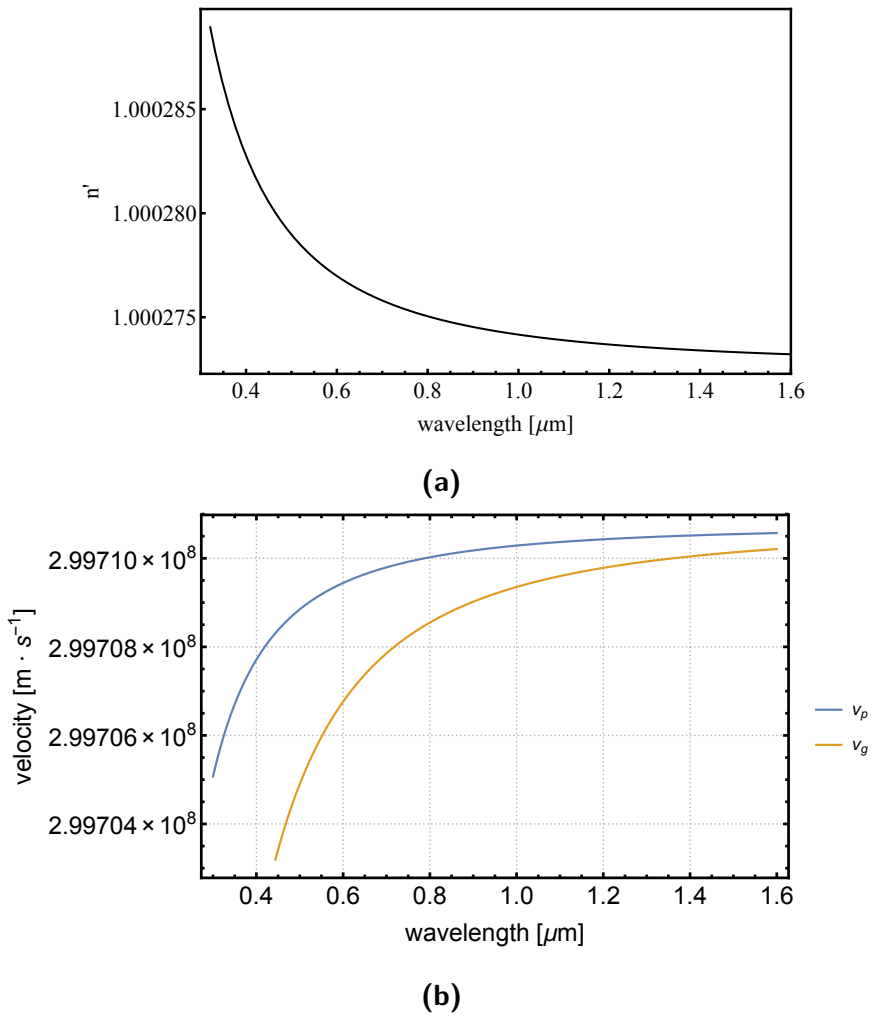

Figure 1.1: (a) Real part of the index of refraction (n') of air at 15 °C, 101325 Pa and with 450 ppm CO_2 content [35]. (b) Phase (v_p) and group (v_g) velocities as calculated from the values shown in (a).

After recalling some notion of electrodynamics, is clear that the electromagnetic response of matter is depending on the materials and the geometry of how it is structured. For example, bulk gold is not considered a magnetic material but when wound in a solenoidal shape it will have a magnetic inductance! The field response of a certain body is described by ϵ_r and μ_r while the response to electromagnetic waves, is described with the index of refraction. As electromagnetic waves are coupled harmonic electric and

magnetic fields, it is clear how these quantities are connected as explicitly stated from Eq.s (1.18) and (1.19).

Let's for example consider atmospheric air, the index of refraction of air has been precisely measured and fitted with an empirical dispersion function. Accurate studies on atmospheric air's dispersive properties are found in Ref.s [35–37] and imported here from the publicly available database, accessible from this webpage [38]. Throughout this thesis all frequency-dependent permittivities and refractive index data are taken from Ref. [38]. A Sellmeier equation for the dispersion of the index of refraction for dry air at 15 °C, 101325 Pa and with 450 ppm CO_2 content, is given by the relation [38]:

$$n'(\lambda_0) = 1 + \frac{0.05792105}{238.0185 - \lambda_0^{-2}} + \frac{0.00167917}{57.362 - \lambda_0^{-2}} \tag{1.32}$$

where $\lambda_0 = \frac{2\pi c}{\omega}$ is the wavelength in vacuum. These values are plotted in Figure 1.1a Despite the small dispersion v_p^{air} and v_g^{air} depend on the frequency (ω), as is shown in Fig. 1.1b.

As is discussed in the next section, there are some materials where the physics of the interaction between light and matter becomes more complicated and n' can even have values very close to zero.

1.1.2 Optics of metals

As it is evident from the substitution that was introduced in (1.24), ϵ_r depends on the electric conductivity of the material so that $\epsilon_r = \epsilon_r(\omega, \sigma)$. Rakić et al. [39] compared various measurements of the complex dielectric constants for 11 different metals of interest for optoelectronic applications; they fit two different mathematical models to the experimental data for the electromagnetic spectrum from the UV to the mid-IR. The theoretical models used are the Lorentz-Drude (LD) and the Brendell-Bormann [40] (BB) models. In both $\epsilon_r(\omega) = \epsilon_r^f(\omega) + \epsilon_r^b(\omega)$ is written as combined

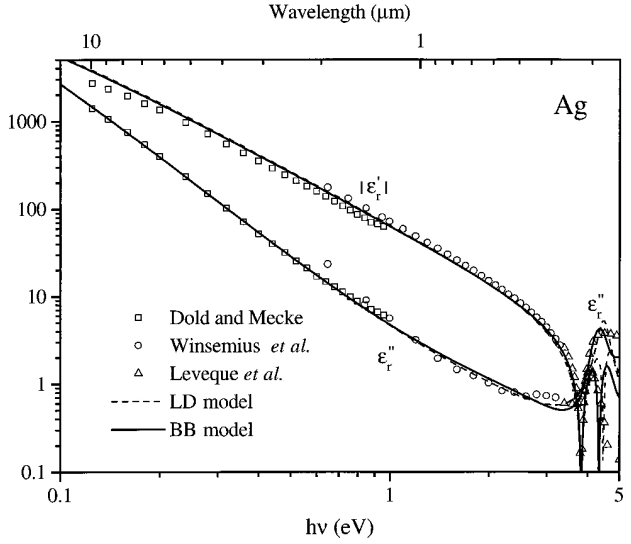

Figure 1.2: Dielectric function (real and imaginary components) of silver (Ag). Adapted and reprinted from Ref. [39].

contribution from free (f) and bound (b) electrons. In case of the LD theory this is modelled with a discrete set of semi-quantum damped oscillators accounting for the intraband transitions based on the Lorentz model for insulators. In contrast, ϵ_r^b in the BB theory it is modelled by a Gaussian distribution of a superposition of an infinite number of harmonic oscillators. In Figure 1.2 the results from both models are plotted together with the measurements published in Ref.s [41–43].

Using a MATLAB code implemented from Meierbachtol [44] it is possible to plot the model. Figure 1.3 shows a comparison between the real part of the index of refraction (n'), obtained from the BB model's fit as optimized in Ref. [39], with other two datasets from measurements published in Ref. [45] and [46]. It is evident that the BB model fails as soon as UV wavelengths are considered.

After these considerations about silver it should be clear that the electrodynamics inside metals can have some interesting properties. The first problem that we should address now is how some metals have low values of n' and a high absorption and therefore also high values of n''. In response to a time-dependent field [14] like

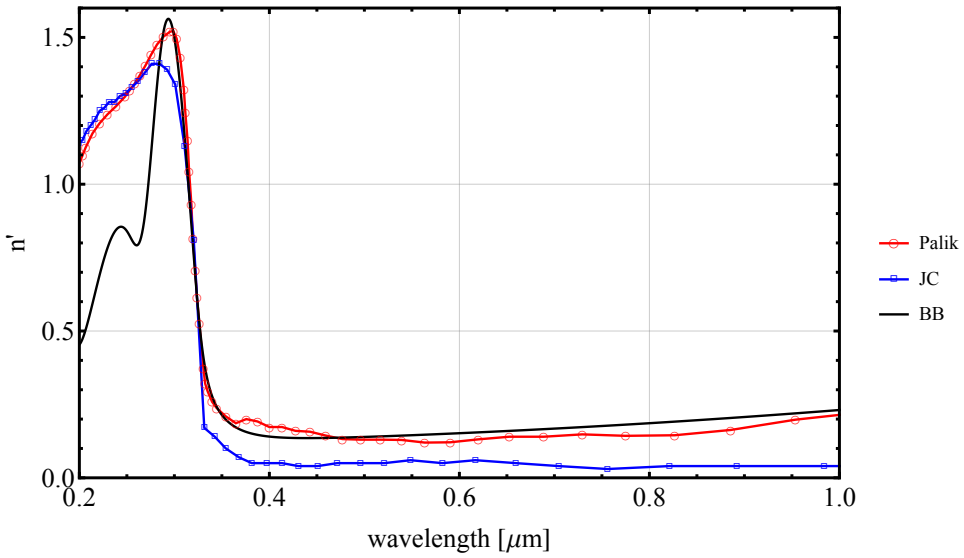

Figure 1.3: Real component of the index of refraction (n') in the visible spectrum. The fit of BB model [39, 44] for Ag compared with two independent measurements from Palik, E.D.[45] and Johnson, P.B. and Christy, R.W.[46].

.

$$\vec{E}(t) = \Re[\vec{E}(\omega)e^{-i\omega t}] \tag{1.33}$$

referring to the Drude model of free electrons, the equation of motion of the electrons results in

$$\frac{d\vec{p}}{dt} = -\frac{\vec{p}}{\tau} - e\vec{E}(t) \tag{1.34}$$

where, τ is the relaxation time and it describes the mean time of free motion between two consequent collisions, that each free electron will experience. Looking for steady-state solutions of the form

$$\vec{p}(t) = \Re[\vec{p}(\omega)e^{-i\omega t}] \tag{1.35}$$

the electric conductivity takes the form [14]

$$\sigma(\omega) = \frac{\sigma_0}{1 - i\omega\tau}, \qquad \sigma_0 = \frac{ne^2\tau}{m}. \tag{1.36}$$

As discussed in Ref. [14] within the model of a free gas of electrons (electric charge e and mass m) with volume charge density n, assuming only electron-electron collisions without long range interactions.

The effect of the magnetic field $\vec{H}$ is ignored because typically the term in $\vec{H}$ in the equation of motion for the electrons [14]

$$\frac{d\vec{p}}{dt} = -\frac{\vec{p}}{\tau} - e\vec{E} - \frac{e\vec{p}}{m} \times \vec{H} \tag{1.37}$$

is a ratio of v/c of the effect of the term in $\vec{E}$, where here v is referred to velocities associated with collective motions of all the electrons, which also for large current densities, are not larger than $\sim 10^{-3}\ m/s$.
If one writes the motion of the electrons that follow the field induced by the electromagnetic wave, i.e. for solutions of the form $e^{-i\omega t}$, the complex dielectric function is given by [14]

$$\epsilon(\omega) = 1 + i\frac{\sigma}{\epsilon_0\omega}. \tag{1.38}$$

Substituting (1.36), it is possible to recognize the bulk plasma frequency of the metal [14]:

$$\omega_p^2 = \frac{ne^2}{m\epsilon_0}, \tag{1.39}$$

which corresponds to the zero crossing of $\epsilon(\omega)$.

As it is possible to recognize, comparing these results to the measured values in the just discussed case of silver (Figure 1.2), the free electron model is an idealized model and the case of real metals can easily vary, where electronic interactions or lattice interactions, as well as many other effects can

soon change the properties of the electric conductivity spectrum. The real case is much more complicated than the ideal one and at the present day, first principle models are limited. The same distinction already noted between the dynamics of the free electrons and bounded electrons present in a metallic phase can bring a difference in the electrodynamics. In particular, for a fortuitous convergence, the free electron model works surprisingly well in the case of most alkali metals, while it is mostly insufficient for describing the electrodynamics of other materials [14]. The comparison between the frequency of oscillation of the fields induced by the propagation of light, must compare with the typical relaxation time of the electrons. In fact, in connection with the free electron model, it is possible to visualize that between two successive collisions, the electrons are, in a first approximation, in free motion under an oscillating field. Qualitatively, if then the product $\omega\tau >> 1$, we are surely in this case and the free electrons are also then behaving as they were bounded electrons. They are oscillating around a steady position, driven by the field induced by the propagation of light; ω_p is formally the frequency at which the whole electron plasma follows with a phase the oscillation of the field. This phenomenon of wave-induced collective oscillation mode of the free electron plasma, is therefore the definition of a quasi particle, called a plasmon.

The empirical BB model used previously to fit the measured values of the dielectric function in the case of silver, models in fact the optical response as from a series of oscillators that reproduce well the electrodynamic properties of the metal for frequencies below the plasmonic resonance.

If we should consider a smaller piece of a metal comparable or even smaller with respect to the wavelength of visible light, i.e. a nanoparticle (NP), the electromagnetic fields have to be treated as non-local. The displacement of the free electrons against the ionic crystal structure, can create in the proximity of the NP's physical boundaries, fields that are up to $\sim 10^2$ times stronger than the incoming fields, which are then confined according to the shape of the metallic NP. In this case we can think the

domain of motion of the free electrons plasma is imposed by the physical boundaries of the NP, which can work in fact as a potential cavity for the free electrons respect to a dielectric background medium. In this way one can then also think to squeeze or release an overall effective potential, that is then imposed by the same physical structure of the NP.

The properties of the electrodynamics in metal NPs have been the subject of study and a very active field of research as it envisions possibilities for applications in many fields. By itself is a subject of research, both as broad source of information about the electrodynamics and in connection to the technical applications offered, the properties of scattering of light from nanoparticles is nowadays an established field of research that spans from physics, to chemistry, medicine and materials engineering. Unfortunately, the physics of the electromagnetic scattering of light from sub-wavelength objects is complicated and in general, it is impossible to obtain analytical solutions of the set of Maxwell's equations except than for highly symmetric scatterers. In fact, analytical solutions have been found only for spherical nano-particles, ellipsoidal or infinite rods, all based on the formal solutions of the Maxwell's Equations for spherical objects, best known as Mie's scattering [8, 15, 47].

1.1.3 Light scattering from a metal nanoparticle

The solutions of the Maxwell's equations formally calculated by Mie [47] well describe the physics of the scattering of electromagnetic waves from a sphere of arbitrary size. The theory of Mie scattering is presented in numerous books [8] and is applied to a broad range of experiments, for example to interpolate a distribution for the size of water drops in the atmosphere, useful for describing the phenomenon of rainbow formation [48] or more technical problems related the size distribution of raindrops encountered during the modelling of radar echoes [49]. Another example closer to our interests is the application of Mie's theory for the description of the light scattering through stained glass; in fact, the antique methods

of preparation of these glasses, employ fine powders of plasmonic metals such as copper, gold or silver mixed in the furnace which together with the silica, result in a suspension of metal nanospheres in the glasses that scatter the light transmitted through it. This was the first application Mie himself found for his theoretical results [47] and permitted him to determine the mean size of the metal NPs corresponding plasmonic peak of absorption of light.

The results of Mie scattering can be used to calculate the cross sections of the scattering (σ_{sca}) and absorption (σ_{abs}) of light, as a function of the radius of the sphere and the relative index of refraction. Most commonly the important quantity is an extinction efficiency which is defined as

$$Q_{ext} = Q_{sca} + Q_{abs} = \frac{\sigma_{sca}}{\pi r^2} + \frac{\sigma_{abs}}{\pi r^2}, \tag{1.40}$$

where r is the radius of the sphere.
The intensity of the transmitted light, with incoming intensity I_0 can then be calculated as

$$I = I_0 \, Q_{ext}. \tag{1.41}$$

In a suspension with volume density η, then the Q_{ext} will be proportional to η and the intensity will drop inversely to the thickness of material l

$$I = I_0 \cdot e^{-\eta \, l \, S \, Q_{ext}}, \tag{1.42}$$

with S representing the probed surface area of the material. Here the efficiency factors can be written with respect to $x = \frac{2\pi r}{\lambda}$, and are equivalent to

$$Q_{ext} = \frac{2}{x^2} \sum_{n=1}^{\infty} (2n+1) \Re(a_n + b_n), \tag{1.43}$$

a_n and b_n are written in terms of the Riccati-Bessel functions [8] for the

fields in function of the angular polar coordinates. As usual in a medium (with index of refraction n) different from vacuum, the wavelength of light will be equivalent to $\lambda = \frac{\lambda_0}{n}$, with λ_0 the equivalent wavelength in vacuum.

Unfortunately, if the scattering on NPs with arbitrary shapes is considered (for example helical shapes), there exists no formal analytical solution to Maxwell's equations. The only way to make calculations, is then by numerical optimization methods. Different numerical methods are available. In this thesis the dipole-dipole approximation (DDA) method is considered.

1.2 Numerical method

The numerical method adopted here is based on the DDA. In particular DDSCAT 7.2.2 has been used, which is a freely available open-source Fortran-90 software package. DDSCAT can calculate the absorption and scattering of electromagnetic waves by targets with arbitrary shape and complex index of refraction. The shape of a specific object can be reconstructed as an evenly spaced lattice of polarizable points and the theory and its implementation of DDSCAT are available in the Ref.s [50–52].

The DDA provides a method to obtain approximate solutions to the Maxwell's equations. As the same authors motivate in Ref. [51]: "Nature provides the physical inspiration for the DDA: in 1909 Lorentz showed that the dielectric properties of a substance could be directly related to the polarizabilities of the individual atoms of which it was composed, with a particularly simple and exact relationship, the Clausius-Mossotti (or Lorentz-Lorenz) relation, when the atoms are located on a cubic lattice. We may expect that, just as a continuum representation of a solid is appropriate on length scales that are large compared with the interatomic spacing, an array of polarizable points can accurately approximate the response of a continuum target on length scales that are large compared with the interdipole separation".

A target with arbitrary shape can be reconstructed by N polarizable points,

with definite position $\vec{r}_j$, $j \in \{1 \dots N\}$. In DDSCAT the $\vec{r}_j$ are on a cubic lattice with spacing d. The electromagnetic scattering problem can be solved for an incident planar wave as in (1.20), with $\vec{E}_j^{inc} = \vec{E}(\vec{r}_j, t)$ at each polarizable point of the target. If each point of the target's array has a defined dipole electric polarizability, α_j, such that its polarization results [51]:

$$\vec{P}_j = \alpha_j \vec{E}_j \ , \tag{1.44}$$

then the total electric field, including the contributions from all the other $N-1$ polarizable dipoles at the point $\vec{r}_j$ is

$$\vec{E}_j = \vec{E}_j^{inc} - \sum_{k \neq j} \overleftrightarrow{A}_{jk} \vec{P}_k \ , \tag{1.45}$$

with each of the $\overleftrightarrow{A}_{jk}$ being represented by a 3×3 matrix:

$$\overleftrightarrow{A}_{jk} = \frac{e^{i\vec{k}\cdot\vec{r}_{jk}}}{\vec{r}_{jk}} \left[k^2(\hat{r}_{jk}\hat{r}_{jk} - I_3) + \frac{ikr_{jk} - 1}{r_{jk}^2}(3\hat{r}_{jk}\hat{r}_{jk} - I_3) \right], \tag{1.46}$$

where $r_{jk} = |\vec{r}_j - \vec{r}_k|$ and $\hat{r}_{jk} = (\vec{r}_j - \vec{r}_k)/r_{jk}$. If one defines the $\overleftrightarrow{A}_{jj} \equiv \alpha_j^{-1}$, the problem is solved by finding the polarizations P_j that satisfy the $3N$ linear equations:

$$\sum_{k \neq j} \overleftrightarrow{A}_{jk} \vec{P}_k = \vec{E}_j^{inc}. \tag{1.47}$$

These P_j polarizations can then be used to calculate the σ_{ext}, σ_{sca}, σ_{abs} [51].

Initially, the polarizability of the points representing the target object were initially described with the Clausius-Mossotti polarizability, as is discussed in section 3.B in Ref. [51]. In DDSCAT, instead, a modified polarizability, with the lattice dispersion relation (LDR) [53], is used instead, which corrects for radiative reaction and is optimal for wave propagation on an array of dipoles to reproduce the corresponding dispersion relation,

assuming to be interested in a continuous medium instead of the point array representation of the target in the simulator software.

The equation (1.47) can be solved with a number of complex-conjugate gradient (CCG) methods [50]. Further, as the targets are represented from cubic arrays of polarizable points, the fast Fourier transforms (FFT) turn out to be ideal transformations that can effectively reduce the number of iterations required for the CCG method to optimize the solutions of the equations, as discussed in detail in Ref. [54].

Apart from the correct physical geometry of the target object, the two most important parameters to be carefully chosen are the data for the index of refraction and the number of dipoles N used to create the target, or more explicitly, is the cubic lattice spacing d that has to be provided to the software. DDSCAT [52] suggests to use at least $N \gtrsim 10^4$ points for the target's model. As this is the most sensitive parameter in terms of the computational time needed, a series of tests were carried out.

To test the reliability of this order of magnitude, DDSCAT simulations for scattering and absorption of visible light on a spherical NP with variable size, where compared to the Mie's theory. In Figure 1.4 are shown some representative results of the DDSCAT simulations compared to Mie theory (as from 1.1.3: Q_{ext} is plotted with a straight red line and Q_{sca} with a broken green line). The material of the NP was chosen to be gold and the frequency dependent complex index of refraction is imported for DDSCAT from the dataset from Ref. [46]. The medium's index of refraction was assumed to be $\tilde{n} = 1.33$ (water). The number of dipoles used to construct the sphere's 3D model was kept constant with $N = 41851$. For the radius (r) spanning from $r = 5\ nm$ to $r = 500\ nm$, the failure of the results of DDSCAT was demonstrated qualitatively for $r \gtrsim 80\ nm$. The results of DDSCAT show in fact that above $\sim 50\ nm$ the effect of absorption ($Q_{abs} = Q_{ext} - Q_{sca}$) is larger than the scattering.

Further, another series of calculations had ran also for gold nano-spheres with different sizes, this time also varying the number of polarizable points

from 10^0 to $\lesssim 10^6$. These revealed again that for $N \gtrsim 10^4$, the mean variance between the values obtained from DDSCAT and the Mie's theory, tend to a minimum. Further in terms of performance of the computer clusters that were used for the calculations, was observed that for larger target models, obtained with $N \sim 10^6$, would require computation times of the order of different weeks, to be completed for each single wavelength and each single orientation.

Let's point out again that the magnetic interactions are completely ignored in DDSCAT, however this reveals to be particularly useful to prove the presence of optical activity, due to structural chirality imposed by nanohelix particles. The connection with the magneto-electric coupling in the DBF constitutive equation (1.16), which is described by the factor proportional to $rot\left(\vec{E}(\vec{r},t)\right)$ is in this regards immediate. In Chapter 2 are shown comparisons between CD spectra calculated with DDSCAT and measurements carried on real samples, fabricated with GLAD. It is proven that is in fact the structural chirality of the nanohelices to induce the strong optical activity that is observed. In case of calculations performed on a finite nano-helical object, no theoretical model exists to compare to. Therefore the possibility to estimate the goodness of the simulations can be proven only in comparison to direct experimental measurements.

1.3 Fabrication method

To be able to obtain thin films with precise nanostructures using a wide range of materials, a glancing angle deposition (GLAD) method was adopted for the scope of this thesis. A good review of this method was published from Taschuk et al. in Ref. [55]. First scientific publications using the idea of oblique angle deposition are recorded since the ending period of the 19th century [56, 57], while glancing angle deposition uses a similar idea but adds the control on the substrate's orientation. This permits control over the columnar deposition and in the modern GLAD systems, real time

sensor feedback and computer controlled motorized positioning stages for the substrate, have improved the shape control of the deposited structures and their quality.

A newly improved GLAD system which is in function at the MPI-IS [9], provides an elegant method to fabricate arrays of nanostructures with programmable geometrical structures using a physical vapour deposition process. This GLAD system in particular, uses liquid nitrogen cooling of the samples holder, to control the temperature of the sample during the deposition process. This is particularly helpful to achieve a control regarding the condensation of the evaporated materials that are to be used during the deposition [58].

One key feature that is very relevant for this improved GLAD system, is the adoption of substrates which have been precedently patterned on the deposition surface with ordered arrays of monodispersed spherical nanoparticles. The patterned surfaces are obtained in most of the cases with gold nanospheres, which are deposited using a technique known as block copolymer micellar nanolithography (BCML) [59]. C. Miksch helped with the preparation of all the GLAD substrates which were used in this work. The use of these patterned substrates permits a seeding of the condensing materials on the surface, to start the directional shadowed growth at grazing angles of incidence of the physical vapour with respect to the sample's surface.

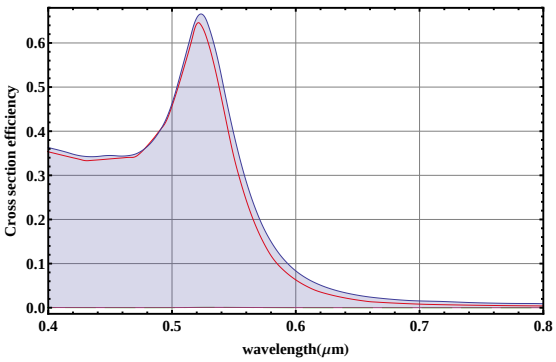

(a) r=5 nm.

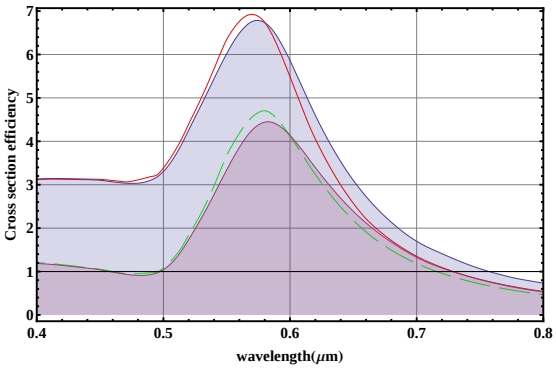

(b) r=50 nm.

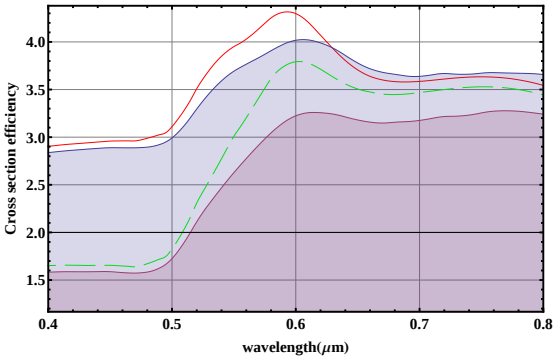

(c) r=180 nm.

Figure 1.4: Some of the spectra for Q_{ext} (blue) and Q_{abs} (purple) selected for a comparison between the results of numerical simulations obtained with DDSCAT 7.2.2 and Mie's theory Q_{ext} (red straight line) and Q_{abs} (green broken line). The calculations consider the physics of scattering on a gold spherical nanoparticle with different radius (r) in water ($\tilde{n} = 1.33$). The total number of polarizable points is set to N=41851.

Chapter 2

Chiral plasmonic metamaterials

Parts of this chapter have appeared in the publication
Appl. Phys. Lett. 103, 213101 (2013). [23]

Of a number of potential chiral shapes, the helix has been identified to be the ideal shape for far-field chiroptic response [60]. A few examples with different geometries for chiral plasmonics have been previously studied: stereo metamaterials [61], the effective helical ordering of multi-layer twisted metamaterials [62], plasmonic oligomers [63], and solid Au helices fabricated by 2-photon lithography [64]. E-beam lithographic methods allow high-resolution complex patterns and shapes to be defined, but they generally only permit 2D structures and require long processing times, yielding only small sample areas. Direct laser two-photon lithography permits true 3D shapes to be realized, but the method provides relatively low resolution (pixel resolution $\sim 100\,\mathrm{nm}$) and gives similarly low yields. Also the polymer has to be replaced by a plasmonic metal in an additional process. Due to the long processing times and low yields of these techniques, systematic studies of the geometric effects on chiroptical response have been lacking.

In 2013 the findings of this chapter were reported in the letter in Ref. [23]. The GLAD fabrication technique [9] allows for the reproducible growth of aligned and well separated sub-wavelength chiral plasmonic nanohelix

arrays when combined with substrate patterning and temperature control. The flexibility of the dynamic physical deposition growth process allows the tuning of the chiroptical response of helical chiral metamaterials in the visible and the systematic exploration of the effect of helix morphology and spacing.

2.1 Circular Dichroism

Circular dichroism (CD) is a measurement of the difference in the absorption of the two orthogonal circular polarization (CP) states of light. CD spectroscopy is a very important analytical tool that can be used to determine the handedness of chiral molecules in solution. Similarly it can also be used to determine the chirality of uniaxial films. If the intensity of incoming light is $I_0 = (I_L + I_R)/2$ and the transmitted intensity of left handed (LCP) and right handed (RCP) circular polarizations are respectively I_L and I_R then CD is given by the following relation:

$$\mathrm{CD} = \frac{\Delta I}{I_0} = 2\frac{I_L - I_R}{I_L + I_R}. \tag{2.1}$$

For an isotropic or uniaxial optically active material the complex index of refraction $\tilde{n} = n' + in''$ is different for LCP and RCP and is given by $\tilde{n}_{L,R} = \tilde{n}_0 \pm \delta\tilde{n}/2 = (n'_0 \pm \delta n'/2) + i(n''_0 \pm \delta n''/2)$, with $\delta\tilde{n} = \tilde{n}_L - \tilde{n}_R$. The extinction of light is related to the imaginary component of the index of refraction n'', thus CD will be proportional to $\delta n''$.

We now explore the factors that affect the strength of the optical activity in thin film metamaterials that exhibit a plasmonic resonance, first considering the CD for transmission of light along the axial direction of the helical structures. Numerical simulations were used to model the interaction of CP light with the nanohelix structures and were compared to measurements in samples that can be fabricated using GLAD. The arrays of plasmonic nanohelix samples were grown on glass substrates to allow for the transmission of light.

2.2 Numerical simulations

It is known that the shape of plasmonic nanoparticles directly affects the scattering of electromagnetic waves. DDSCAT 7.2 is a publicly available Fortran-90 code for the calculation of the scattering and absorption of arbitrarily shaped objects with complex indices of refraction. The software constructs the volume of an object as an array of equally spaced polarizable point dipoles and calculates the interaction with a monochromatic plane wave and includes the mutual interaction between each point dipole.

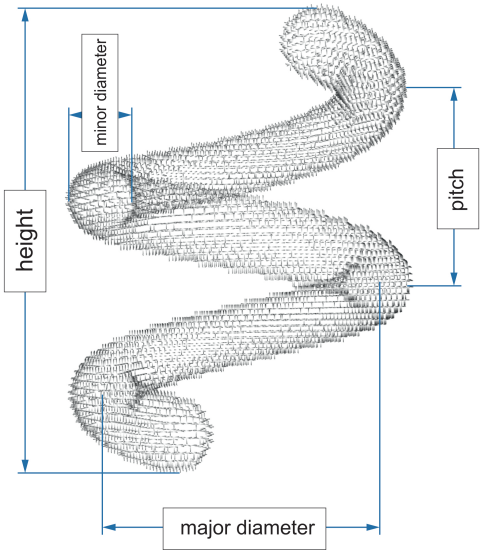

Figure 2.1: A schematic of the point array model of a helix used for numerical simulations. The four shape parameters of the helix are indicated. The minor diameter is the transverse diameter of the wire, the major diameter is the diameter of an imaginary cylinder about which the helix is coiled, the pitch is the length of one single full turn and the height is the distance from the top to the bottom.

An array of point dipoles of a helix is shown in Figure 2.1 which also shows the geometrical parameters defining the helix's morphology: the minor diameter ($2r$) is the transverse diameter of the wire that ideally forms the solid body of the structure, the major diameter ($2a$) is the diameter

of the imaginary cylinder which is coaxial with the helix and extends to the center of the wire. The pitch (P) is the length of one single full turn of the helix and finally the height (h) is the distance from the top to the bottom. Previous numerical analysis of plasmonic nanohelices, predicted a CD spectral dependence upon P; namely, as P increases, the differential absorption maximum is expected to red-shift [65], although the helix major radius a has been shown to give a larger effect than the pitch [66].

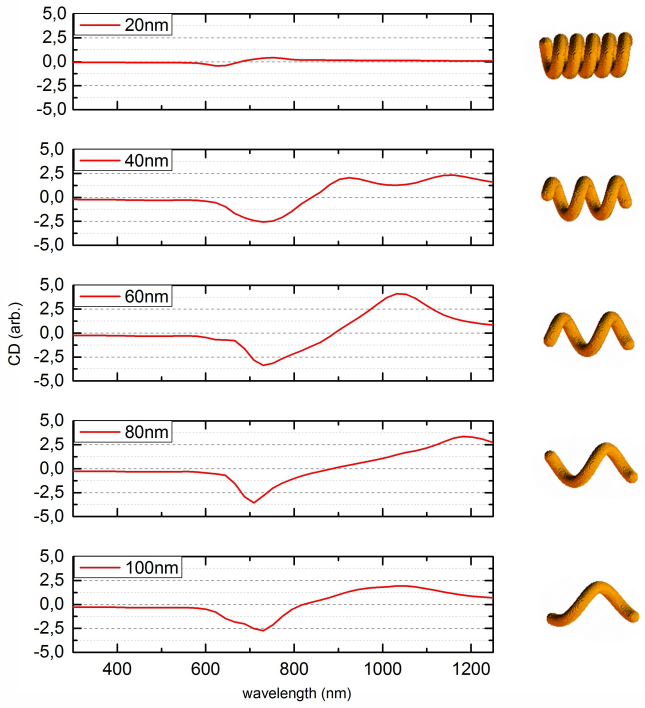

Figure 2.2: Calculated CD spectra for a left handed Cu helix for light propagation along the axis of the helix. The spectra from top to bottom are obtained by altering the pitch $P = 20, 40, 60, 80, 100$ nm. The height $h = 116$ nm, the major radius $a = 20$ nm, and the minor radius $r = 8$ nm are kept constant.

The shape of a plasmonic nanoparticle influences its optical properties. Therefore, one expects also that the CD spectrum is influenced by the shape of the helix. To explore these effects systematically, series of simulations

were conducted, in which each of the helix's shape parameters was varied while the others were held constant. The CD spectra have been calculated for visible light incident along the axis of a single left handed copper helix. The material properties are introduced from measurements of the complex index of refraction of copper [46].

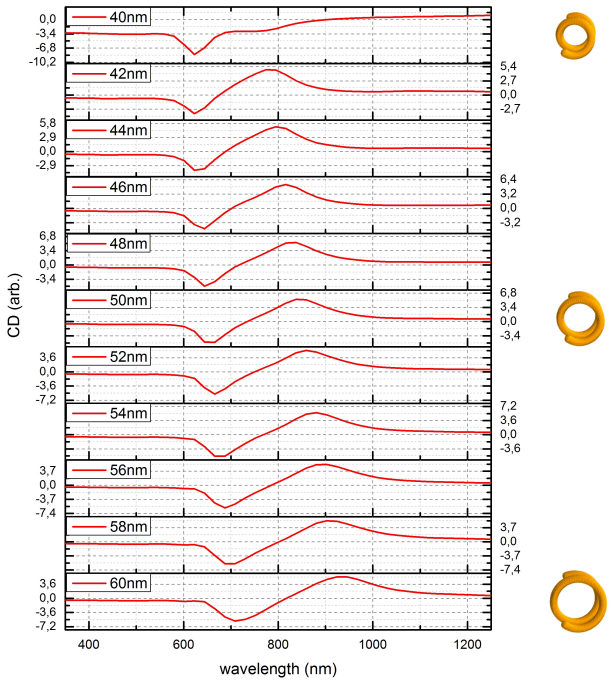

Figure 2.3: Calculated CD spectra for a left handed Cu helix for light propagating along the axis of the helix. From top to bottom, the major radius is varied ranging from $a = 18$ nm to $a = 38$ nm at steps of 2 nm. The other dimensions are held constant: $h = 116$ nm, $P = 40$ nm and $r = 8$ nm.

In Figure 2.2 the computed CD spectra for a left handed helix with $h = 116$ nm, $a = 20$ nm, $r = 8$ nm for five different pitch lengths $P = 20, 40, 60, 80, 100$ nm are shown. The positive peak of the CD corresponding to a dominant absorption of LCP seems to be much more sensitive to the variation of P in terms of the expected red-shift and the broadening of the

peak. In particular it is interesting to note the appearance of different peaks. For example for the spectrum calculated for the helix with $P = 40$ nm there are two peaks at $\lambda = 924\ nm$ and $\lambda = 1161\ nm$, which correspond to higher modes of the plasmonic resonance that can be sustained on the helical structure. The helix with $P = 60\ nm$ exhibits the largest magnitude of the CD response. As shown in the next section, this result is also seen in the experimental data.

The pitch of the helix seems not to affect the position of the absorption peaks in a simple way but instead has the role of tuning the coupling of different resonance modes. The effect of the shift in wavelength can more clearly be seen if one observes the series of calculations shown in Figure 2.3, in which the major radius (a) was varied while holding all other parameters constant. With increasing a, the CD spectrum red-shifts and the CD signal increases in magnitude. In order to facilitate the comparison, the incremental ratio $\zeta = \frac{\Delta\lambda[nm]}{\Delta a[nm]}$ was calculated for the two peaks of the CD, which result in $\zeta_{LCP} \sim 11$ and $\zeta_{RCP} \sim 5$; the $\Delta\lambda$ is the shift in wavelength of the peak for the complete $\Delta a = 20$ nm variation of the major radius.

The opposite trend is instead observed when considering an increase of r, the effect of which is shown in Figure 2.4. The increase of r causes the CD to blue-shift. In this case the sensitivity to the minor radius results in $\zeta_{LCP} \sim -46$ and $\zeta_{RCP} \sim -36$, where ζ is this then calculated from the two peaks of CD with respect to the variation of r as $\zeta = \frac{\Delta\lambda[nm]}{\Delta r[nm]}$.

Finally, altering the height (h) of the helices does not influence the spectral response but only causes an increase of the magnitude as is qualitatively shown in Figure 2.5.

The calculations presented so far have been for a single helix and have not considered the optical responses of nanohelix arrays, where, for example, the mutual coupling of adjacent helices and thus the surface density are expected also to influence the optical activity. There have been already pre-

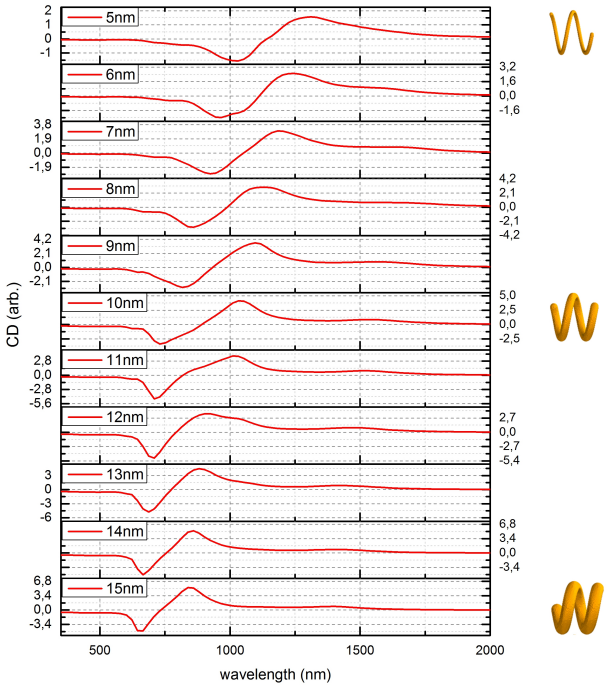

Figure 2.4: Calculated CD spectra for a Cu helix for light propagating along the axis of the helix. From top to bottom, the minor radius is varied ranging from $r = 5$ nm to $r = 15$ nm at steps of 2 nm. The other dimensions are held constant: $h = 116$ nm, $P = 40$ nm and $a = 28$ nm.

vious studies that have considered the effect of the spacing of the array [67]; their conclusion is that a more packed array of helices is expected to augment the magnitude of the CD. However there could be a limit to this trend given the mutual interaction between adjacent plasmonic structures. This aspect will be discussed in more detail, after considering the experimental data recorded from GLAD samples fabricated on substrates patterned so to obtain a set of different spacing between the nanohelices.

2.3 Sample fabrication and characterization

The samples for chiroptical measurements are fabricated on glass slides with a thickness of ~ 200 μm. A nanolithography process, block copolymer

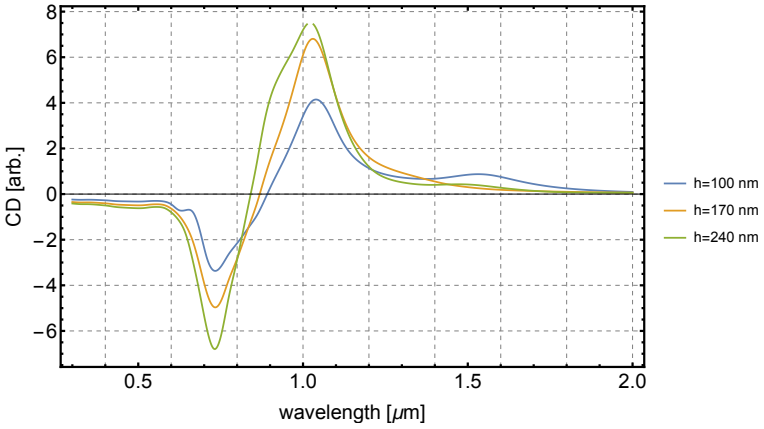

Figure 2.5: Calculated CD spectra for a left handed Cu helix for light propagating along the axis of the helix. The height is varied ranging from $h = 100$ nm to $h = 250$ nm. Here are shown selected lengths with $h = 100$ nm, 170 nm, 250 nm) The other dimensions are constant: $P = 40$ nm, $a = 28$ nm and $r = 8$ nm.

micellar lithography (BCML), allows an entire glass slide to be patterned with Au nanodots in a relatively rapid manner [59]. This results in equally spaced nanoseed arrays, which are arranged on a hexagonal geometry. The BCML-patterned substrates have been prepared by C. Miksch. The GLAD depositions were carried out by the author together with J.G. Gibbs who also analysed the helix morphologies and critical dimensions with scanning electron microscopy (SEM). Figure 2.6 shows a schematic that defines the dimensions for individual nanohelices (a). An inset with the structural details for a co-deposited metal alloy of Cu/Ag is shown in (b), where each image on the raster was chosen at a different orientation to reveal clearly the three-dimensional helix morphology. For this particular sample $P = 54$ nm, $a = 16$ nm, and $r = 14$ nm for a 2-turn helix. The tunable hexagonal lattice spacings of average separation, φ, defines the separation between individual helices, as shown in Figure 2.6(c). The seed size affects the final helix minor radius.

In order to measure the chiroptical tunability of these helical metama-

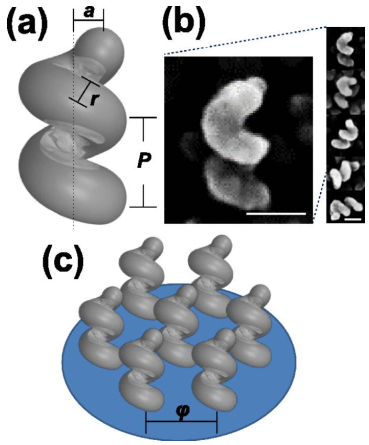

Figure 2.6: (a) Model of a plasmonic nanohelix showing the critical dimension for pitch, major radius, and minor radius as P, a, and r, respectively; (b) On right: 5 SEM images of different individual Cu/Ag helices at different orientations to show morphology; top image enlarged; scale bar 50 nm; (c) schematic of an array of helices with the edge of the hexagonal pattern marked as φ. Figure reprinted from [23].

terials (all the measurements were carried out together with J.G. Gibbs) different sets of samples have been grown, varying the shape or the mutual spacing of the helices. During the depositions, the substrates were placed in the GLAD vacuum chamber, which was evacuated to 10^{-6} mbar. The substrate holder was tilted to a grazing angle so that the substrate surface normal forms an angle of ($\sim 85°$) with the vapour flux direction. This large angle ensures that the growth of the material will be restricted to the nanodots on the substrate due to the shadowing effect [58]. The substrate is rotated by a motor during the deposition, as is necessary for helix formation. The rate at which the motor rotates, is controlled by a computer which relates the amount of material being deposited to the angular frequency of the spinning substrate. Therefore, the rotation rate controls the helix pitch (P) and the major radius (a), which are proportional to each other. Figure 2.7 shows cross section SEM images of five samples of copper nanohelix arrays with varying P; the length is held constant at $h \sim 100$ nm. It is clear that the morphologies are different for each pitch, $P = 20, 40, 60, 80$ and 100 nm in Figures 2.7 (a)-(e), respectively. The length of the helix arrays is held

constant in order to reduce effects of broadening of the wire radius, r, which is typically seen with GLAD films and also to try to keep the absorption constant.

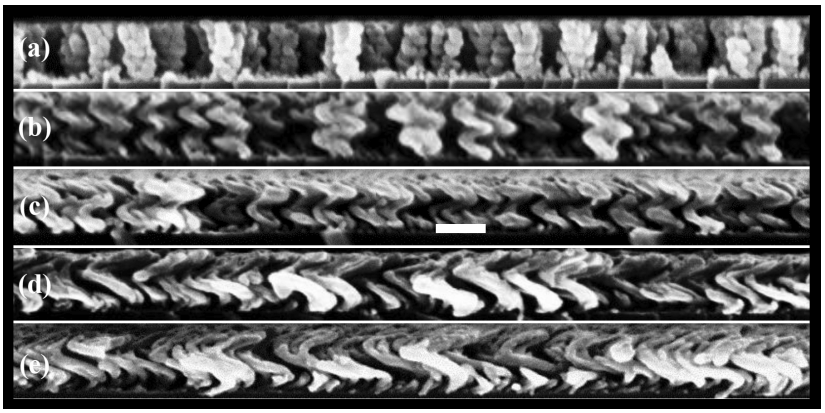

Figure 2.7: Side-view SEM images of 5 different pitch sizes for Cu nanohelices: (a) 20 nm, (b) 40 nm, (c) 60 nm, (d) 80 nm, (e) 100 nm. Scale bar is 100 nm. Figure reprinted from [23].

It is evident that $P \propto a$ in the GLAD process. The proportionality between P and a is derived by taking multiple measurements from cross-section SEM images like the ones shown in Figure 2.7, and the results are fitted linearly by the approximate relation $a \propto 0.3P$, as derived from the plot shown in Figure 2.8.

2.4 Circular dichroism measurements and comparison with simulations

The CD responses were reported in degrees of ellipticity defined by $\tan\theta = 2\frac{I_L - I_R}{I_L + I_R}$. It follows that pure circular and linear polarization states correspond to $\tan\theta = \pm 1$ and $\tan\theta = 0$, respectively. Even for small probe beams our measurements are made on many millions of nanohelices aligned in the same direction with a typical surface number density of $\sim 240\ \mu\text{m}^{-2}$.

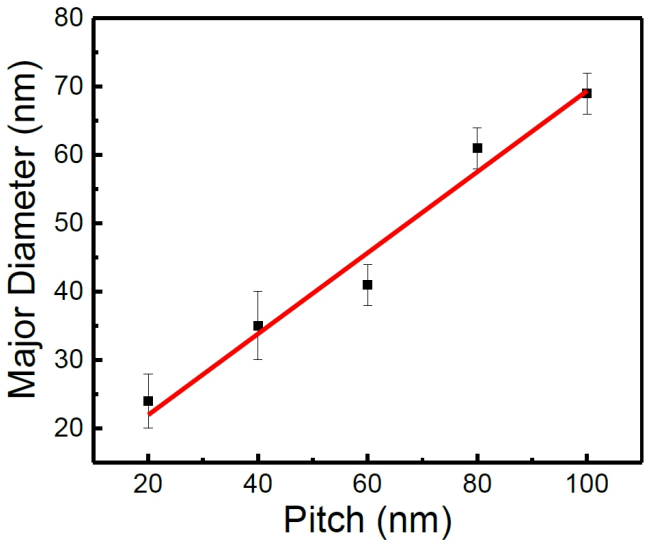

Figure 2.8: Relationship between the major diameter (2a) of Cu nanohelices against the pitch (P). Figure reprinted from [23].

The numerical analysis of the plasmonic nanohelices, discussed in section 2.2, predicts a CD spectral dependence upon P and a; namely, as P increases a increases too, the CD peaks are expected to red-shift [65]. Here the relationship of $P \propto a$ with respect to the resulting CD spectrum is explored experimentally using Cu helix arrays. These results are to be compared with numerical simulations. The helices on each substrate are $h = 110$ nm in total height but with varying P (Figure 2.7). The deposition process with different P does lead to some morphological variations in size and shape. For example, as the structure becomes longer, the minor radius of the helix expands slightly. This effect is well known for the GLAD technique and depends on the material that is deposited [68]. It is important to note that r has been shown numerically to have a large effect on the optical response. All helix arrays are grown here to the same overall length and nominally only P is gradually increased from 20 nm to 100 nm, in increments of 20 nm. The broadening of the minor radius should therefore be uniform across all samples. However, to reproduce correctly the spectra which were measured, it was necessary to consider the relationship between $a \propto 0.3P$ in the numerical simulations too.

2.4.1 Pitch and major radius

Figure 2.9a shows the absolute CD spectra measurements carried out on samples of Cu helices aligned along the direction of the incident light. From the normalized spectra in Figure 2.9b the negative CD peaks red-shift with increasing P. The short-wavelength peak is negative and quite pronounced in all of the samples, and for $P = 80$nm there is $-6°$ of ellipticity at $\lambda = 700\,\text{nm}$.

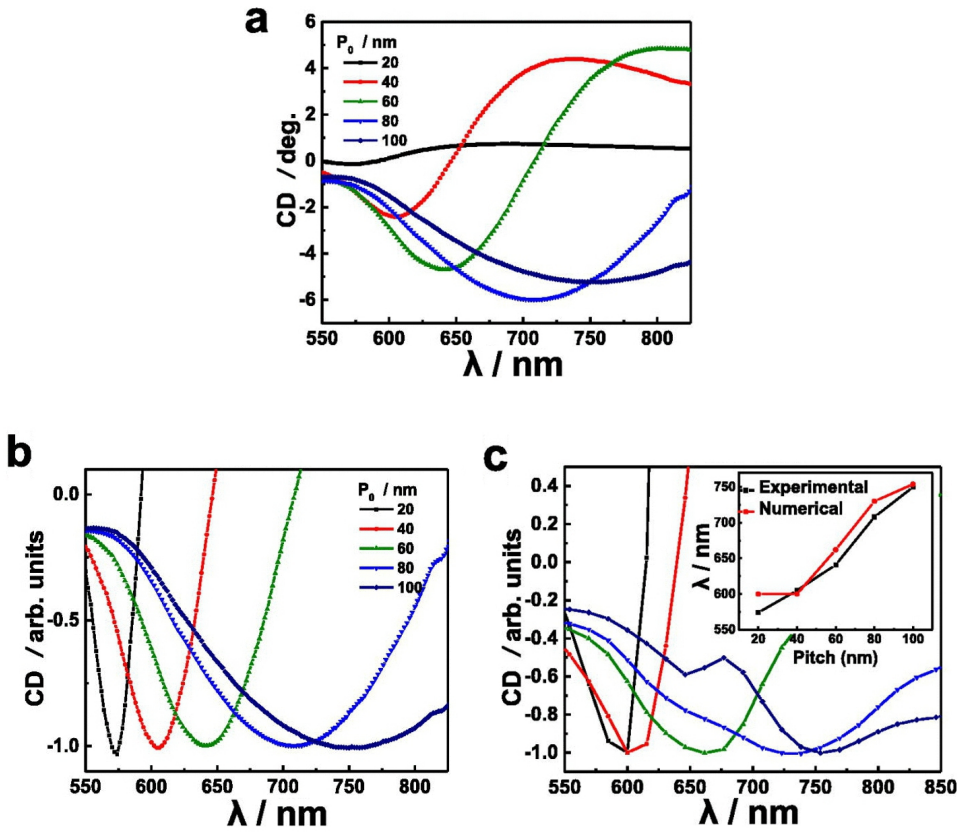

Figure 2.9: (a) CD spectra for Cu helices on a glass substrate with five different lengths of pitch (P) indicating a red-shift with respect to an increase in P, as measured from samples with $P = 20, 40, 60, 80, 100\,nm$; (b) normalized CD spectral peaks for the same Cu nanohelices; (c) normalized CD from the numerical simulations carried for the five Cu helices. Here the inset shows the negative peak position vs. pitch size for experiment and simulation in black and red, respectively. Figure reprinted from [23].

This is orders of magnitude larger than what is typically measured for molecules, where CD measurements are usually reported in mdeg. A broadening of the spectral width is also clearly visible. The peak is dramatically shifted and it is also the only peak which could be analysed in this spectral range with the JASCO-810 spectropolarimeter, as the positive peak for the $P = 80$ and $100\,nm$ are red-shifted to the IR. Figure 2.9b and Figure 2.9c compare the normalized results of the experimental data and the numerical simulations, respectively. Taking into account the mutual dependence $a \propto 0.3P$, there is a very good agreement between the two, with regards to the shift in the CD peak. This means that the appearance of the CD spectrum is due to the shape of the helices. Further, if one calculates the quantity $\zeta_{RCP} = \Delta\lambda/\Delta a$ as the slope of the line fitting the data shown the in inset of Figure 2.9 (c), this results in $\zeta_{RCP} \simeq 7.5$, which is slightly higher than the equivalent ζ_{RCP} calculated from the numerical simulations for an independent variation of the major radius, a, in section 2.2 and consistently shows a smaller contribution to the red-shift given from the joint effect of $a \propto P$ in the real GLAD samples.

2.4.2 Lattice spacing

The effect of varying the separation between individual helices is explored experimentally. In this case, Cu/Ag alloy nanohelix arrays are used. By growing Cu/Ag alloy structures, as opposed to pure Cu presented in Figure 2.7, it is possible to move the CD peak to shorter wavelengths, because the plasmon resonance of Ag occurs at shorter wavelengths compared with Cu. Increasing the spacing between helices is expected to reduce the total extinction. In what follows we will focus on the relationship of the optical density (OD) and the CD to the surface density of the helices by changing the seed spacing with BCML. Wu et al. used the finite-difference time-domain (FDTD) method to study left-handed (here not the chiral sense) helical metamaterials with the aim of producing an effective circular polariser. They showed that the quality of a helical metamaterial polariser

of this form improves by increasing the length of the helix, decreasing the diameter, and/or increasing the spacing between helices [67].

Coupling the deposition process with BCML permits us to alter each of these parameters. Changing the spacing permits the strength of the overall absorption to be adjusted, which is useful in the case of plasmonic materials that are lossy [69]. Figure 2.10(a) shows that by increasing the spacing of the seed pattern, samples show less total OD, as is expected. The total extinction is measured for five lattice spacings $\varphi = 53, 62, 69, 76, 81$nm. The OD in Figure 2.10(a) decreases noticeably for $\varphi = 53, 62, 69, 76$ nm, but then increases again for $\varphi = 81$nm. SEM observations indicate that if $\varphi >$ 80 nm, nanohelix formation between seeding points becomes significant, and helix surface density begins to increase indicating that the spacing can only be adjusted to values between about $\varphi = 50$–80 nm, although smaller separations could be used.

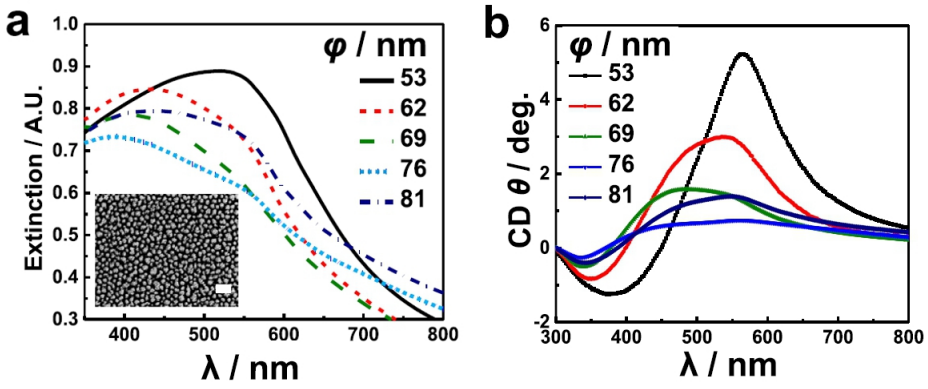

Figure 2.10: (a) Total extinction curve for linearly polarized light for substrates with Cu/Ag alloy nanohelices with different seed spacings of $\varphi = 53, 62, 69, 76, 81$nm; inset: SEM top-view with scale-bar 200 nm for $\varphi \sim 76$ nm spacing; (b) the effect of changing seed separation on CD which is greatest for the most closely-packed helices and decreases with increasing distance until $\varphi = 76$ nm; the optical activity for $\varphi = 81$ nm again increases due to the inability of the seeding at large distances to properly shadow adjacent seeds. Figure reprinted from [23].

Although increasing φ does in fact reduce loss, the CD decrease can be seen in Figure 2.10b . Also, the spectral peaks red-shift with decreasing φ which may be a result of plasmonic coupling [70, 71]. The decreased optical activity with increasing φ presumably occurs due to the reduction in surface density of the nanohelices, as is expected. The CD begins to increase for the $\varphi = 81\,nm$ case as the larger spacing leads to 'random' unseeded helices forming in between the seed points. However, although this increase is present, the degree of the optical activity does not reach the same magnitude as for either $\varphi = 62$ or $69\,nm$ which are in fact properly seeded and regularly ordered, suggesting improved uniformity and structural fidelity. Also, the spectral peaks are more clearly defined in the case of properly seeded nanohelix arrays. From these observations it is possible to conclude that nanoseeding makes a significant difference in the quality of each helix array and its respective chiroptical response. However, there is an inevitable trade-off between loss and strength of the CD. The strongest signals arise in the most closely packed, regularly ordered helix arrays, but in this case loss is also highest.

2.5 Discussion

In conclusion, it has been demonstrated that the optical activity of chiral plasmonic nanohelices can be tuned by adjusting the deposition parameters of a dynamic shadowing growth physical vapor deposition technique, and the chiroptic spectral responses are altered by adjusting the individual helix shape and the spacing between the helices. Spectral red-shifting for larger pitches, which is linearly proportional to the helix major radius, is complimented by numerical simulations using DDSCAT. Also, a trade-off between increasing optical activity and simultaneously increasing loss is inevitable for plasmonic materials. Optical activity is larger with closer helix spacing, but these samples also show the greatest loss. Nevertheless, it is clear that regular ordering is indeed important for sample quality. The

wafer-scale fabrication of tunable hybrid and plasmonic nanostructures will enable possible applications such as chiral light modulation and chiral sensing as well as other photonic systems to be explored. These results prove that the optical activity in chiral-plasmonic metamaterials can be tuned and maximized during the GLAD fabrication. The extinction is determined by the imaginary part of the index of refraction, but the real and imaginary components of the index of refraction are dimensionless quantities that relate directly to the observables of CD and OR, which are analytical in the wavelengths domain and therefore connected by the general relations of Kramers-Kronig. As clearly discussed in Ref. [72], these relations permit a comparison between the real and imaginary component of $\delta\tilde{n}$. The generalized KK-relations that consider the logarithm of the observables and that include a Blaschke multiplier, permit a direct conversion between OR and CD spectra. However, in practice the KK transform is not accurate in the visible due to insufficient experimental data at shorter wavelengths. For the specific interests of this thesis, it follows that the presence of strong CD implies also the presence of strong CB. The direct measurement of the index of refraction $\tilde{n}_{\substack{L \\ R}}$ is not a simple measurement. In Chapter 3 it will be shown how a laser interferometer can be adoperated for these measurements. In Chapter 4 the refractive indices describing the nanohelix arrays will be examined in more detail.

Chapter 3

Circular polarization laser interferometer

Existing methods for direct measurement of circular birefringence (CB) like optical rotation, only give information about the difference of the refractive indices for left- and right- circularly polarized light $\delta n = (n_L - n_R)$. A new type of polarization interferometer was therefore developed based on the design of the Jamin-Lebedeff interferometer [73, 74] to be able to determine independently n_L and n_R. The Jamin-Ledebeff interferometer uses linearly polarized light and has been used to measure the refractive index of a pigmented biological tissue [75], or crystals [76] and also in the case of metamaterials [77].

In this chapter, Jones calculus is used to analyse the physical principles of the laser interferometer setup. The operation of the circularly polarization interferometer is tested on a uniaxial cholesteric liquid crystal sample. The measurements presented herein have been carried out with the help of Dr. A. Sanchez-Castillo and have in part been published in [24]. A direct measurement of $n_{L,R}$, the real part of the indices of refraction in the region of Bragg reflection, could be obtained as a function of temperature and thus during the phase change of the LC from cholesteric to isotropic.

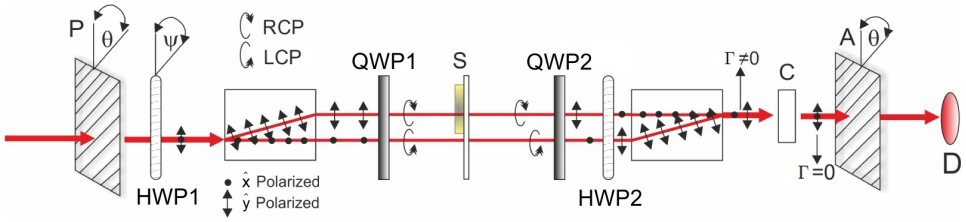

Figure 3.1: Scheme of the circular polarization setup, the various optical components are explained in the text. Figure adapted and reprinted from [24].

3.1 Jones model of the laser interferometer

The interferometer's scheme is shown in Figure 3.1. The radiation source used in this setup is a HeNe laser, which is used in its intensity stabilization mode. In this section each single optical component is described and its function is analysed in order to describe the working principle of the interferometer. In the following the formalism of the Jones calculus is used without recalling all the mathematical model that set the connection with electrodynamics. The general model of the Jones calculus is discussed in Ref.s [34, 78, 79].

3.1.1 Preparation of two coherent beams with orthogonal polarization

The euclidean spatial system of reference that is used here is a right handed one, with the unit vectors $\mathscr{F} \equiv (\hat{x}, \hat{y}, \hat{z})$ that form a complete basis for it. The laser light is with its wave-vector $\vec{k}$ parallel to the direction $\hat{z}$ with a linear polarization along the $\hat{x}$ axis. The laser beam is transmitted first through a polariser (P) and then through a half-wave plate retarder (HWP1) before being separated by $4.2mm$ along the $\hat{y}$ direction in two beams with orthogonal polarization states by a beam displacer calcite crystal (BD1). With this set of optics one can first project the initial linear polarization from the laser along the direction of the axis of polarization of P rotated by an angle θ with respect to $\hat{x}$. The Jones matrix for a polariser oriented by

an angle θ on the $(\hat{x}, \hat{y})$ plane is:

$$P(\theta) = \mathscr{R}(-\theta)P(0^\circ)\mathscr{R}(\theta) = \begin{pmatrix} \cos^2\theta & \sin\theta\cos\theta \\ \sin\theta\cos\theta & \sin^2\theta \end{pmatrix} \tag{3.1}$$

where $P(0^\circ)$ is

$$P(0^\circ) = \begin{pmatrix} 1 & 0 \\ 0 & 0 \end{pmatrix} \tag{3.2}$$

and $\mathscr{R}$ represents the 2D rotation transformation

$$\mathscr{R}(\theta) = \begin{pmatrix} \cos\theta & \sin\theta \\ -\sin\theta & \cos\theta \end{pmatrix}. \tag{3.3}$$

For a retardation plate rotated by the azimuthal angle θ:

$$W(\theta) = \mathscr{R}(-\theta)\, W_0\, \mathscr{R}(\theta) \tag{3.4}$$

where

$$W_0 = \begin{pmatrix} e^{-i\Gamma/2} & 0 \\ 0 & e^{i\Gamma/2} \end{pmatrix} \tag{3.5}$$

where Γ represents the phase retardation between the fast and slow axis introduced by the wave-plate. In the case of a quarter wave-plate it is important to be able to distinguish the fast axis from the slow axis of the crystal, in order to know the sign of the circular polarization that is generated.

Let's explicitly calculate what is the effect of the different optics. Before P the Jones vector of the $\hat{x}$-polarized light in the $(\hat{x}, \hat{y})$ plane is simply:

$$|J> = \begin{pmatrix} J_x \\ J_y \end{pmatrix} = \vec{E}_0/|\vec{E}_0| = \begin{pmatrix} 1 \\ 0 \end{pmatrix}, \tag{3.6}$$

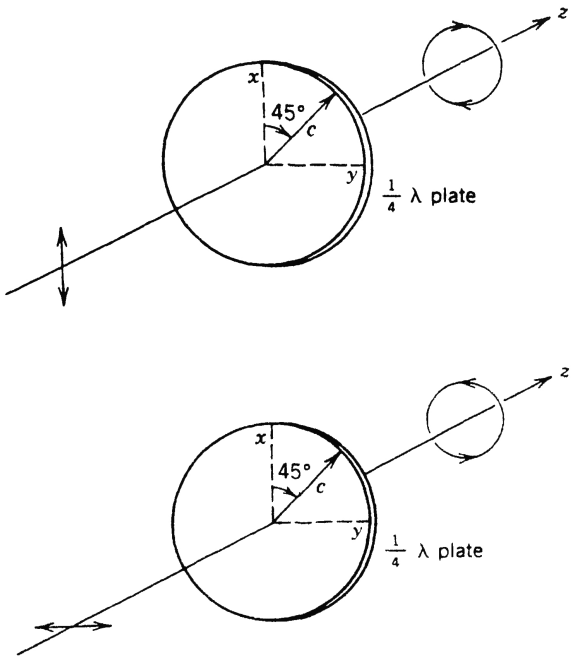

Figure 3.2: Action of a quarter waveplate with $\theta = 45°$, on incident linearly polarized beams along the $\hat{x}$ or $\hat{y}$ directions. c marks the orientation of the slow (extraordinary) axis of the crystal. Figure adapted and reprinted from [78].

and after P:

$$\begin{aligned} \vec{E_1} &= \begin{pmatrix} \cos^2\theta & \sin\theta\cos\theta \\ \sin\theta\cos\theta & \sin^2\theta \end{pmatrix} \vec{E_0} = \\ &= |\vec{E_0}|\cos\theta \begin{pmatrix} \cos\theta \\ \sin\theta \end{pmatrix}. \end{aligned} \tag{3.7}$$

P can be used to control the total intensity of the transmitted beam, which will be given by the projection of the amplitude of $|\vec{E_0}|\cos\theta$ along the direction of the transmission axis of P. After the HWP1 the electric field of the beam will result in:

$$\begin{aligned}\vec{E_2} &= \mathscr{R}(-\theta)\begin{pmatrix}\cos^2\psi-\sin^2\psi & 2\sin\psi\cos\psi\\ 2\sin\psi\cos\psi & \sin^2\psi-\cos^2\psi\end{pmatrix}\mathscr{R}(\theta)\,\vec{E}_1\\ &= \mathscr{R}(-\theta)\begin{pmatrix}\cos 2\psi & \sin 2\psi\\ \sin 2\psi & -\cos 2\psi\end{pmatrix}\mathscr{R}(\theta)\,\vec{E}_1.\end{aligned} \tag{3.8}$$

Defining now the basis $\mathscr{F}' \equiv (\hat{x}', \hat{y}', \hat{z}')$ rotated along the $\hat{z}$ axis by θ so that $\hat{x}' \parallel \vec{E}_1$ one can see the effect of the half wave-plate rotated with the fast axis by an angle ψ. An incoming linear polarization state which is oriented along the $\hat{x}'$ axis, is then rotated by -2ψ.

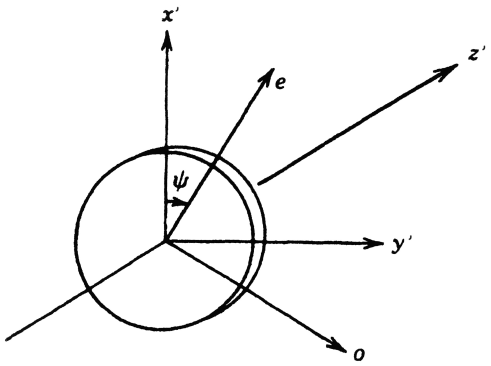

Figure 3.3: Frame of reference and positive azimuthal angle ψ between the $\hat{x}'$ axis and the extraordinary axis of the wave-plate. Figure adapted and reprinted from [78].

BD1 splits splits the light into two parallel beams separated by $4.2mm$ that are respectively polarized along the $\hat{x}$ and $\hat{y}$ direction. The two components of the Jones vector written with respect to the $\mathscr{F}$ basis, resulting from the combined action of P and HWP1, are then written as

$$\begin{aligned}\vec{E_2} &= |\vec{E_0}|\cos\theta\,\mathscr{R}(-\theta)\begin{pmatrix}\cos 2\psi\\ \sin 2\psi\end{pmatrix}\\ &= |\vec{E_0}|\cos\theta\begin{pmatrix}\cos\theta\cos 2\psi-\sin\theta\sin 2\psi\\ \sin\theta\cos 2\psi+\cos\theta\sin 2\psi\end{pmatrix}.\end{aligned} \tag{3.9}$$

The combined selection of θ and ψ can then be used to obtain two parallel coherent beams with orthogonal linear polarizations with the same intensity.

3.1.2 From two beams with orthogonal linear polarizations into orthogonal circular polarizations

One single quarter wave-plate is used for the two incident beams with mutually orthogonal linear polarizations, so that they are transformed in two circular polarizations of opposite hand. For this the quarter wave-plate QWP1 should be oriented with its axis at 45°.

The Jones matrix in the case of a quarter wave-plate retarder ($\Gamma = \pi/2$) with its fast axis rotated by an angle θ with respect to $\hat{x}$, will result in

$$W(\theta) = \begin{pmatrix} \cos^2\theta + i\sin^2\theta & (1-i)\cos\theta\sin\theta \\ (1-i)\cos\theta\sin\theta & i\cos^2\theta + \sin^2\theta \end{pmatrix} \tag{3.10}$$

For the wave-plate rotated by $\theta = 45°$:

$$W(45°) = \frac{1}{2}\begin{pmatrix} 1+i & 1-i \\ 1-i & 1+i \end{pmatrix} \tag{3.11}$$

which acts on the Jones vector for the two states of incoming linear polarizations

$$W(45°)\begin{pmatrix} 1 \\ 0 \end{pmatrix} = \frac{1}{2}\begin{pmatrix} 1+i \\ 1-i \end{pmatrix} = (1-i)\begin{pmatrix} 1 \\ -i \end{pmatrix} \tag{3.12}$$

$$W(45°)\begin{pmatrix} 0 \\ 1 \end{pmatrix} = \frac{1}{2}\begin{pmatrix} 1-i \\ 1+i \end{pmatrix} = (1+i)\begin{pmatrix} 1 \\ i \end{pmatrix} \tag{3.13}$$

Instead, in the case of the wave-plate rotated by $\theta = -45°$

$$W(-45^\circ) = \frac{1}{2}\begin{pmatrix} 1+i & i-1 \\ i-1 & 1+i \end{pmatrix} \tag{3.14}$$

and the two orthogonal linear polarizations along $\hat{x}$ and $\hat{y}$ will result in

$$W(-45^\circ)\begin{pmatrix} 1 \\ 0 \end{pmatrix} = \frac{1}{2}\begin{pmatrix} 1+i \\ i-1 \end{pmatrix} = (1-i)\begin{pmatrix} 1 \\ i \end{pmatrix} \tag{3.15}$$

$$W(-45^\circ)\begin{pmatrix} 0 \\ 1 \end{pmatrix} = \frac{1}{2}\begin{pmatrix} i-1 \\ i+1 \end{pmatrix} = -(1+i)\begin{pmatrix} 1 \\ -i \end{pmatrix} \tag{3.16}$$

This means that the left-circular polarization (LCP, with unit vector defined as $|L>= \frac{1}{\sqrt{2}}\begin{pmatrix} 1 \\ i \end{pmatrix}$) and right-circular polarization (RCP, with unit vector defined as $|R>= \frac{1}{\sqrt{2}}\begin{pmatrix} 1 \\ -i \end{pmatrix}$) are generated at the same time. In the case of a quarter wave-plate retarder, the distinction of the slow axis from the fast axis is crucial in order to know the absolute sign (hand) of the circular polarization. This is seen by writing down the Jones matrix for a $\lambda/4$ wave-plate rotated with the fast axis by $\theta = 45^\circ + 90^\circ$, which is equivalent of inverting the two axes of the retarder. The Jones matrix results in:

$$W(45^\circ + 90^\circ) = \frac{1}{2}\begin{pmatrix} 1+i & i-1 \\ i-1 & 1+i \end{pmatrix} = W(-45^\circ) \tag{3.17}$$

Now we know how the two separated parallel beams with orthogonal linearly polarized can be transformed into two orthogonal circular polarizations using one single quarter wave-plate retarder. Is it also possible to return the two beams from circular to linear polarizations with another quarter wave-plate? In order to demonstrate this we calculate the effect of the quarter wave-plate rotated by $\theta = -45^\circ$ applied to the results of (3.12) and (3.13):

$$W(-45^\circ)\left[(1-i)\begin{pmatrix}1\\-i\end{pmatrix}\right]=\frac{1-i}{2}\begin{pmatrix}1+i & i-1\\ i-1 & 1+i\end{pmatrix}\begin{pmatrix}1\\-i\end{pmatrix}=2\begin{pmatrix}1\\0\end{pmatrix} \tag{3.18}$$

$$W(-45^\circ)\left[(1+i)\begin{pmatrix}1\\i\end{pmatrix}\right]=\frac{1-i}{2}\begin{pmatrix}1+i & i-1\\ i-1 & 1+i\end{pmatrix}\begin{pmatrix}1\\i\end{pmatrix}=2\begin{pmatrix}0\\1\end{pmatrix} \tag{3.19}$$

This demonstrates that the two beams recover the same linear polarization that they had just before the QWP1 when they propagate into a second $\lambda/4$ wave-plate, which we call QWP2, with an equivalent and opposite rotation of the azimuth angle in the direction of propagation of the beams. The same scalar multiplier resulting in front of the final linearly polarized states, means that there is no relative phase difference between the two beams introduced by the combined action of QWP1 and QWP2 with opposite rotations of the azimuthal angles with respect to frame $\mathscr{F}$.

3.1.3 Recombination of the two beams and interference

The laser beams that have been separated after BD1 can be recombined using an equivalent calcite beam displacer that we call BD2. Both of the BDs are mounted on anti-vibration and optical translation stages. To obtain the right alignment of the linear polarizations of the beams to the crystal plane of the BD2 crystal it is necessary to use a second $\lambda/2$ wave-plate retarder (HWP2), which is positioned between QWP2 and BD2 and that rotates the two polarizations by 90°.

Before any measurement can be carried, the interferometer needs to be set in its offset condition: it is crucial that, without any sample aligned in the interferometer, the two beams are propagated through all the optical elements without any difference in phase. With all the optical elements in position, maximizing the interference of the two beams while acting on

the translation stages where the BDs are mounted, gives the possibility to finely align the mutual orientation of the calcite crystals of BD1 and BD2. This procedure can be used to obtain the same optical pattern of the two beams in the overall dynamics of the laser beams between the source and the detector. When the two beams are in a fully constructive interference condition, the interferometer is set at offset.

BD2 then recombines the two beams, but the polarization of the outcoming beams is orthogonal and therefore cannot interfere. The interference of the two beams can be measured when a second polariser (analyser, A) is used to project the polarization of both of the beams along the same direction (Eq. (3.7)). Then a photodetector can be used after A oriented with the transmission axis at the azimuthal direction θ, as previously defined with respect to the $\mathscr{F}$ frame of reference, to obtain a measurement of the intensity $I(\theta)$ of the interference of the two coherent beams.

3.1.4 Measurement of the phase retardation from a material in the path of one of the beams

Once the interferometer is at offset then the two beams have the same intensity and accumulate the same phase when propagated from the source to the detector. In what follows the electric field results from the composition of the two linearly polarized waves along $\hat{x}$ and $\hat{y}$ that are propagated after BD2, are written as $\vec{E_x}$ and $\vec{E_y}$ as monochromatic planar waves with angular frequency $\omega = 2\pi c/\lambda$. The vector sum of the two electric fields generated by the two coherent laser beams will be of the form

$$\vec{E} = \vec{E_x}\cos(\omega t - \vec{k}\cdot\vec{z}) + \vec{E_y}\cos(\omega t - \vec{k}\cdot\vec{z}). \tag{3.20}$$

At the detector $z = 0$

$$\vec{E} = \vec{E_x}\cos(\omega t) + \vec{E_y}\cos(\omega t) \tag{3.21}$$

Assuming that the $\hat{y}$-polarized beam passes a material and acquires the phase retardation (Γ) when it reaches $z = 0$, so that

$$\vec{E} = \vec{E_x}\cos(\omega t) + \vec{E_y}\cos(\omega t + \Gamma) \tag{3.22}$$

The vectorial sum of the electric field of the two beams will be an elliptical polarization with a precise handedness and ellipticity. In particular Figure 3.4 summarizes the polarization state corresponding to different phase retardations of the wave polarized along $\hat{y}$. In the case that $|\vec{E_x}| = |\vec{E_y}|$, for $\Gamma = (2k+1)\pi/2$, the polarization will be circular.

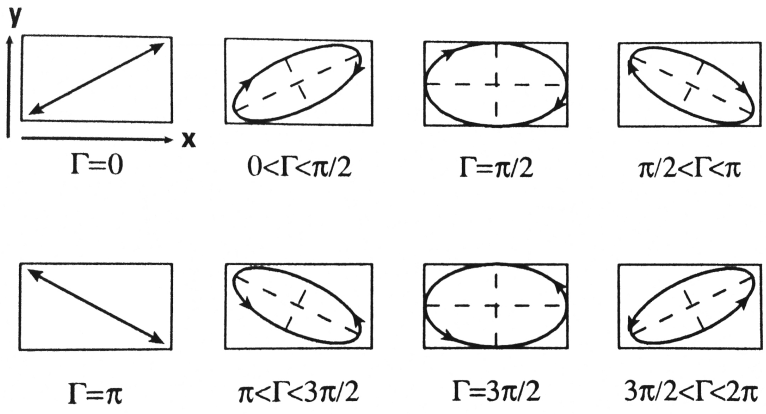

Figure 3.4: Various elliptical polarization waves for different phase delays Γ. Figure adapted and reprinted from [34].

With the nanohelix arrays that are produced in the GLAD system on SiN suspended films can also be deposited. The interferometer can be used to measure the chiral index of refraction of the metamaterial, obtained with such an array of plasmonic nanohelices. If one of the beams between the QWPs, is propagated through a chiral metamaterial film and the other beam is propagated through an equivalent clean SiN substrate (i.e. with the same thickness), the phase accumulated because of the transmission through the

metamaterial can be measured directly. This phase difference (Γ) will be in function of the index of refraction (n) of the metamaterial as

$$\Gamma = \frac{2\pi(n - n_{ref})d}{\lambda} \tag{3.23}$$

with d the thickness of the nanostructured film of nanohelices deposited and n_{ref} is the real part of the index of refraction of the reference material which is present on the reference beam of the interferometer, when no specific reference is present this will be the index of refraction of air $n_{ref} = n_{air}$.

Once circular polarizations are generated between QWP1 and QWP2, as described in section 3.1.2, the amplitude of the outcoming beams can be set to be equal acting on the HWP1 as described previously in section 3.1.1. Γ can be measured acting on a linearly birefringent crystal (compensator, C): one is having a full-wave polarization dependent compensator, for instance an LCC-1113A from THORLABS that can add a phase depending on which of the polarization axes is aligned along its slow axis. What is actually being measured is the intensity (I_{out}) after A, which projects the two orthogonal linear polarization at the output of the preceding set of polarization optics, along the same direction along A. In terms of the two intensities $I_x = \frac{\|\vec{E}_x\|^2}{2}$ and $I_y = \frac{\|\vec{E}_y\|^2}{2}$, the intensity of the interfering beam with A positioned at an azimuthal angle θ will be:

$$I(\theta) = I_x \cos^2\theta + I_y \sin^2\theta + 2\sqrt{I_x I_y}\sin\theta\cos\theta\cos\Gamma \tag{3.24}$$

$I_x = I_y = I_0$ can be obtained by acting on the HWP1. When A is positioned with the polarization axis at either $\pm 45°$, then:

$$I(\pm 45°) = I_0(1 \pm \cos\Gamma). \tag{3.25}$$

It is more convenient to measure a photocurrent for a destructive interference than for a constructive interference and the choice of the angle of A

(between $\pm 45°$) helps by introducing or not introducing a phase of half a wave between the two interfering beams.

3.1.5 Characterization of a liquid crystal compensator and the wave-plates

LCC-1113A

The liquid crystal variable retarder LCC-1113A can act as a variable retarder, depending on its applied voltage, with phase retardation introduced between its fast and slow axis from < 0.1 waves to > 1 full wave. When the empty interferometer is set at offset and with the LCC-1113A aligned with the fast and slow axes along the direction of the two orthogonal $\hat{x}$, $\hat{y}$ polarizations propagated out of BD2, then it is possible to characterize the retardation introduced by the variable compensator in function of the applied voltage. Unfortunately the characterization data provided by the supplier (*THORLABS*), did not match the experimentally observed retardations.

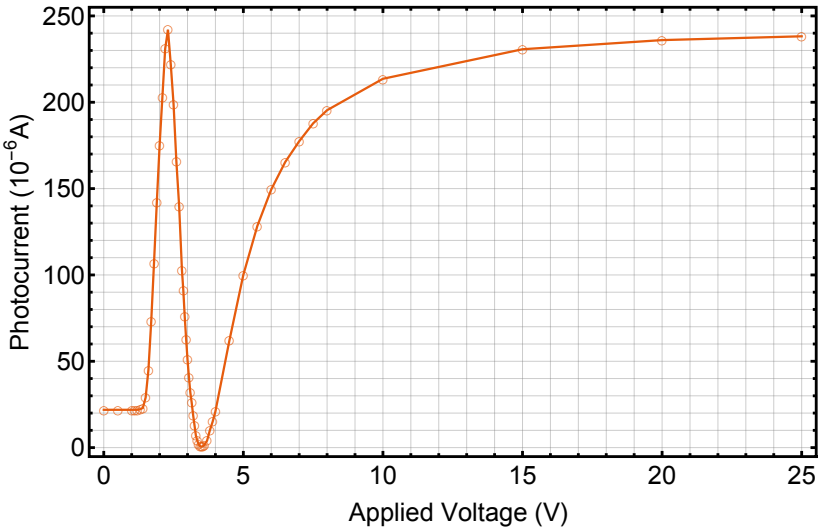

Figure 3.5: Measurements of the interferometer's photocurrent, showing the effect of the action of the LCC-1113A.

The linear birefringence of the LCC is characterized as it follows: first the LCC is positioned along the path of the two collinear laser beams after BD2, with the slow and fast axes respectively aligned with the axes of linear

polarization ($\hat{x}$, $\hat{y}$). Then a voltage is applied to the device, which will result in a change of the linear birefringence between the two axes. The wave with polarization along the slow axis will thus experience a higher index of refraction and will travel slower. The birefringence can be decreased by raising the applied voltage. A voltage V between 0 V and 25 V can be selected on the LCC's driver. At the polarization interferometer's wavelength the measurement of the interference, recorded after the A is shown in Figure 3.5.

A very small birefringence is observed at high voltages ($V = 25$ V), where the photocurrent is maximal. A minimum corresponding to a half-wave retardation is observed at the applied voltage of $\simeq 3.5\ V$. The maximum around $\simeq 2.2\ V$, corresponds to a full-wave retardation. A phase retardation of ~ 1.4 waves is then observed for $\lesssim 1.4\ V$. Figure 3.6 shows the corresponding values of retardation for the LCC-1113A.

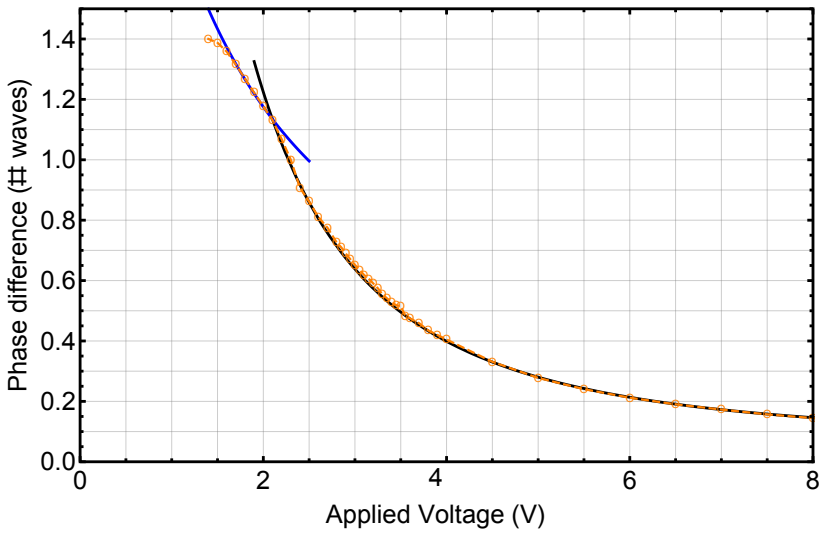

Figure 3.6: Measurement of the retardation of the liquid crystal compensator. In orange are shown the measurements obtained from the laser interferometer, black and blue lines are analytical fits that best characterize the LCC-1113A.

Using Wolfram Mathematica an analytical relation has been fitted using a model of the retardation for $\Gamma(V)$ of this form:

$$\Gamma(V) = \frac{A}{(V - V_0)^{\alpha}} + B \tag{3.26}$$

With the given 4 free parameters (A, B, V_0, α), two main domains can be identified where the model is consistent with the measured phase retardation, marked in Figure 3.6 with the black and blue functions. The fitting parameters are given in Table 3.1 for different domains of V_d.

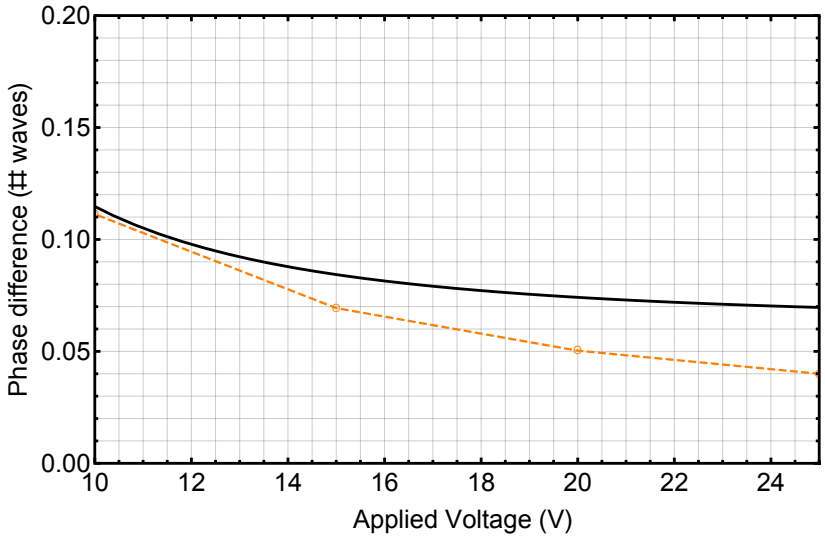

Figure 3.7: Measurements of the phase introduced with the LCC-1113A. A detail of the difference between the modelled response and the measurements at applied driver's tensions 10 V $<$ V_d $<$ 25 V

For values $V_d > 12$ V The model is slightly less consistent, but in practice these values correspond to values of introduced retardation that are not useful for the subsequent measurements as they correspond to very small retardations of a fraction of wave of $0.05 < \Gamma < 0.1$. On the other hand, for values of $V_d < 1.6$ V as is shown in Figure 3.5, the LCC-1113A reaches a constant value of $\Gamma \sim 1.4$ waves.

Important for the purpose of the interferometry measurements, is the alignment of the different wave-plate retarders, including the LCC, and this is described in the next section.

Axes of the wave-plate retarders

Crucial for the purposes of the subsequent measurements is the orientation of the retarders. The determination of the axes of the wave-plates is easily obtained with a coupled cross polariser configuration. However, the correct

Applied voltage (V_d)	A	B	V_0	α
$1.6\ V < \ V_d\ < 2.1\ V$	3.6	0.059	-0.9	1.1
$2.1\ V < \ V_d\ < 12\ V$	12.3	0.063	-0.8	2.3

Table 3.1: Calculated parameters for the best fit for the model of the retardation of the LCC-1113A to the measured values from the polarization interferometer.

distinction between the fast and slow axes, in particular for the QWPs is of crucial importance in the polarization interferometer.
The wave-plates used in this interferometer are all zero-order wave-plates already mounted. These optics come with a marking on the mount but it is not sufficient to rely on this marking. In principle, one could determine the handedness of the circular polarization state by introducing a circular absorber. However, the circular dichroism of most samples is generally too weak to be useful.

Based on the phase difference introduced in reflection between the in plane and the out of plane linear polarizations characteristic of a metal surface, Logofatu [80] reported a method for the determination of the fast and slow axis of a wave-plate. This method was adopted in this work for the determination of the axes of birefringence of the quarter wave-plates. The metal surface used here was obtained by sputtering 500 nm of aluminium on a silicon substrate by Reinhart Völker. The direction of the slow and fast axis of birefringence were then determined by the method described in Ref.s [80, 81], for each wave-plate used in the polarization interferometer.

In Figure 3.8 is shown a scheme of the setup used for the determination of the slow and fast axis of the wave-plates used in the interferometer. The HeNe laser was also adoperated here. In turn, all the QWP1, QWP2 and the LCC (with an applied voltage corresponding to a quarter-wave retarder) where measured with either of the birefringence axes oriented along the component $\hat{p}$ (out of plane) or $\hat{s}$ (in plane), defined with respect to the surface of the aluminium mirror. The laser beam is incident at an angle of

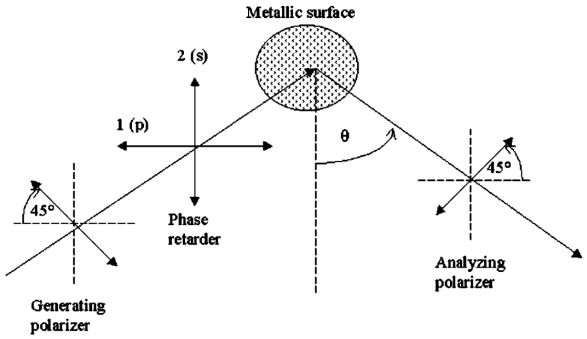

Figure 3.8: Scheme of the optics used to determine the fast and slow axis of the wave-plate retarders. Reprinted from [80].

$\sim 30°$ on the mirror's surface. The laser light is first propagated through a polariser oriented at $-45°$ with respect to the $(\hat{s}, \hat{p})$. The reflected beam is then propagated through an analyser and the photocurrent is measured by a photodetector. If the real part of the index of refraction of the metallic surface ($n'_{Al}(633 \text{ nm}) = 1.2675$ [39]) is bigger than $n' > 1.0$, then when the fast axis of the probed quarter wave-plate is oriented along $\hat{s}$, the detected photocurrent is always higher than the case when the slow axis is along $\hat{s}$.

3.2 Circular polarization interferometer measurements on a cholesteric liquid crystal

Parts of this section have appeared in the publication
Optics Express, Vol. 22, Issue 25, pp. 31227-31236 (2014). [24]

The interferometer setup was first tested on isotropic solutions (sugar / salt) at different concentrations and gave consistent results with the known models of index of refraction.

Subsequent tests were carried out on a cholesteric liquid crystal (CLC), a cholesteryl oleyl carbonate commercially available from Sigma Aldrich. The optical properties of this compound are known [82, 83]. However a direct measurement of the index of refraction depending on the state of

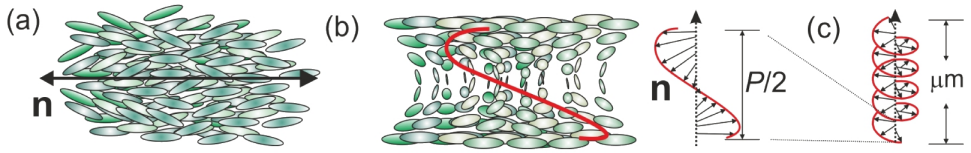

Figure 3.9: Schematic representation the liquid crystals of rod-like molecules. (a) Nematic phase: the molecules are oriented along the director n. (b) Cholesteric phase: spatially twisted alignment with the molecules aligned along helical director lines (red line) with single-turn length P. (c) Typical LC cells can form over several μm and have considerable number of turns.Figure reprinted from [24].

circular polarization not been obtained previously. LCs may be described as partially ordered fluids, where the simplest liquid crystalline phase is called the nematic phase where the rod-like molecules tend to align along a certain director (n) (Figure 3.9). In the cholesteric phase instead, the molecules align along a director that is now with a helical shape [84]. These different phases will also have different optical polarization properties. In particular, optical activity will be expected and therefore a measurable difference in the index of refraction depending on the circular state of polarization, due to the circular birefringence (therefore different velocities of transmission of the wave) with consequent optical rotatory power (ORP) and selective Bragg reflection [85–88].

The dispersion relation of the CLC is shown in Figure 3.10, where the normal modes of propagation k_1 and k_2 respectively for left and right handed polarization states, are schematically represented (Figure 3.10c) together with the effect of the Bragg reflection and ORP in proximity of the Bragg regime. The RCP is expected here to be transmitted almost unperturbed, while the LCP should be strongly reflected (Figure 3.10a). As it was also observed in Ref. [89], where the domain of wavelengths $\lambda \in [650, 720]\ nm$ was considered, a transmission of $\simeq 100\%$ for RCP and a reflection of $\simeq 95\%$ for LCP are expected in this material. As represented qualitatively in Figure 3.10b k_1 changes sign at the frequency ω_B and therefore in the ORP an inversion point appears, which changes the sign of the rotation angle of

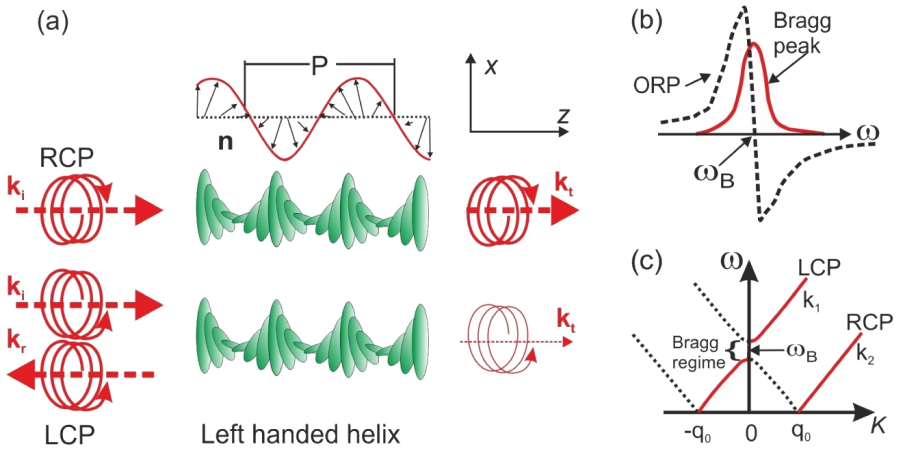

Figure 3.10: (a) Schematic representation of propagation of light, with orthogonal circular polarizations (LCP or RCP), on a CLC with left-handed alignment. In this case RCP is transmitted unperturbed, while LCP is mostly reflected. k_i, k_r and k_t, represent respectively the wavevectors of the incident, reflected and transmitted light. (b) In the proximity of the Bragg regime a peak of reflection, corresponding to the k_1 mode appears (solid line) and the difference in the velocities of propagation of the circular polarizations results in a strong optical rotatory power (ORP). (c) Schematic representation of the normal modes of propagating waves in the CLC. Four polarized modes are present, respectively for k_1 and k_2 being respectively left and right-handed polarized modes, propagating forward (solid lines) and backward (dashed lines). The stop band that appears at the crossing of the four modes is where the Bragg diffraction is present. Figure adapted and reprinted from [24].

the polarization. In terms of a superposition of two orthogonal circularly polarized waves of equal amplitude, this results in a rotation experienced by the resulting linear polarization. This effect of ORP is conventionally measured in units of rad/mm [90]

$$\rho = \frac{1}{2}(k_1 - k_2) = \frac{\pi}{\lambda}(n_L - n_R) \tag{3.27}$$

where $\delta n = (n_L - n_R)$ is due to the circular birefringence of the material. In principle ρ can be measured by simply measuring the angle of rotation of an incoming monochromatic wave with linear polarization and dividing by the thickness of the material, however this gives information about the difference δn. The absolute values of n_L and n_R remain undetermined. Al-

though the dispersion relations are theoretically modelled [91], these have never been measured directly. The polarization interferometer can be used to obtain these values.

To obtain the values of n_L and n_R at the operating wavelength of the HeNe laser, two identical CLC cells are positioned in the two arms of the interferometer, between the QWP1 and QWP2 (3.1), so that the two orthogonally polarized laser beams are propagated through each separately. One of the cells is used as the reference, and is kept at a constant temperature T_{ref} in the isotropic phase, where $n_L = n_R \equiv n_{ref} = 1.49804$.

The other CLC cell can be controlled in temperature using a Peltier plate system with a current driver, equipped with a PID controller with feedback control from a thermoresistor which gives control of the temperature within an error of $\delta T = \pm 0.05\ ^{\circ}C$. The phase of the CLC can be controlled by changing the temperature of the cell.

The interferometer is set to offset, by setting the temperature of the two cells equal. Any eventual spurious contribution from the glass substrates is therefore also nulled in this way, so that in this condition the measured phase difference will be $\Gamma = 0$. Using then Equation (3.23) we can assume that the two index of refractions $n_{L,R}(T)$, depending which state of circular polarization is set to be propagated on the temperature controlled "sample" CLC cell, can be obtained with this formula, after measuring the phase difference $\Gamma(T)$:

$$n_{L,R}(T) = \frac{\lambda}{2\pi d}\Gamma_{L,R}(T) + n_{ref}\ . \tag{3.28}$$

One of the main experimental difficulties have been refractive index fluctuations due to air convection that is created inside the closed sample area, by the temperature difference between the "sample" and the "reference" cell. A small ventilation system had to be designed to overcome the problem, by stabilizing the temperature and extracting the heat. As clearly shown in Figure 3.11, where the mass density is plotted against the temperature of the sample, the expected phase transition temperatures for the

cholesteryl oleyl carbonate [82, 83] are expected at $T_{I-Ch} \sim 36\ ^{\circ}C$ for the isotropic–cholesteric transition and at $T_{Ch-Sm} \sim 20\ ^{\circ}C$ for the cholesteric-smectic transition.

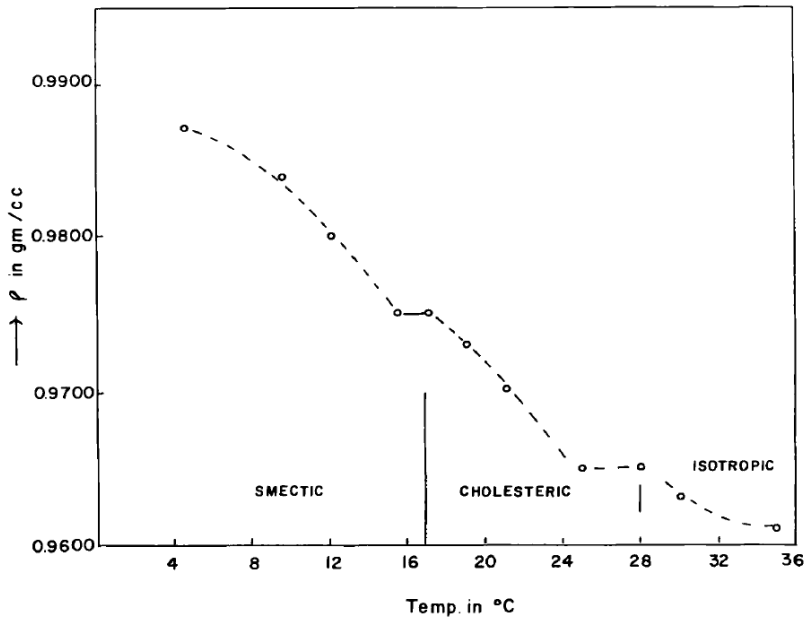

Figure 3.11: Mass densities for cholesteryl oleyl carbonate showing the phase changes depending on the temperature. Reprinted from [83].

3.2.1 Results

For the discussion of the results a reduced temperature scale is used, defined with respect to the isotropic-cholesteric temperature, which is defined as $(T_{I-Ch} - T)$. In function of the temperature of the sample we can measure the transmission of the laser ($\lambda_0 \simeq 633\ nm$) intensity to observe the behavior of the samples and gain information about the phase transition temperatures of the actual samples that are positioned in the interferometer. If all the optics of the interferometer except A are removed after the sample, is possible to measure the transmission depending on the incoming polarization state that can be selected on QWP2 (Figure 3.1).

In Figure 3.12 the results of these measurements are plotted (the insets i-iv show actual optical camera pictures acquired from a $\sim 5\ mm$ side at different temperatures around the phase transition temperature. From the

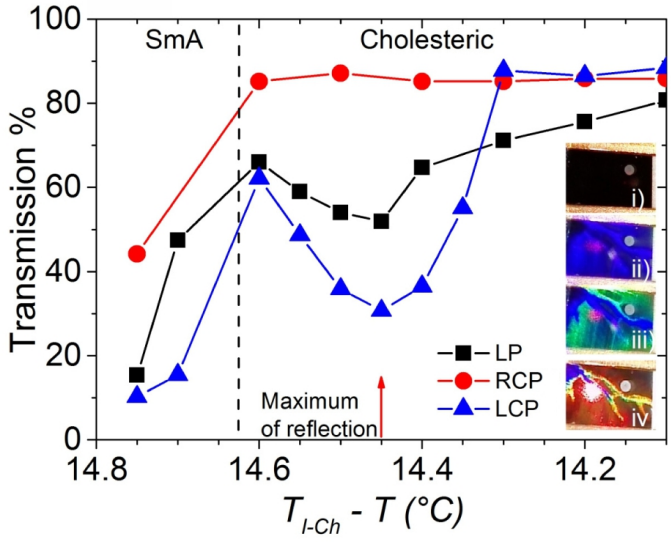

Figure 3.12: Temperature dependence of the phase retardation (Γ) measured at $\lambda \simeq 633\ nm$. Adapted and reprinted from [24].

sample's colour, under normal illumination with incandescent light). From the data we can recognize the cholesteric-smectic transition and the Bragg reflection domain, where only LCP of the two polarization components is reflected. A further general $\sim$ 12 % loss in intensity can be attributed to the glass interfaces of the cells containing the liquid crystal. In the smectic phase scattering strongly dampens any transmission [92].

The phase retardation as a function of the temperature, measured with the interferometer are shown in Figure 3.13, showing large changes in phase ($\Gamma(T_{I-Ch} - T)$) for impinging LCP (set with QWP1). Almost no influence is seen for the same measurements when RCP light is selected. For a change in temperature of about $\sim$ 0.05 $^{\circ}C$ from 14.45 $^{\circ}C$ to 14.50 $^{\circ}C$, the measurements show the presence of an inversion point for LCP, as expected qualitatively at ω_B (Figure 3.10b). This abrupt change might be connected with the reorientation of the major axis of nearly circular polarized modes in the CLC. This is expected [84, 93] and probed qualitatively also in the interferometry experiments [24].

From the measurements of Γ it is then straightforward to calculate the corresponding index of refractions $n_{L,R}$ that were sought, using the equation

in (3.28). The results are plotted in Figure 3.14. While the value of $n_R \approx n_{ref}$ for any temperature in the cholesteric phase, n_L changes at the Bragg resonance of about $\delta n_L \simeq (1.5005 - 1.4955) = 5.0 \cdot 10^{-3}$.

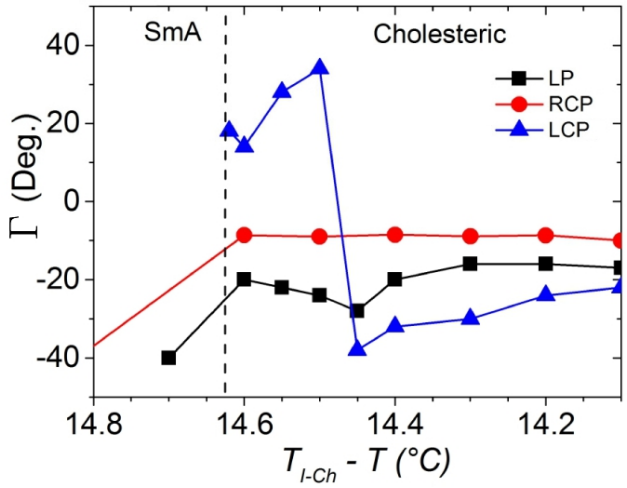

Figure 3.13: Temperature dependence measurements of the transmission of polarized light with $\lambda \simeq 633\ nm$. Adapted and reprinted from [24].

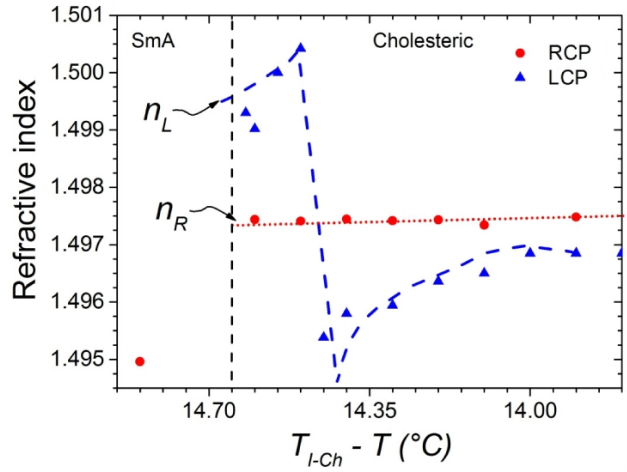

Figure 3.14: Temperature dependence of the index of refraction for left (n_L) and right (n_R) handed circular polarization at $\lambda \simeq 633\ nm$. Interrupted lines are two guide the eye. Adapted and reprinted from [24].

As an additional control, the measurements of optical rotation (OR) of a linearly polarized laser light have been carried and are to be compared with the interferometer related data of n_L and n_R, simply using the relation found in the equation in (3.27) and assuming the thickness of the sample of

25 μm $\rho(T)$ the two measurements compare consistently as is shown in the plot in Figure 3.15.

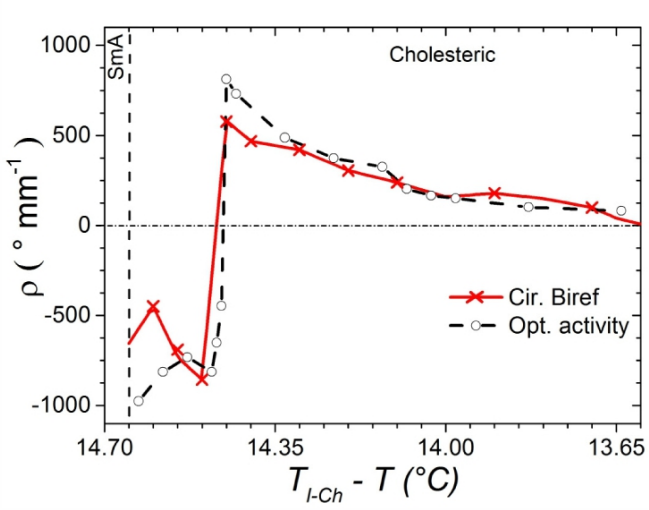

Figure 3.15: Temperature dependence of the ORP (ρ) as measured from measurements of optical rotation of linearly polarized laser light compared to the values calculated from the measurements of the circular polarization index of refractions n_L and n_R obtained with the polarization interferometer. Reprinted from [24].

Chapter 4

Chiral negative index metamaterial

Half a century ago (1967) V. Veselago theoretically analysed the possibility to have materials that would have both an electric permeability (ϵ_r) and a magnetic permeability (μ_r) that is negative [94], which means the medium has a negative real component of index of refraction(n'). Up to this point, materials were only believed to posses a positive index of refraction. The experimental observation of a metamaterial with $n' < 0$ was first obtained more than three decades later (2001) by Shelby et al. [95].

In 2004 Pendry showed [22] that a negative index of refraction can also be obtained in a chiral medium without a magnetic response. Many experiments have since explored chiral negative index metamaterials (ChNIM). Wang et al. show how an array of split ring resonators, conveniently wired and aligned to obtain coupled layers of 2D metamaterials, can be arranged on 3D chiral unit cells [96]. Another approach is to use metal structures where now the chirality is inherently present in the shape, such as a helix. The fabrication is more complicated. Gansel et al. did not explore a negative index both numerically [66] and experimentally [64] examined a chiral metamaterial of gold helix arrays that can be used as a circular polariser in the IR.

In Chapter 2 has been shown that a chiral metamaterial deposited with the GLAD system using a plasmonic metal, shows a large optical activity that is also tunable by accurately designing the geometrical parameters of

the helical unit structure. In particular the structures are small enough, that the optical activity can be tuned from the IR to the UV. The samples can be produced in a fast manner on very large substrates. In Chapter 3 it was shown how a laser interferometer can be used to measure the phase that a circularly polarized light component acquires when it propagates along a uniaxial optically active material. Here we present the measurement of the index of refraction of chiral metamaterials, deposited on a transparent substrate as a thin film of sculptured 3D helix arrays.

4.1 Index of refraction of an optically active material

The easiest way to probe the presence of circular optical activity is by measuring a CD spectrum. By the Kramers-Kronig relations it follows that such a sample must also show a circular birefringence. During a GLAD deposition the same glass substrates used for the copper helices shown in Chapter 2 can be used. Instead, if other metals with stronger plasmonic resonances are used, the strength of the optical activity is expected to be enhanced.

If we assume a medium with optical activity, then for an isotropic medium or a uniaxial medium that is observed along the optical axis:

$$\tilde{n}_{L,R} = \tilde{n}_0 \pm \frac{\delta\tilde{n}}{2}\,, \tag{4.1}$$

where

$$\tilde{n}_0 = \frac{\tilde{n}_L + \tilde{n}_R}{2}\,. \tag{4.2}$$

The $\Im[\delta\tilde{n}]$ can be determined measuring the CD, while the $\Re[\delta\tilde{n}]$ can be obtained from a measurement of the CB, which is canonically obtained with a measurement of the angle of rotation of the polarization axis of a linearly polarized light beam transmitted through the material, which is a measurement of the optical rotation (OR). As clearly described in Ref. [97]

for the specific case of a cholesteric liquid crystal, the CD and OR spectra are connected by the Kramers-Kronig relations.

In Chapter 3, it has already been discussed how n_L and n_R can be measured using the laser polarization interferometer, which works at a wavelength of $\lambda_0 \approx 633\ nm$.

Let's assume now that a material has $\|\frac{\delta\tilde{n}}{2}\| > \tilde{n}_0$. It follows that one of the two indices for circular polarized light should become negative. In particular, the real part of the index of refraction $\Re[\tilde{n}] = n'$ will, following Pendry's prediction, become negative in such a chiral metamaterial.

4.2 Fabrication of a chiral plasmonic metamaterial with subwavelength thickness

First a suitable material (metal) has to selected. Silver and gold are the best candidates as they show a strong free electron density and consequently strong plasmonic resonance. Bulk optical properties suggest that at $\lambda_0 = 633\ nm$ the $n'_{Ag} \approx 0.051$ and $n'_{Au} \approx 0.143$ [98], so the n'_0 can be expected to be low. Although gold is easy to deposit in the GLAD system to obtain good quality nanohelix structures, previous attempts for the growth of nanohelices with silver did not give good results. This is probably because of the higher diffusivity of silver atoms, which does not result in defined structures when used in the evaporation system of the GLAD chamber. To reduce the adatom surface diffusion during the condensation process of the physical vapour incident on the target substrate, a small amount of titanium has been co-evaporated. The volume ratio estimated from the quartz crystal monitors positioned inside the evaporation chamber is about $4 - 5\%$. Co-evaporating this small amount of titanium has a dramatic effect on the quality of the resulting structures [99].

The fabrication of nanohelix arrays with both gold and silver is also possible. The results from numerical simulations and measurements of CD and CB on a large number of samples suggests that silver nanohelices tuned to

have a maximum of OR at the working wavelength of the laser interferometer have a larger CB and a lower bulk refractive index $\Re[\tilde{n}]$ at the plasmon resonance.

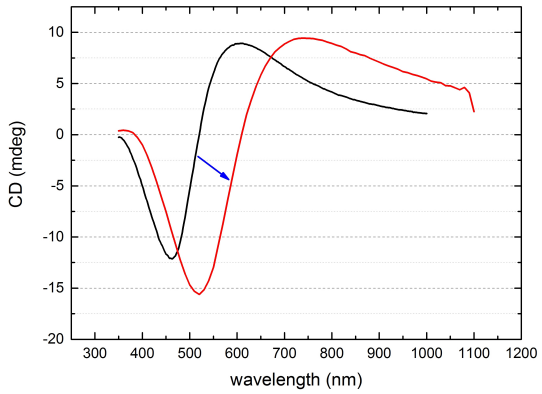

(a)

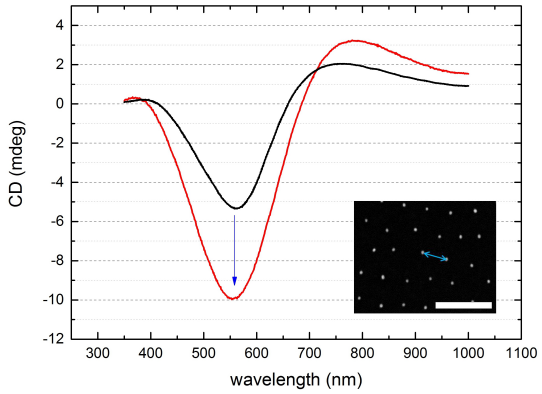

(b)

Figure 4.1: CD spectra measurements showing the effect of the change of the pitch (P) and the spacing of the helices (φ), obtained with different preparation of the seeded glass substrates during the BCML procedure. (a) Film of total height of 100 nm with $P = 50$ nm (black) and $P = 75$ nm (red). (b) Single turn helices with $P = 150$ nm, with different spacings (φ). The inset is a top-view SEM micrograph of the BCML hexagonally patterned substrates where the double arrow marks φ; scale bar is 100 nm.

CD spectra can give useful information about the optical activity present in the material and are fast to acquire (with the JASCO 810 spectropolarimeter). In Figure 4.1a are shown the CD spectra for two different sam-

ples obtained depositing silver helices of $h = 100$ nm total height, with respective pitch lengths (P) from $P = 50\ nm$ (black) and $P = 75\ nm$ (red). Increasing P results in a red-shift of the negative CD peak from $\lambda = 460$ nm to $\lambda = 520$ nm. Another parameter which results in an enhancement of the optical activity is given by the packing density of the deposited helical structures. Reducing the distance of the nanodot seeds during the BCML process shows that the corresponding CD spectra (see Figure 4.1b) increase in strength. The same deposition of a 1 turn helix with $P = 150$ nm, with two substrates with different spacing (φ) between the seeds doubles the CD response when the distances are reduced from $\varphi = 80$ nm (black) to $\varphi = 25$ nm (red).

OR measurements of the samples deposited in the GLAD system on glass, have been obtained using the Jasco spectropolarimeter. The light from the lamp source and a monochromator is linearly polarized using a Fresnel stack. The spectral resolution is adjusted from 0.01 nm to 15 nm to permit enough light to reach the detector. After the light is transmitted through the sample a second polarizer was rotated to find the intensity minimum on a photomultiplier tube (PMT). The intensity of the transmitted light is correlated with the orientation of the second polarizer. This gives a measurement of the angle of rotation of the polarization and therefore of the OR of the sample which is positioned between the two polarisers.

Figure 4.2 shows the results of OR measurements of 2 turn silver nanohelices with $P = 150$ nm, deposited on glass substrates patterned with gold seeds of about a diameter ~ 7 nm and a spacing of $\varphi \sim 25$ nm.

The OR can also be measured with the same configuration of crossed polarisers, using a laser source instead of the lamp and monochromator. Compared to the beam from the lamp of ~ 1 cm^2 the laser results in a probe beam of < 1 mm^2. This is interesting because it gives the possibility to measure the whole surface of the deposited samples with a much higher spatial resolution. The same sample measured previously (Figure 4.2) shows local variations in the measurements of OR with a variation depending

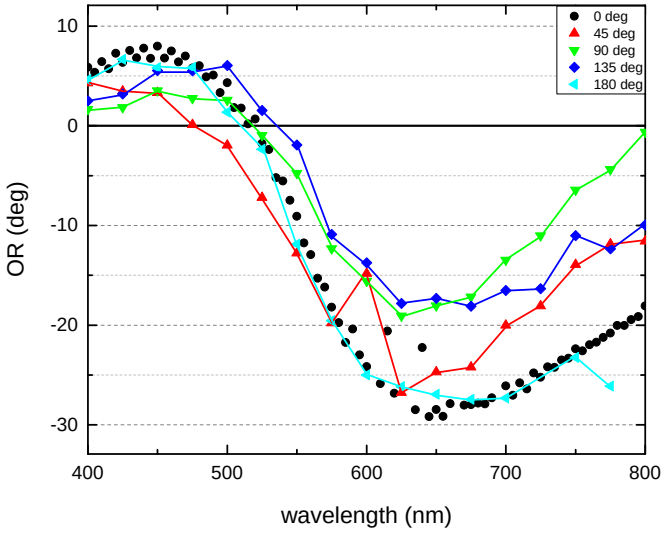

Figure 4.2: Optical rotation measurements of visible linearly polarized light through a thin film of silver nanohelices with total height of 300 nm and pitch length 150 nm. The helices are deposited on a glass substrate patterned with BCML procedure with gold nanodots of 7 nm diameter, hexagonally arranged with separations of 25 nm. The different colors in the plot are for different measurements performed rotating the sample in the direction parallel to the direction of propagation of the probing light, with respect to the direction of the polarization. Refer to the legend of the plot for the angle of rotation for each set of measurement.

on the position of the sample of roughly 50%. The variation of the OR depends on the area probed by the laser beam (TEM_{00}, with a waist of about ~ 0.7 mm). This suggests that the whole metamaterial formed by a nanostructured coating on the glass substrate was not of a high quality. The reason for this lack of uniformity is, however, not due to any inhomogeneity of the fabrication process but rather the quality of the substrate, which shows a residual birefringence and also a variation in thickness. The latter is problematic of any interferometric measurements. The inhomogeneity results from the roughness of the substrate's surface as the shadowing of the physical vapour at grazing angles of the GLAD technique is sensitive to the small deviations from an ideal flat surface; second, for optical probes

also the small variations of the surface or the strain in the glass substrate may show strong polarization effects.

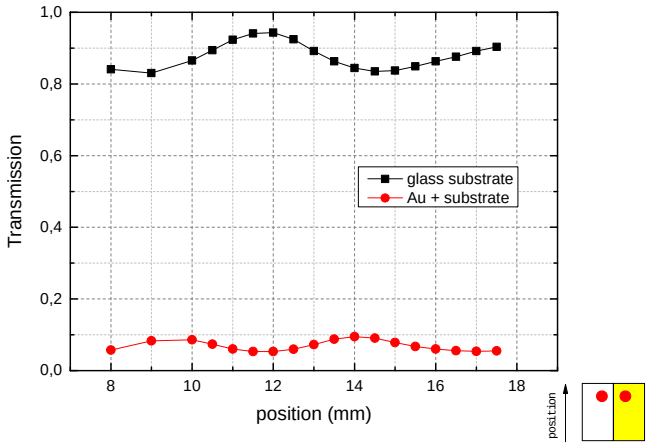

Figure 4.3: Transmission of $\lambda_0 \approx 633\ nm$ laser beams on a glass substrate half sputtered with 40 nm gold film. The inset at the bottom-right of the plot shows a scheme of the sample, the probing beams of the interferometer and the direction along which the sample is moved during different measurements.

Although relatively easy to handle and inexpensive, the glass substrates are not appropriate for the sensitive measurements that are to be carried out in the laser interferometer for the determination of the index of refraction of the metamaterials, as the following simple experiment demonstrates: the transmission of normal incident linearly polarized laser light at $\lambda_0 \approx 633\ nm$ has been measured through one of the glass substrates. The substrate was sputtered on one half with a gold film of thickness 40 nm and the other half of the surface of the glass substrate was left clean (sample prepared by Reinhard Völker). The surface has been also analysed after sputtering by Christian Kappel in ZYGO New View 5000 white light interferometer, to probe the flatness of the surface. The result of C. Kappel shows that the roughness on the side of the sputtered gold was lower than the resolution offered by the white light interferometer, which means < 1 nm. Figure 4.3 shows the measurements carried independently of the relative intensity of the two beams being transmitted through the clean and gold sputtered half

of the sample in the interferometer. For this measurement the QWPs were removed and linearly polarized light is normally incident on the surface. The sample was then moved to a new position and re-measured. The interference of the two beams has been measured as well, following the method described in Chapter 3. The index of refraction of the gold film (assuming a thickness of 40 nm) has been calculated as a function of the position of the probing laser beams on the sample (Figure 4.4). The variations in these results, prove that the BK7 glass substrates are not suitable for sensitive refractive index measurements, as the effect of thickness variation of the glass is larger than the expected difference due to the circular birefringence. Substrates of defined thickness are needed.

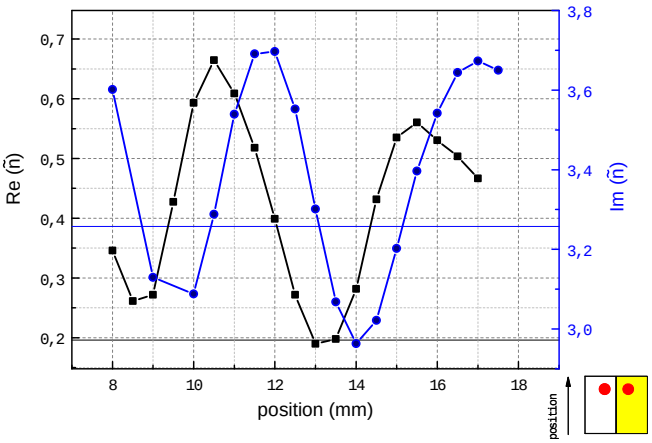

Figure 4.4: Index of refraction at $\lambda_0 \approx 633\ nm$ of gold as calculated from the measurements with the laser interferometer on a glass substrate, half sputtered with 40 nm gold film, see text for details about the measurements. The straight horizontal lines mark the values of the index of refraction of gold according to Ref. [39]. The inset at the bottom-right of the plot shows a scheme of the sample, the probing beams of the interferometer and the direction along which the sample is moved during different measurements.

For the aforementioned reasons silicon nitride membranes were chosen as substrates for interferometric measurements. The substrates are commercially available from Silson Ltd (Blisworth, Northampton, NN7 3DW, England) were therefore adopted. C. Miksch prepared all the windows with

BCML patterning for the samples to be deposited with the GLAD system. Different thicknesses of the suspended film were tested and the minimum safe thickness that has the mechanical strength to "survive" the BCML and GLAD process has been identified to be 150 nm. The dichroism and birefringence of these films have been measured after the BCML processing to identify inhomogeneity or any optical anisotropy (strain), but such effects could be detected within the sensitivity of the optical analysis instrumentation. At the same time, the BCML process had been refined and for these new substrates of suspended SiN films, it was possible to obtain BCML patterned gold dots of diameter 3 nm with a mean separation on the hexagonal pattern of $\varphi = 20$ nm. Figure 4.5 shows a SEM image of one of these patterned SiN windows. For visual clarity the smallest dots and spacings are not shown here.

GLAD was performed on the SiN substrates (like the ones shown in Figure 4.5). The result is a thin film of a metamaterial structured as a closely packed array of silver nanohelices with interstitial separations that are below 10 nm.

As shown in Figure 4.6 the chiral metamaterial film, deposited with the GLAD system is a silver - titanium alloy (96% : 4%), that results in a highly packed array of nanohelices. Using such a dense film with Ag reduces the amount of air between the helices and thus will cause the effective n_0' to be as small as possible near the plasmon frequency. The subsequent measurements are based on films similar to the one shown in Figure 4.6 and show that the CB are large enough to generate negative indices of refraction.

4.3 Interferometric measurements.

The optical activity present in plasmonic helical nanostructures can be large. In the previous section it was shown how a thin film deposited with the GLAD technique, could be tuned to $\lambda_0 \approx 633$ nm, which is the wavelength of the laser polarization interferometer.

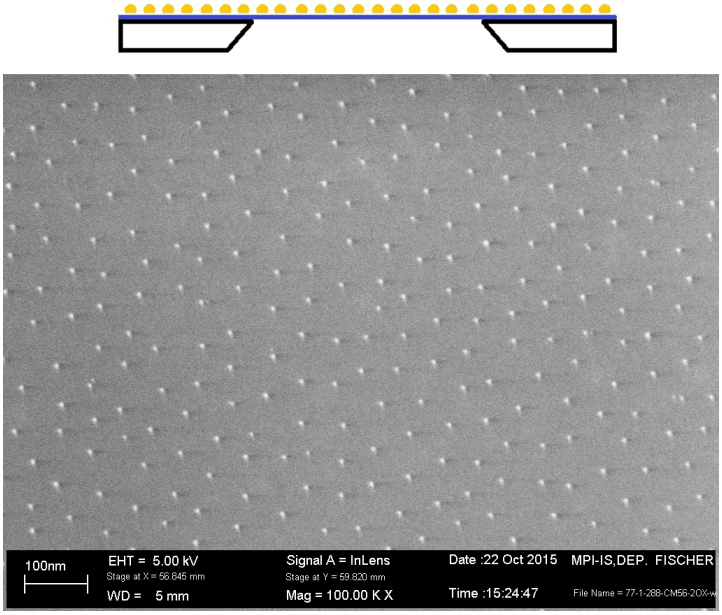

Figure 4.5: Top view SEM image of a suspended silicon nitride film of 150 nm, patterned with gold dots arranged on a hexagonal pattern using BCML. The mean distance of the gold dots is $\varphi = 68\ nm$, while the diameter of each dot is 7 nm. Image credit C. Miksch. Above the image is a schematic representation of a lateral central section of the suspended film. Yellow is gold, blue is silicon nitride and black is the silicon frame.

The use of the SiN windows which possess only small openings and the strong absorption present in the silver films make it necessary to focus the light for any transmission measurements. This makes standard spectropolarimeter for OR rotation and CD measurements not useful as typically the optical aperture at the center of the SiN suspended films is a square of edge (l) between 1.0 $mm \leq l \leq 3.0\ mm$. However, single wavelength measurements with a laser are still possible in the polarization interferometer. The whole thickness variation of the suspended 150 nm SiN films is specified as 10 % by Silson Ltd.

Assuming uniaxial symmetry, a maximum optical rotatory power (defined as ρ =OR/d, which can be measured in units of $deg \cdot\ \mu m^{-1}$ and where d is the thickness of the metamaterial), a maximum of $\rho \approx 380° \cdot \mu m^{-1}$ have been measured on these samples. To compare with other optical metamaterials, which are reportedly the materials with the highest rota-

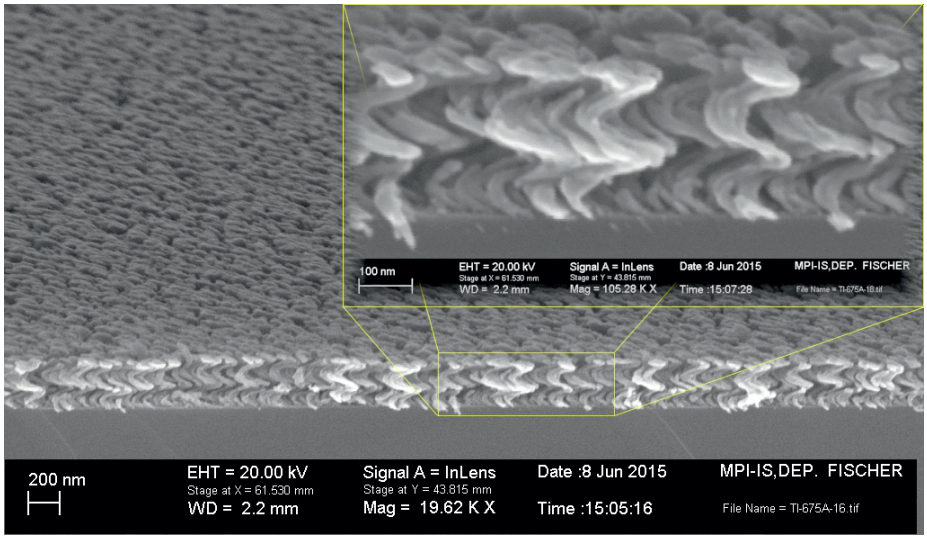

Figure 4.6: Side view SEM image (5° tilted) of a chiral metamaterial film, deposited with GLAD system as a silver - titanium alloy (96:4), which is nanostructured as an array of standing 2 turn nanohelices of 300 nm total height. The patterned substrate, obtained with BCML, is with gold nanodots of 3 nm diameter, arranged on a hexagonal pattern with 15 nm mean distances.

tory powers that might exist, Decker et al. have realized in coupled bilayers of twisted-crosses of gold $\rho \approx 46° \cdot \mu m^{-1}$ [100] or again by using instead twisted split-ring resonators a $\rho \approx 146° \cdot \mu m^{-1}$ [101]; with another technique Gorkunov et al. have instead milled silver films holes of start-screws through which they reported $\rho \approx 330° \cdot \mu m^{-1}$ [102]. This indicates that in presence of such an enormous optical activity in a medium of 300 nm thickness a $\delta n' = n'_L - n'_R \approx 1.3$ should be expected.

The absolute values of n'_L and n'_R can be measured using the laser interferometer. The metamaterial shown in Figure 4.6, deposited on a 5 mm × 5 mm SiN windows with a central aperture of 2.0 mm × 2.0 mm was positioned after the QWP1 in one arm of the interferometer. A clean SiN, with the same thickness (150 nm) was positioned in the second arm and used to compensate the phase difference given by propagation through the substrate. Rotating QWP1 can switch the polarization between LCP and RCP. Results from the corresponding interferometric measurements are shown in

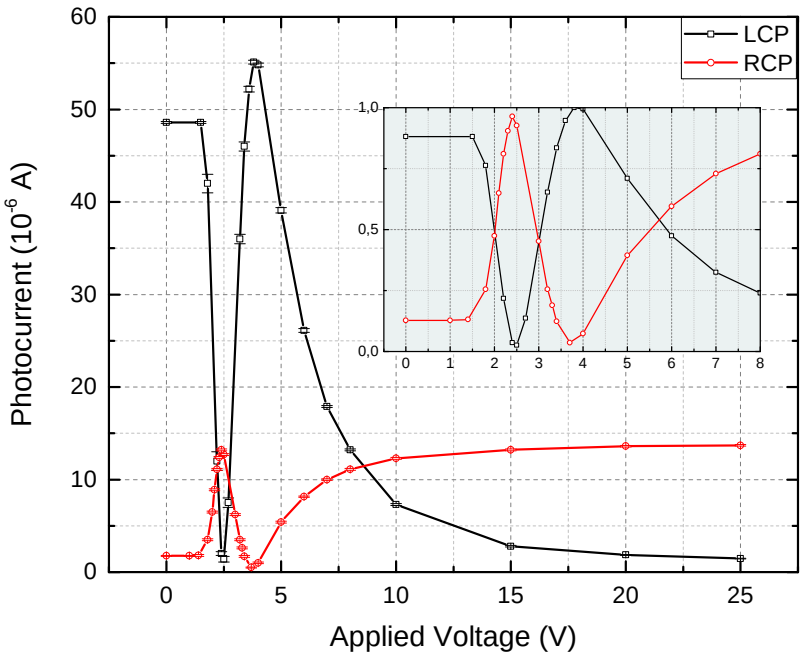

Figure 4.7: Measurements carried out with the circular polarization laser interferometer ($\lambda_0 \approx 633\ nm$) as a function of the voltage set on the driver of the LCC-1113A. Inset: detail for the lower values of the applied voltage, with the normalized values of the measured interference of the two beams of the interferometer.

4.7. The applied Voltage on the LCC-1113A, drives the liquid crystal polarization compensator (compare to Figure 3.5). The values of accumulated phase Γ for each one of the states of polarization LCP and RCP, can then be calculated using the calibration of the LCC (see Section 3.1.5). Finally, after retrieving values of the phase retardation (advancement) measured for LCP or RCP being transmitted through sample, the following indices of refraction are obtained with the help of equation (3.23):

$$n'_L = +1.1 \tag{4.3}$$

$$n'_R = -0.2 \tag{4.4}$$

Under the assumption of uniaxiality, these results suggest that the chiral samples can give rise to a negative index of refraction at visible wavelengths.

The index of refraction can be positive or negative, depending on the polarization of light. The relevance to observe such a kind of behaviour inside a material is schematically shown in Figure 4.8, where the evolution of the electromagnetic wave is computed at a specific time, differentiating at the first interface with two colours the two cases corresponding to the values of $n' = \{-0.2,\ +1.1\}$.

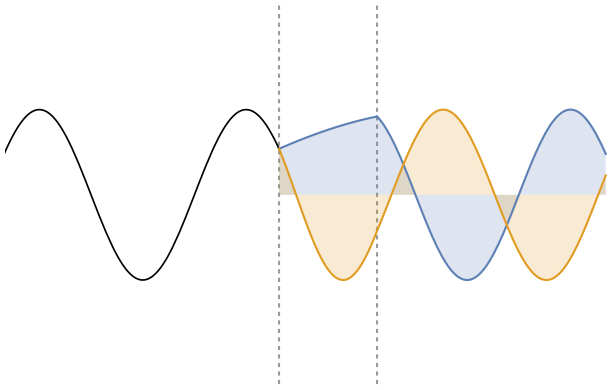

Figure 4.8: Conceptual representation of the transmission of a wave in a slab of material. The incoming wave (black) is represented propagating from left to right. In particular here are represented two cases of a wave experiencing the real part of the index of refraction $n' = +1.1$ (red) or $n' = -0.2$ (blue) during the propagation in the material, delimited by the vertical dashed lines. Losses are neglected on purpose.

However, as can be observed from the measurements of OR plotted in Figure 4.2, the films are not perfectly uniaxial therefore $\tilde{n}_R$ and $\tilde{n}_L$ are then not, in principle, uniquely defined. In what follows the assumption of uniaxiality will be examined and discussed in more detail.

4.4 Symmetry considerations.

Evidence of an anisotropy of the optical activity is present in the analysis of the arrays of nanohelices. Exhaustive sets of measurements both of the CD and OR show that the metamaterial films are not uniaxial. Consider the plot in Figure 4.2, which shows the results of OR measurements in transmission through 2-turn silver helices of total height 300 nm deposited

on a glass substrate, with BCML patterning of gold dots with 25 nm mean spacing distance and 7 nm diameter.Indicated in the figure is the angle by which the sample is rotated while the direction of the incident polarization is kept fixed. A similar orientation dependence is found with 1-turn helices of a total height now of 150 nm (Figure 4.9).

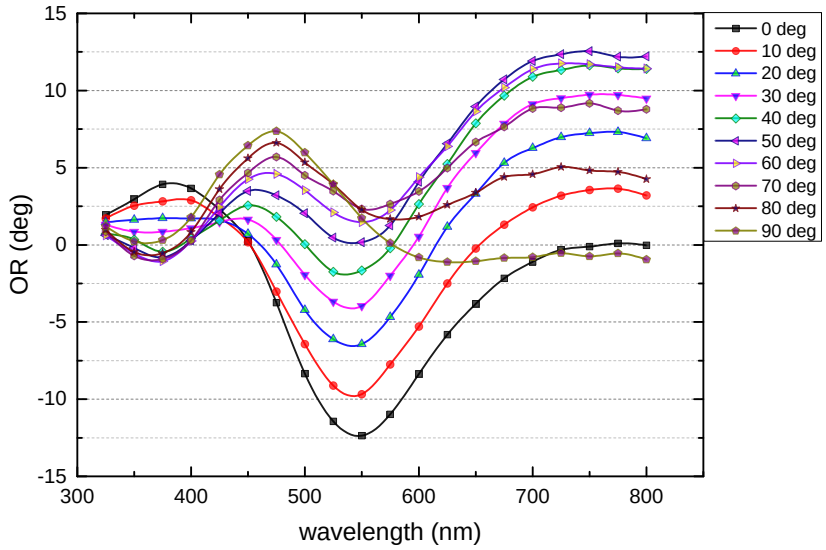

Figure 4.9: Optical rotation measurements of linearly polarized light through a thin film of silver nanohelices with total height of 150 nm and pitch length 150 nm. The helices are deposited on a glass substrate patterned with BCML procedure with gold nanodots of 7 nm diameter, arranged on hexagonal patterns with separations of 25 nm. Different colors are used for different measurements performed rotating the sample with respect to the direction of polarization. Refer to the legend of the plot for the angle of rotation for each set of measurements.

Unfortunately, the absence of a specific model for the propagation of light in a nanostructured non-uniaxial (possibly triclinic) material does not help in interpreting this behaviour. However, it is possible to make some general observations by analysing the dependence of the optical activity on the azimuthal angle of these metamaterials. First, it is evident that a combination of circular optical activity and a linear optical activity is present in the film, and they can result in effects which are comparable in magnitude.

The 90° periodic dependence, which is evident from the OR spectra is a clear indication of this. Further, the spectral dependence of OR, that appears more clearly in Figure 4.9, suggests also that this combination of linear and circular optical activities, might be directly connected with the different modes of collective electronic resonances that can be sustained on these silver nanostructures. and which have been thoroughly simulated numerically with DDSCAT and visualized in case of an isolated freely suspended silver helix by Zhang [65, 103].

In order to determine all circular and linear birefringences and dichroisms that may be present, the samples have been sent to the Kahr Group at New York University, who operate a Stokes polarimeter [104]. This permits the independent retrieval of the rank 4 Müller matrix, therefore the determination of the different components of optical activity (i.e. CD, CB, LD, LB). Figures 4.10 and 4.11 show the results of the measurements, which were carried by the Kahr group at New York University using the 4-PEM polarimeter, on three samples obtained during the same GLAD deposition, together with other three samples that were measured with the polarization interferometer at the MPI-IS in Stuttgart. Within the sensitivity of the interferometer, no variations could be observed between the three different samples. Comparisons can be made between the measurements using the interferometer and the Stokes polarimeter.

Unfortunately, the Stokes polarimetric measurements indicate that the nanohelix films have triclinic symmetry. The films can therefore not be described by a unique refractive index $\tilde{n}_{L,R}$ for LCP and RCP. The directions of the LB and LD are independent and do not share a common axis as can be seen in Figure 4.10c where the difference angle (delta) is plotted. However, the amplitude of LD and LB, as is observed from the Figures 4.10a and 4.10b are strongly reduced at the working wavelength of the interferometer. Correspondingly this is the wavelength for which the samples were programmed to present a maximal CB (Figure 4.11b). From the same measurements of CB, using the definition of ORP in the equation in 3.27, it

is possible to estimate that $-0.8 \geq \delta n' \geq -1.3$, which compares well with the $\delta n' = n'_L - n'_R = -1.3$ that is measured in the interferometer under the assumption of uniaxiality.

4.5 Final discussion.

In conclusion, evidence has been found of a chiral metamaterial realized as a nanostructured subwavelength thin film coated on flat surfaces and obtained with glancing angle deposition, where the real component of the index of refraction can be negative. The origin of this is a strong circular birefringence which at the plasmon resonance frequency is greater than the real part of the mean refractive index n'_0. The shape and material composition was optimized to yield maximal circular birefringence at $\lambda_0 \simeq 633\ nm$.

Independent polarimetry measurements reveal also that the system is not perfectly uniaxial, but triclinic. However, the linear optical activity is more than an order of magnitude weaker than what results for the circular optical activity. The metamaterial considered may therefore be approximated as a quasi-uniaxial sample.

The different steps taken towards maximizing the circular optical activity and minimizing the linear optical activity described in this chapter, revealed a sensitivity to the structure of the nanohelices and their spacing. The unusual damping of the linear optical activities may most probably be explained by analysing the near field interaction arising from the plasmonic resonance of the nanohelices and identifying planar symmetries arising from the mode of the resonance that can be sustained inside the metamaterial. The spacing of the helices seems also to have an important role in this. Further steps in the fabrication process might then be able to reduce even further LD and LB and help to grow perfectly uniaxial chiral negative index films.

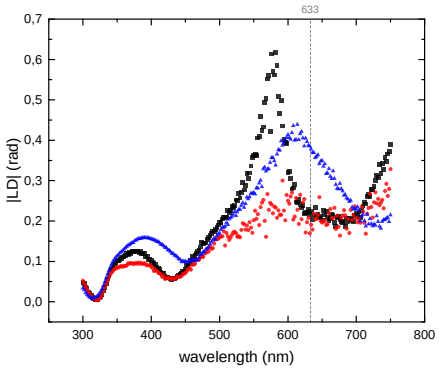

(a) Linear dichroism (LD).

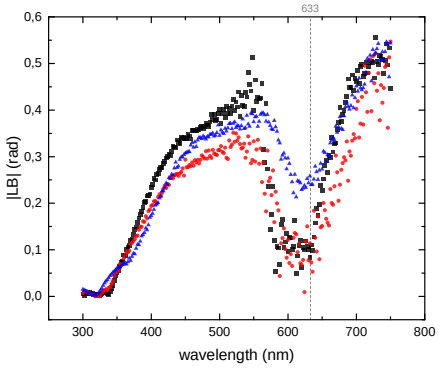

(b) Linear birefringence (LB).

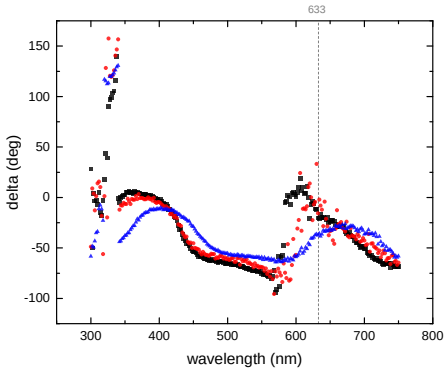

(c) Difference (delta) between the direction of linear dichroism and linear birefringence.

Figure 4.10: Results for the linear optical activity from the polarimetry measurements carried out by the Kahr group at New York University. Three samples (marked with different colours and markers) that were deposited together with the samples shown in Figure 4.7).

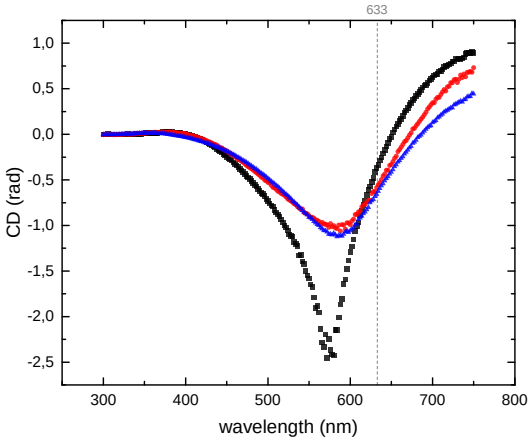

(a) Circular dichroism (CD).

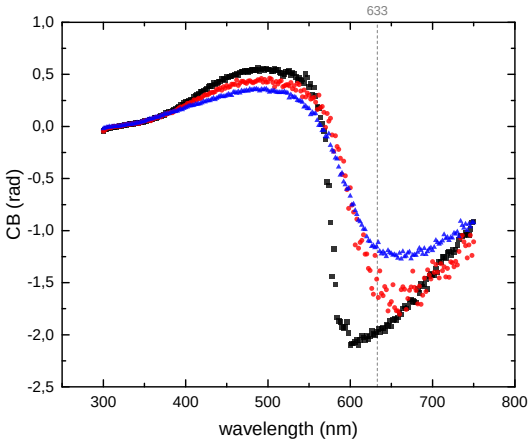

(b) Circular birefringence (CB).

Figure 4.11: Results for the circular optical activity from the polarimetry measurements carried by the Kahr group at New York University on three samples (marked with different colours and shapes) that were deposited together with the samples with $n'_L = +1.1$ and $n'_R = -0.2$ (referred to the measurements shown in Figure 4.7).

Chapter 5

A ferromagnetic-plasmonic-chiral metamaterial

Parts of this chapter have appeared in the publication
ACS Photonics 1(11), pp1231-1236 (2014) [25]

In this chapter a metamaterial analogous to the previous GLAD deposited nanohelix arrays is considered, which can also have additional optical properties if the nanohelices are also ferromagnetic. The elements which are found in a ferromagnetic phase at ambient condition are iron, nickel, cobalt and few rare earth elements. The spontaneous magnetic ordering is due to an ordered arrangement of the single magnetic moments present inside the material, where an internal interaction called the exchange interaction favours all the magnetic moments to line up. This is opposed by the thermal agitation, which at higher temperatures overwhelms the exchange interaction. The critical transition temperature between an ordered (ferromagnetic) and a disordered phase of the magnetization is the Curie temperature (T_c).

As the critical dimensions of a magnet approaches the ferromagnetic domain size, structural morphology becomes increasingly important in relation to its magnetic properties, in fact magnetic domain formation may be influenced [105]. For ferromagnetic nanoparticles, or nanomagnets, the magnetic domain size and the electron transport scattering length can both

be of the same length scale as the size of the particles themselves. Such nanoscale magnetic materials are interesting due to possible applications as high-density data storage media or for the study of more fundamental properties such as magnetic vortex formation [106, 107]. Nanoscale materials are particularly compelling because multiple properties can arise from the same morphological confinement.

The samples that will be considered in detail here are deposited with nickel (Ni), which is ferromagnetic at standard condition. Ni nanoparticles can also support surface plasmon resonances [107–109], therefore a geometric constraint in nanoscale Ni, not only limits the formation of multiple ferromagnetic domains but can also lead to localized plasmon resonance. Since the properties of a nanomagnet are highly geometry dependent, structural asymmetries can be expected to induce corresponding asymmetries even in its magnetic properties.

On the side of GLAD deposition was also found that, in the case of Ni and Co, the deposition process is particularly facilitated. This is because it is found to be working at best with the substrate at room temperature, therefore no liquid nitrogen cooling is required for nanohelix fabrication. Experiments that reveal the direct coupling of magnetic and optical properties of chiral Ni nanomagnets are shown and discussed in this chapter. Strong optical activity to visible light is detected and its dependence to an external magnetic field is measured. In particular, the coupling of the nanoparticle's chirality to the field and the simultaneous absence of parity and time reversal symmetry, leads to a higher order optical response known as magnetochiral dichroism (MChD) [110], which manifests itself as a tunable, polarization-independent absorption effect.

5.1 Magneto-chiral asymmetry

When a nanostructured material has a chiral asymmetry, it will interact differently with the two CP states of light, which are themselves chiral

[60, 63, 111–115]. As geometrical shape is called chiral when it cannot be superimposed in its mirror image with any possible reorientation, this also means that chirality is sensitive to a parity transformation along a symmetry axis (P). To describe the various contributions to the optical activity in absorption, we need to refer to the general multipolar expansion of the radiation-matter interaction [7].

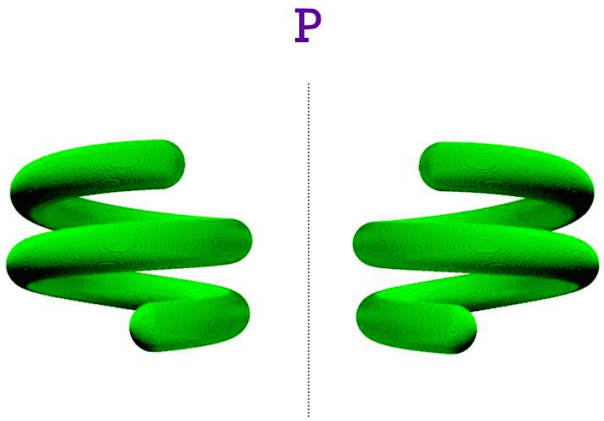

Figure 5.1: The effect of a parity transformation (P) does not conserve the chirality. As shown in this graphics the transformed shape has inverted handedness.

In the multipolar interaction approximation, a chiral distribution of charges could be sensitive only to those interactions that have an asymmetry with respect to the P transformation. An electric dipole ($\vec{\delta}$) is odd under a P transformation while a magnetic dipole ($\vec{\mu}$) is even under a parity transformation. For simplicity, the interaction Hamiltonian ($\mathscr{H}^{int}$) can be written as

$$\mathscr{H}^{int} \approx -\vec{\delta} \cdot \vec{E} - \vec{\mu} \cdot \vec{B} \tag{5.1}$$

This model is useful to motivate the presence of different contributions to the optical activity. Chiral media exhibit natural circular dichroism (NCD), which is the CD without the presence of external fields. Similarly, any medium in the presence of a magnetic field (parallel to the direction of light propagation) will also show differential absorption proportional to the field strength, i.e., magnetic circular dichroism (MCD). The former is mediated

by the imaginary component of the product of an electric-dipolar–magnetic-dipolar ($\vec{\delta}\cdot\vec{\mu}$) transition moment, whereas the latter is a function of a product of two electric-dipolar and one magnetic-dipolar transition moments ($\vec{\delta}\cdot\vec{\delta}\cdot\vec{\mu}$). It is interesting to point out that whereas NCD is dependent upon the chirality of the medium, MCD is not. These effects can be summarized by expanding the generalized dielectric function ϵ depending on the wavevector $\vec{k}$ and the magnetic field $\vec{B}$ [116],

$$\epsilon_{\pm}^{\mathscr{L}/\mathscr{R}}(\omega,\vec{k},\vec{B}) = \epsilon(\omega) \ \pm\alpha^{\mathscr{L}/\mathscr{R}}(\omega)k \ \pm\beta(\omega)B \ +\gamma^{\mathscr{L}/\mathscr{R}}(\omega)\vec{k}\cdot\vec{B} \ +\ldots \quad (5.2)$$

where $+,-$ correspond to LCP and RCP, respectively, while $\mathscr{L}$ and $\mathscr{R}$ denote the chirality of the medium. The first term in the multipolar interaction picture originates from an electric-electric-dipolar interaction ($\vec{\delta}\cdot\vec{\delta}$). The term with α is responsible for the natural optical activity (natural circular birefringence (NCB) and NCD) and is due to the magnetic-dipole electric-dipole interaction ($\vec{\mu}\cdot\vec{\delta}$). In the same picture, β is the electric-electric-magnetic dipole tensor ($\vec{\delta}\cdot\vec{\delta}\cdot\vec{\mu}$) that underlies the Faraday effect and MCD. The term with γ, characterizes the additional effect of a magnetic field in the presence of a chiral medium, and it depends on the chiral sense and the relative orientation between $\vec{k}$ and $\vec{B}$, but not on the polarization of light. In the multipolar approximation this last term originates from a magnetic-magnetic-electric dipole tensor ($\vec{\mu}\cdot\vec{\mu}\cdot\vec{\delta}$). It manifests itself in absorption as magnetochiral dichroism (MChD) which is a cross-effect of NCD and MCD, it has already been observed previously in chiral crystals and molecules [110, 117–119], but never in a nanostructured material. If we consider the dipolar operators and the combination of their symmetry under P transformations then, the tensors α and γ are non-zero only if the medium is chiral and it changes sign with the handedness of the enantiomorph. Because MChD is a cross-term, it is expected to be strong in systems that show substantial NCD and MCD [120]. In ferromagnetic-plasmonic nanohelices both NCD and MCD should be enhanced, thus giving

large values for MChD.

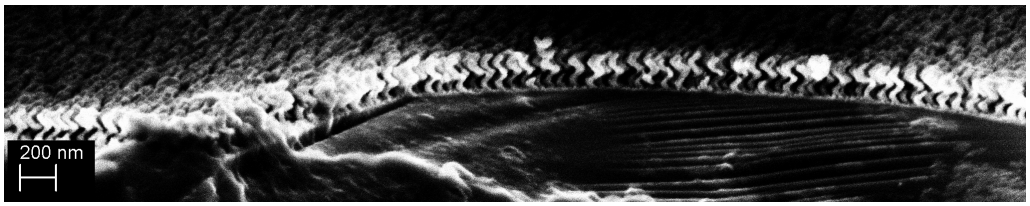

Figure 5.2: Tilted side view SEM showing a sample of GLAD nanohelices with Sm:Co=1:4.

5.2 Ferromagnetic nanohelices

In the GLAD chamber we are able to grow nanohelices with a broad range of materials. Also Ni, Co and Fe may be chosen, which are all in a ferromagnetic phase at standard conditions. In this section nanohelix arrays and magnetometry carried out on samples made of Co or co-deposited with Sm-Co and Ni.

5.2.1 Co and Sm-Co

It was attempted to fabricate a metamaterial of SmCo alloy which is known to have some of the strongest ferromagnetic coercivities [121], but unfortunately no evidence of the formation of the typical values of the strong ferromagnetic ordering of this alloy could be observed.

Figure 5.3 shows superconducting quantum interference device (SQUID) measurements carried out on two different samples with $h = 220\ nm$, $P = 145\ nm$, $a = 50\ nm$ and $r = 10\ nm$ grown on silicon substrates with Au BCML patterns. One of the samples is deposited with only Co, the other is the result of a co-evaporation of Sm and Co, with the ratio of co-evaporated material of Sm:Co=1:4. A side view of the sample deposited with the Sm-Co co-evaporation is shown in the SEM micrograph in Figure 5.2. As is possible to see from the comparison of the magnetization curve with the only Co nanohelices shown in Figure 5.3, the expected increase due to the

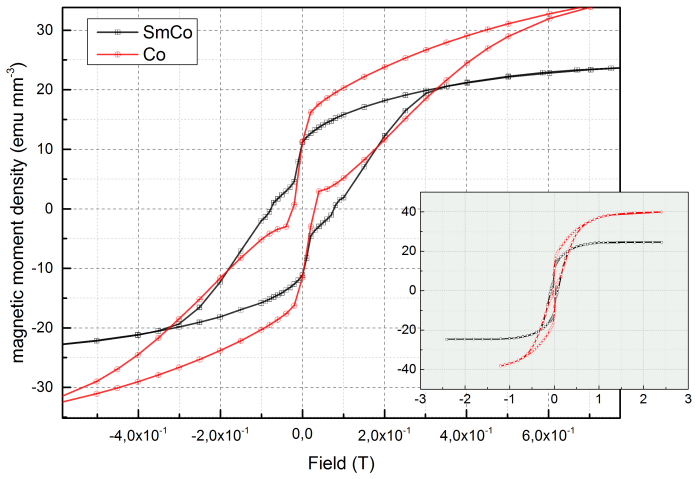

Figure 5.3: SQUID magnetometry measurements along the direction normal to the plane of the sample, showing the hysteresis curve of two samples coated with helix array metamaterial deposited with similar characteristics. Red data corresponds to a sample where the deposition was carried out with Co, while the black data corresponds to a sample where the deposition was carried out with a co-evaporation of Sm:Co=1:4. The main plot shows a magnified view of the magnetization curves for values of the external magnetic field below the saturating field. Saturation occurs at $\sim$ 0.35 T for SmCo and $\sim$ 0.70 T for Co.

co-evaporation of Sm-Co is not observed in the coercivity of the curve. The saturation magnetization density (m^{sat}) is reduced by $\frac{m^{sat}_{SmCo}}{m^{sat}_{Co}} \simeq 0.62$.

5.2.2 Nickel

As already anticipated, also Ni can be evaporated in the GLAD system which results in the growth of nanohelix arrays with good structures. Ni has been found to condense in smoother and more homogeneous structures when no nitrogen cooling of the substrate was adopted during the GLAD method.

As is clearly visible in the comparison of the resulting structures shown in Figure 5.4, when the deposition is carried out with cooling of the substrate this clearly deteriorates the resulting nanostructures.

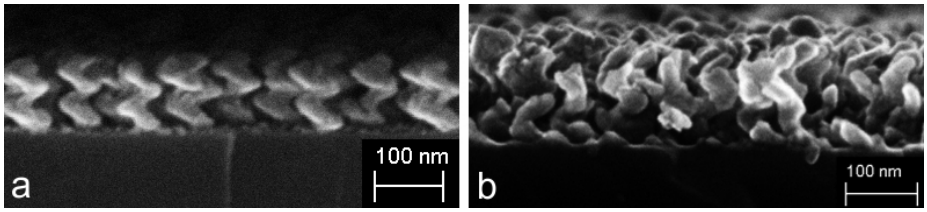

Figure 5.4: A comparison of the structural results of two samples with Ni nanohelices grown in the GLAD system. (a) liquid nitrogen cooling of the substrate is not adopted during deposition (b) liquid nitrogen cooling with the cooling being adopted during deposition.

Ni has proven to work so well in the GLAD system to permit a test of the limit of miniaturization. This resulted in the fabrication of the smallest nanohelix structure, with a pitch size of about $P \simeq 20\ nm$ which has been published in Ref. [10]. As a means of comparison the DNA double helix has a pitch length of its helical structure observed to be of about $\sim 3.4\ nm$ [122].

For the optical measurements two BCML patterned glass substrates (with Au nanodots of about 17 nm diameter with a spacing of about 75 nm) have been deposited with Ni nanohelix arrays, one left-handed $\mathscr{L}$ being the approximate enantiomer of the other, which is right-handed $\mathscr{R}$ and are both shown in Figure 5.5. The growth parameters of the two samples for the helices are identically set to $h = 100\ nm$, $P = 50\ nm$ but with the only difference of the rotation sense of the substrate holder during the deposition. Also a clean glass has been deposited with an unstructured bulk nickel film of the same thickness for comparison.

Oxidation of the nickel nanohelices has been found to be negligible, when all the other measurements shown in this chapter have been carried out over a period of several months. The magnitude and the spectral dependence of the optical absorption measurements (i.e. CD) were unchanged for repeated measurements during this time. A high-angle annular dark field scanning transmission microscopy (HAADF-STEM) of the samples is shown in Figure 5.5, detached from the substrate through a short process of ultrasound

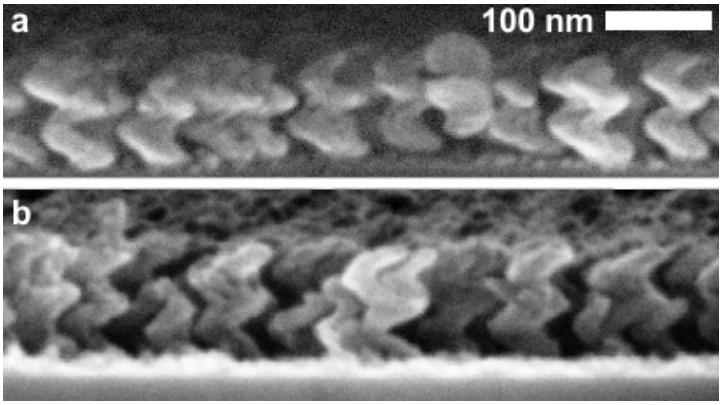

Figure 5.5: SEM side view picture of the two Ni nanohelix samples: (a) are left-handed, (b) are right-handed. Figure adapted and reprinted from [25].

sonication thanks to M. Alarcón-Correa. HAADF-STEM was performed thanks to T.C. Lee and the results can give precious information about the composition of the materials through the secondary emitted radiation using energy-dispersive X-ray analysis (STEM-edx). A typical result is shown in the false colour Figure 5.6, with the different materials marked with different colours: (Au) panel shows clearly the BCML gold nanodot where the structure has been grown, (Ti) shows the thin titanium layer deposited right before the deposition of the Ni, (O) shows the presence of oxigen, which seems only to cover the external shape of the nickel helix and finally (Ni) clearly identifies the predominance of nickel atoms forming the nanohelix shown in this image. For both $\mathscr{L}$ and $\mathscr{R}$ films a saturation field of $\sim 0.16\ T$ is observed, a saturation magnetization of 5×10^{-2}emu mm^{-3} and a coercive field of ~ 0.0140 T.

SQUID magnetometry of the samples has also been carried out. The magnetization curve acquired for the $\mathscr{L}$ is shown in Figure 5.7, which shows the typical hysteresis present in the ferromagnetic phase. The dimensions of an individual Ni structure are on the same order as the superparamagnetic domain size which leads to long, but finite, Néel relaxation times. Measurements of the remanent magnetization relaxation time shown in Figure 5.8 ($\tau \sim 1.5 \times 10^3$ s), suggest that the structures have a mean magnetic domain

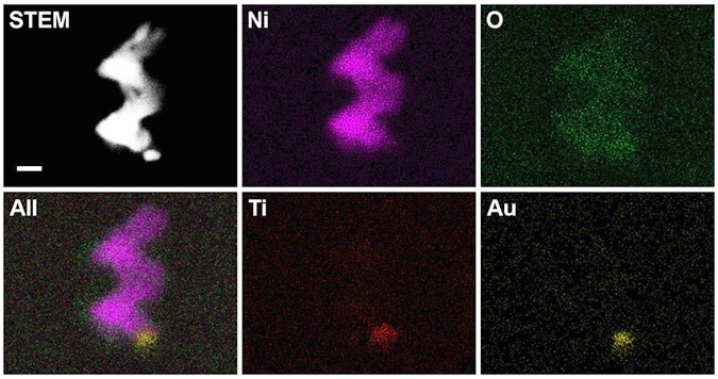

Figure 5.6: High-angle annular dark field scanning transmission electron microscope (HAADF STEM) image (top-left) of a typical Ni nanohelix and the corresponding false-color elemental maps obtained by STEM-edx spectral mapping, confirming all the intended elemental composition within the nanostructure. Scale bar = 20 nm. Figure adapted and reprinted from [25].

size of 18 nm according to the Néel-Arrhenius model. This agrees well with the measured helical wire diameter of $r \sim 20$ nm.

5.3 Optical absorption measurements

In this section are shown all the optical measurements in absorption of visible light, which is propagated on normal incidence on the nickel samples structured as arrays of nanohelices two turns in a film of about 100 nm and compared with an unstructured film of the same thickness, fabricated as described in the previous section. Independent measurements were carried out for each one of the contributions from the various effects underlined in Equation 5.2 for the dielectric constant of a magnetic and chiral metamaterial. The absorbance of each sample, $A(B = 0)$, necessary for calculating the g factors, was measured in transmission for unpolarized light using a Cary 4000 UV-VIS spectrometer. The unperturbed CD which corresponds to the NCD was measured in a standard JASCO 810 spectropolarimeter. Then MCD was obtained from measurements of the CD using an AVIV 42 MCD spectropolarimeter coupled to an Oxford Instruments Spectromag SM4000-10 in the group of Prof. van Slageren at the Univ. of Stuttgart

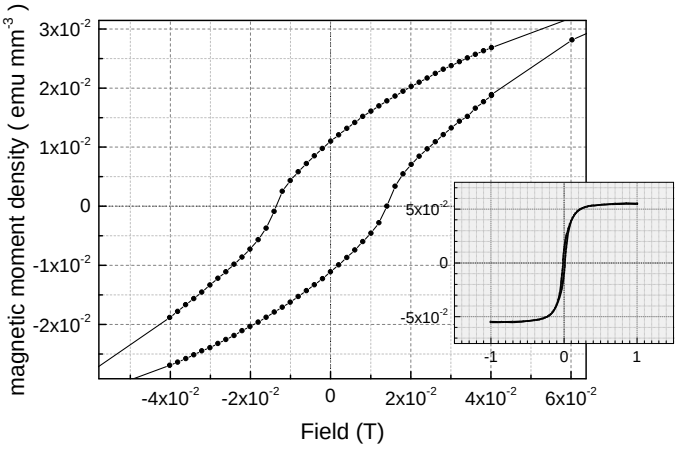

Figure 5.7: Magnetization curve measured parallel to the axis of the left handed nanohelices obtained with a SQUID magnetometer. The bottom-right inset shows the wide field magnetization curve with saturation at $\sim$ 0.16 T. Figure adapted and reprinted from [25].

together with Y. Rechkemmer, which provides magnetic fields from -10 T to $+10$ T along the direction of propagation of light. Finally direct measurements of the MChD acquired with a custom built setup can be compared with what is theoretically expected from the data of NCD and MCD for a cascaded cross effect of the two.

5.3.1 Unpolarized light absorbance and natural circular dichroism

The glass substrates with the deposited nickel films in the GLAD system were measured under normal incidence and the results are shown in Figure ??.

The NCD was measured with the JASCO 810 for $\mathscr{L}$ and $\mathscr{R}$ nanohelices and for the unstructured (plain) film made of nickel. Here a Hamamatsu R316 photomultiplier tube (PMT) was used as photodetector. The results are shown in Figure 5.10 in units of absorbance. As expected the $\mathscr{L}$ shows dominant LCP absorption and $\mathscr{R}$ shows dominant RCP absorption, while there is no NCD present in the unstructured film. The nickel nanohelices

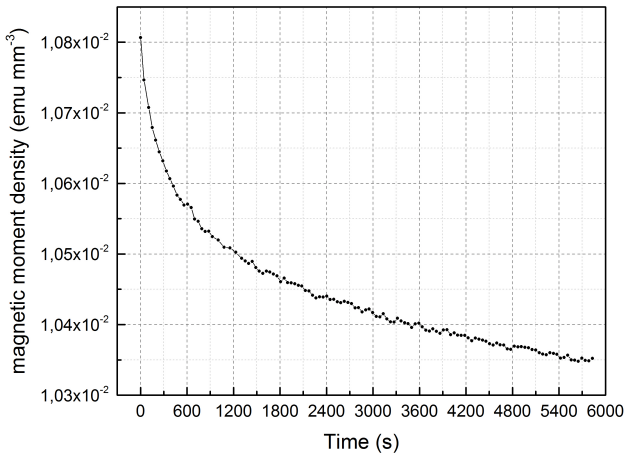

Figure 5.8: Magnetization relaxation measurement from the left handed nickel nanohelices in the SQUID magnetometer. A fit of the curve with the Néel-Arrhenius model suggests $\tau \sim 1.5 \times 10^3$ s and a corresponding magnetic domain size of 18 nm.

show a NCD peak which is as broad as the whole visible range. The magnitude of the optical activity can be compared directly with the measurements of the copper helices seen in the Chapters 2 and 4. In units of ellipticity the dominant absorption of LCP, for the $\mathscr{L}$ nickel helices at the wavelength of 570 nm is of 1319 mdeg. The corresponding peak of RCP for the $\mathscr{R}$ sample, is found at the wavelength of 545 nm and measures 1415 mdeg. This is about 4 times smaller in magnitude compared to the copper nanohelices already considered previously, but is still large compared to the CD observed for example in chiral molecules.

5.3.2 Magnetic circular dichroism

MCD is not sensitive to the chirality of the sample but only proportional to $\vec{B}$ and the CP of the electromagnetic wave. As the nickel samples are in a ferromagnetic phase and are immersed in an external magnetic field $\vec{H}$, the magnetization ($\vec{M}$) of the samples will generate a field which is $\vec{B} = \mu\vec{H}$, where μ is known as the magnetic permeability of the material. CD measurements are obtained from the AVIV 42 coupled to an Oxford Instruments

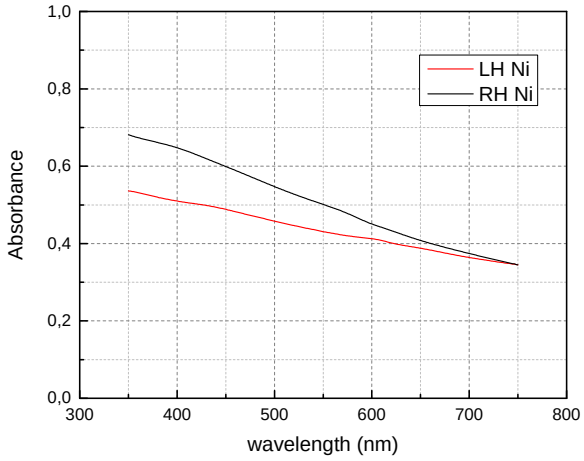

Figure 5.9: Absorbance of visible light at normal incidence on the two helical nanostructured nickel films, measured in the Cary 4000 UV-VIS spectrometer.

Spectromag SM4000-10. In Figure 5.11 are shown the CD spectra recorded from the unstructured nickel film as a function of the applied magnetic field. The CD from a material with chiral asymmetry will be a combination NCD + MCD. For the nickel nanohelices one has to subtract the NCD, in order to calculate the direct effect of MCD. In Figure 5.12 the MCD (in units of absorbance) for all three of the samples are shown; for clarity only the effects at the saturation and zero of $\vec{M}$ (-0.30 T, 0.00 T, $+0.30$T) are selected. In fact for any of the samples considered here, a positive field induces a positive contribution from the MCD to the whole CD, while a negative field induces a negative contribution. The slightly different magnitudes of the effect between the three samples is due to differences in the density, thickness and morphology of the films. Due to the strong absorption in the glass substrate measurements are restricted to $\lambda < 350$ nm.

5.3.3 Magneto-chiral dichroism

The magneto-chiral dichroism was measured using a custom setup depicted schematically in Figure 5.13. The monochromatic light from the Jasco 810c

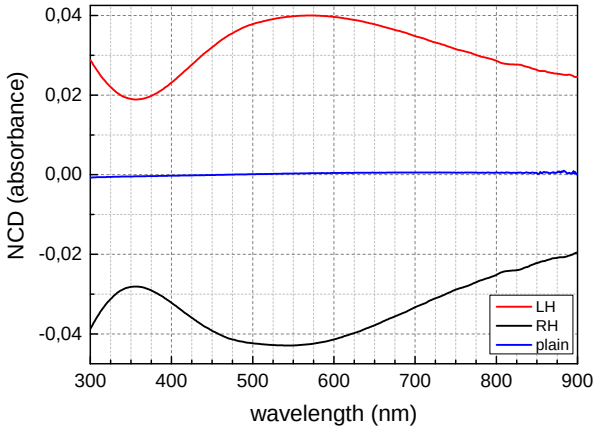

Figure 5.10: Natural circular dichroism spectra recorded under normal incidence on structured left (LH) and right (RH) handed 2-turn Ni nanohelices are shown in the red top curve and black bottom curve respectively, and an unstructured plain Ni film is shown as a control and shows no NCD as is expected. Figure adapted and reprinted from [25].

is depolarized and aligned in the central hole, which runs axially with respect to the of electrical windings from one side of an electromagnet. The electromagnet was built with copper wires windings around a double-E shaped ferrite core support (EPCOS PM 114/93). A central gap was created with a ring spacer at the centeral core of the ferrite magnet($\sim$ 2.3 mm), where a glass slide can be positioned so that is placed in the magnetic field and at the same time can be probed with the light which is aligned through the axial aperture in the ferrite core. The light propagated through the electromagnet is collected with a similar optical fiber bundle and redirected to the photomultiplier tube of the Jasco spectropolarimeter. The electrical current in the coils of the electromagnet is generated by a current amplifier (HUBERT AMP1250-16) which is driven by a 10Hz sinusoidal waveform generator (Hewlett Packard 33120A). The current running the electromagnets can be modulated as an AC magnetic field along the direction of propagation of the probing light with tunable amplitude proportional to the peak-to-peak voltage of the HP 33120A. The electromagnet has been found to be able to dissipate the heat in air, up to the magnetic fields of $\sim$ 0.3 T. For electrical

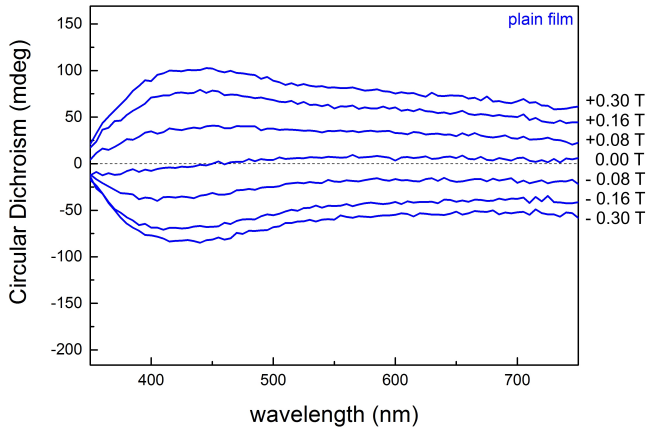

Figure 5.11: CD spectra recorded from the unstructured nickel film (plain) for external magnetic fields generated along the wave-vector of the propagated light. On the right side of the plot the amplitude of the external field is indicated.

currents required to generate fields of higher magnitude the temperature of the coils grows very rapidly compared the acquisition time typical for the measurement routine, in order to acquire MChD measurements at multiple wavelengths. Finally a Stanford Research lock-in amplifier (SR830) synchronized with the same signal of the HP 33120A, is used to detect the small difference of transmitted light being propagated parallel or antiparallel with respect to the magnetic field (T_ω), generated from the electromagnet, where the sample is positioned. In this way, the difference in absorbance called $MChD = A(\vec{B} \uparrow\uparrow \vec{k}) - A(\vec{B} \uparrow\downarrow \vec{k}))$ can be calculated.

If the effects are measured as difference in absorbance, it could be very challenging to make comparisons with other materials or between different effects. So if the absorbance differences are

$$NCD = CD(\vec{B} = 0) = A_- - A_+ \,, \tag{5.3}$$

$$MCD = CD(\vec{B}) - NCD \,, \tag{5.4}$$

$$MChD = A(\vec{B} \uparrow\uparrow \vec{k}) - A(\vec{B} \uparrow\downarrow \vec{k})) \tag{5.5}$$

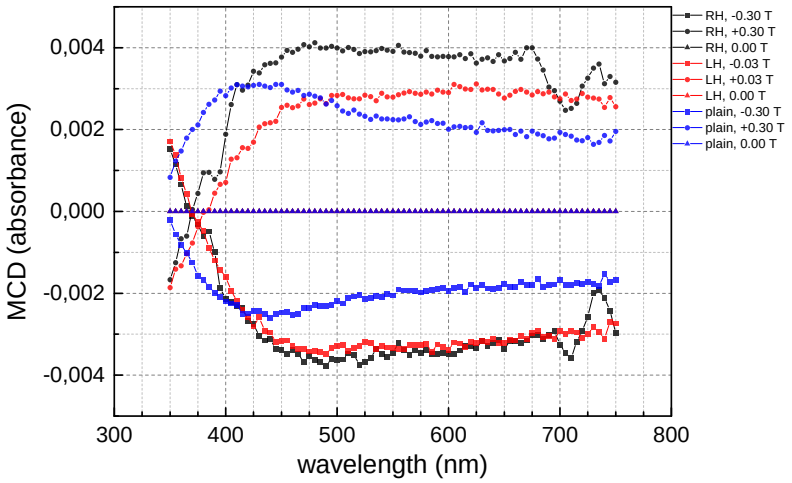

Figure 5.12: CD spectra recorded from the unstructured nickel film (plain) for external magnetic fields generated along the wave-vector of the propagated light. On the right side of the plot is indicated at the end of each curve the amplitude of the external field. Figure adapted and reprinted from [25].

then, a useful quantity that can be calculated is known as the dissimetry factor (g_{NCD}, g_{MCD}, g_{MChD}). If the unperturbed absorbance of unpolarized light is $A = \frac{A_-(\vec{B}=0)+A_+(\vec{B}=0)}{2}$, the anisotropy factors are defined as:

$$g_{NCD} = \frac{NCD}{A} , \tag{5.6}$$

$$\tag{5.7}$$

$$g_{MCD} = \frac{\partial}{\partial \vec{B}} \frac{MCD}{A} , \tag{5.8}$$

$$\tag{5.9}$$

$$g_{MChD} = \frac{\partial}{\partial \vec{B}} \frac{MChD}{A} . \tag{5.10}$$

No detailed theory exists to model magneto-chiral dichroism on metallic helices at optical wavelengths. Existing models for long wavelengths on metallic helices [123] or for free electrons on a helix [124] cannot account for the experimentally observed spectra. Yet it is useful to consider that to the general first-order approximation, it is expected that $g_{MChD} \approx \frac{1}{2}\, g_{NCD}\, g_{MCD}$ [116]. In Figure 5.14 the values of g_{MChD} calcu-

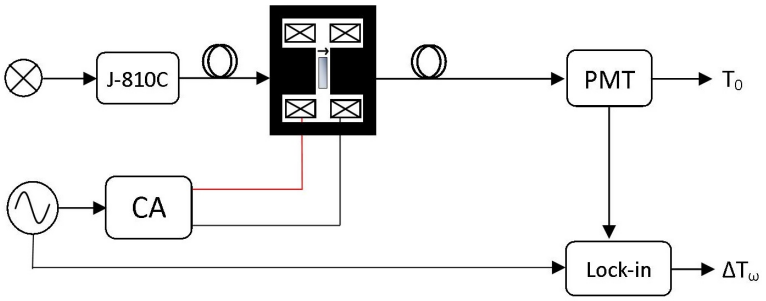

Figure 5.13: Schematics of the setup used for the magneto-chiral dichroism measurements.

lated from the direct measurements performed for the detection of MChD are shown and compared with the values calculated from the values obtained from g_{NCD} and g_{MCD}. It is remarkable that although the magnitude of the effect is consistent with the one expected from NCD and MCD, the wavelength of the actual MChD resonances are much shorter and are located in correspondence of the zero-crossing observed in the MCD spectra. As also previously discussed in Ref. [117], this is a confirmation that the pure MChD is observed here and not a cascaded effect. A slope of $g_{MChD} = (6.8 \pm 0.3) \times 10^{-4}$ T^{-1} at 380 nm for the RH helices and $g_{MChD} = (7.3 \pm 0.7) \times 10^{-4}$ T^{-1} for the LH helices. In term of absorption of light at the peak of the MChD resonances, this is about $\sim 10^{-4}$ the total absorbed light, but is detected in transmission through a metamaterial with a total thickness of 100 nm, at room temperature. Other MChD measurement have required the use of cryogenic equipment and about a hundred-fold stronger magnetic fields, yet the magnitude of the g_{MChD} is comparable with previous observations.

Regarding the nanohelices samples that have been produced with Co and SmCo, the MChD measurements show a slightly smaller effect. Figure 5.15 shows the results of the measurements of the MChD as recorded from the MChD setup as a comparison of the MChD present in the nickel nanohelix metamaterials. All the samples are left handed (LH) helices. However, with respect to the two turn nickel helices of 50 nm pitch, the cobalt and

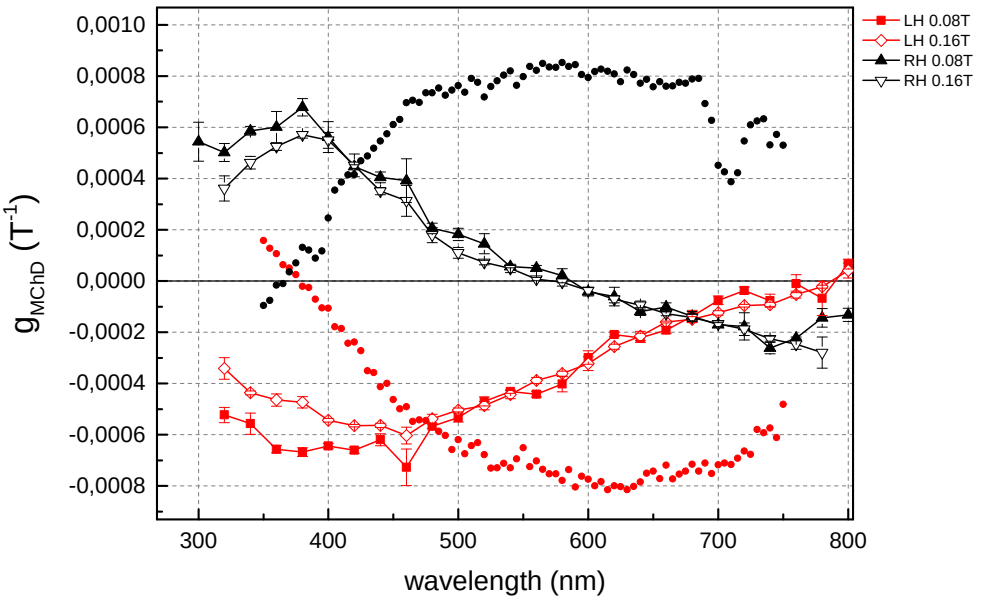

Figure 5.14: Dissimetry factor g_{MChD} calculated from the measurements carried out on left handed and right handed nickel nanohelices arrays coated on glass windows. The connected data points are the result of direct measurements, while the scattered points are theoretically calculated values from the measurements of NCD and MCD ($g_{MChD} \approx 1/2\ g_{NCD}\ g_{MCD}$). Figure reprinted from [25].

samarium cobalt samples are about $\sim$ 90 nm of pitch with one and half turns. This was necessary to red-shift the optical activity to the visible range for the cobalt based samples. However the g factors can still be compared as they are scaled to the total absorbances for each sample.

The difference between the different samples is clearly evident, which can at present not be quantitatively understood. There is no convincing explanation to the lack of MChD in the cobalt based samples. From a quantitative analysis of hysteresis curves, which were already shown in Figures 5.3 and 5.7, the saturation magnetization is just a little less than 10^3 times for the cobalt sample. Following the indication of the theory, also the MCD and MChD should be correspondingly larger with respect to the nickel sample, than what is measured (MCD spectra for the cobalt based

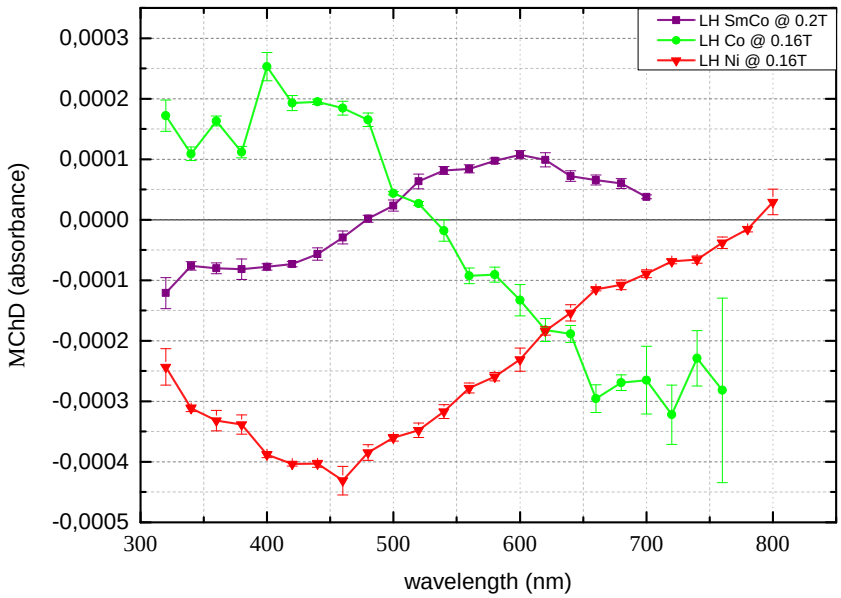

Figure 5.15: Results of the measurements carried on three different samples of nanohelix metamaterials deposited with glancing angle deposition method using nickel, cobalt and a coevaporation of samarium and cobalt. All the samples are lef handed (LH) helices, the pitch of the cobalt and samarium cobalt samples are about ~ 90 nm with one and half turns, this was necessay to red-shift the optical activity in the visible range.

samples are not shown here). Surprisingly the results of the measurements reveal a smaller effect in the cobalt sample, even though the magnetization and the magnetic susceptibility are about three orders of magnitude larger. If this was given by the larger coercive field in the cobalt based samples, this would in fact correspond to damping of the measured signal, which for low values of the external AC magnetic field, would correspond to an out of phase contribution to the detected T_ω. However, considering for example explicitly the ratio between the value of the coercive fields of the Co and Ni samples this results only $\sim$ 5 times larger in the case of the Co sample and therefore irrelevant compared to the magnetic susceptibility calculated at the saturation field for the two samples.

5.4 Final discussion

Chiral metamaterials deposited with GLAD have been demonstrated to be found in a ferromagnetic phase. In particular, nickel and cobalt nanohelix arrays have been designed to present strong NCD in transmission of visible light and measured with SQUID magnetometry to measure the magnetization curve in response to external magnetic fields, which reveals the presence of ferromagnetism. The combined presence of NCD and MCD have been observed in these hybrid chiral metamaterials. In presence of both of these optical activities, a higher order effect, the magneto-chiral optical activity is expected to be present. In particular, MChD in transmission of visible light was detected in metamaterials of nickel and cobalt at room temperature and using perturbing AC magnetic fields relatively limited in amplitude.

Chapter 6

Conclusion.

The optical activity of chiral metamaterials has been the main focus of this thesis. A unique glancing angle deposition method initially triggered the interest to explore the possibility to obtain metamaterials, with a very strong chiroptical response in the visible part of the electromagnetic spectrum. This method permits to process entire wafer-scale samples, which could be deposited with arrays of helices where the shape parameters and the chemical composition could be programmed.

The two orders of magnitude size difference existing between natural molecular dimensions and the wavelength of visible light could be filled with fabricated nanostructures and the observed strong, resonant optical response was discussed in terms of scattering of electromagnetic waves. In particular, the use of plasmonic metals was demonstrated to enhance the optical activity that could be present in macroscopic materials in the form of nanosculptured thin films or colloidal suspensions.

Standard techniques of chiroptical spectroscopy were adopted initially to measure the dependence on the circular polarization state of light in absorption. The physical role of structural chirality was considered, comparing the experimental results with results of a numerical method. The nanohelices' shape and dimension were demonstrated to determine directly the spectral dependence and the magnitude of the optical activity, due to the dispersive coupling of the plasmonic resonance.

Apart from the chiroptical response in absorption this thesis also explored the effect of chiral metamaterials on the real part of the index of refraction. This motivated the construction of a dedicated polarization laser interferometry setup, which could measure the index of refraction of chiral materials and the phase shift of left and right circularly polarized light components. In a uniaxial sample the circular birefringence as well as the absolute magnitude of the polarization-dependent refractive index components can be determined with the polarization interferometer. To test the interferometer, a cholesteric liquid crystal sample was examined and the measurements indicate a consistency with other experimental results and theoretical models.

The interferometer was then used to characterize the nanohelix metamaterial surfaces. Near the plasmon resonance the real part of the index of refraction becomes small, and this suggests that when the circular birefringence is large enough, the index of refraction could become negative for one of the two circular polarization components. To determine the small indices of refraction it became necessary to eliminate the contribution from the substrate on which the nanohelices are grown. This was achieved by using SiN windows. Silver nanohelices with 2 turns and an overall height of ~ 300 nm showed a plasmon resonance at ~ 633 nm. At this wavelength their circular birefringence was estimated to approach $\delta n' \simeq -1.3$. Near the plasmon resonance the real part of the refractive index of silver is only $n'_{Ag} \simeq 0.05$. This suggests that the index of refraction can be negative for a dense uniaxial film. Measurements from the interferometer indicate that under the approximation of uniaxiality the chiral metasurfaces can support a negative index of refraction. However, Muller matrix polarimetry measurements from a collaboration partner, showed that the surfaces are not uniaxial, but triclinic which complicates the analysis and does not permit the extraction of an overall index of refraction. In the future a finer tuning of the nanohelices will likely permit to produce a perfectly uniaxial metamaterial. Structural uniformity and stoichiometric control are most probably the

keys to reach this purpose. The use of other materials such as aluminium or alkali metals is also expected to increase the optical activity which could be used to obtain magnitudes higher than the thin film metamaterials considered in this thesis, to be then used then to obtain isotropical suspensions with negative index of refraction due to chirality.

Finally, chiral Ni nanohelices that were ferromagnetic at room temperature were fabricated. The simultaneous presence of natural optical activity and strong magnetic circular dichroism meant that the 100 nm thick chiral films also showed magnetochiral dichroism, which is otherwise a small effect. The chiral films showed the presence of a large band of MChD of $g_{MChD} \simeq 7 \times 10^{-4}$ around the wavelength of 400 nm.

Chiral nanohelix films give rise to large chiroptical effects in absorption and in refraction, and should permit the realization of a negative index medium due to chirality in the visible.

Bibliography

[1] W. T. B. Kelvin, *The molecular tactics of a crystal.* Clarendon Press, 1894.

[2] C.-S. Wu, E. Ambler, R. Hayward, D. Hoppes, and R. P. Hudson, "Experimental test of parity conservation in beta decay," *Physical review*, vol. 105, no. 4, p. 1413, 1957.

[3] J. H. Christenson, J. W. Cronin, V. L. Fitch, and R. Turlay, "Evidence for the 2 π decay of the k 2 0 meson," *Physical Review Letters*, vol. 13, no. 4, p. 138, 1964.

[4] W. A. Bonner, "Parity violation and the evolution of biomolecular homochirality," *Chirality*, vol. 12, no. 3, pp. 114–126, 2000.

[5] E. Ariens, "Stereochemistry, a basis for sophisticated nonsense in pharmacokinetics and clinical pharmacology," *European journal of clinical pharmacology*, vol. 26, no. 6, pp. 663–668, 1984.

[6] E. G. DeVita, M. Miao, and A. A. Sadun, "Optic neuropathy in ethambutol-treated renal tuberculosis.," *Journal of Neuro-Ophthalmology*, vol. 7, no. 2, pp. 77–83, 1987.

[7] L. D. Barron, *Molecular light scattering and optical activity.* Cambridge University Press, 2004.

[8] H. C. Hulst, *Light scattering by small particles.* Courier Corporation, 1957.

[9] A. G. Mark, J. G. Gibbs, T.-C. Lee, and P. Fischer, "Hybrid nanocolloids with programmed three-dimensional shape and material composition," *Nature materials*, vol. 12, no. 9, pp. 802–807, 2013.

[10] J. G. Gibbs, A. G. Mark, T.-C. Lee, S. Eslami, D. Schamel, and P. Fischer, "Nanohelices by shadow growth," *Nanoscale*, 2014.

[11] A. Fang, S. White, P. K. Jain, and F. P. Zamborini, "Regioselective plasmonic coupling in metamolecular analogs of benzene derivatives," *Nano letters*, vol. 15, no. 1, pp. 542–548, 2014.

[12] N. Engheta and R. W. Ziolkowski, *Metamaterials: physics and engineering explorations*. John Wiley & Sons, 2006.

[13] S. Link and M. A. El-Sayed, "Spectral properties and relaxation dynamics of surface plasmon electronic oscillations in gold and silver nanodots and nanorods," *The Journal of Physical Chemistry B*, vol. 103, no. 40, pp. 8410–8426, 1999.

[14] N. Ashcroft and N. Mermin, *Solid State Physics (Brooks Cole, 1976)*.

[15] M. Quinten, *Optical properties of nanoparticle systems: Mie and beyond*. John Wiley & Sons, 2010.

[16] A. Yurtsever, R. M. van der Veen, and A. H. Zewail, "Subparticle ultrafast spectrum imaging in 4d electron microscopy," *Science*, vol. 335, no. 6064, pp. 59–64, 2012.

[17] L. Novotny and N. Van Hulst, "Antennas for light," *Nature Photonics*, vol. 5, no. 2, pp. 83–90, 2011.

[18] J. A. Scholl, A. L. Koh, and J. A. Dionne, "Quantum plasmon resonances of individual metallic nanoparticles," *Nature*, vol. 483, no. 7390, pp. 421–427, 2012.

[19] H. A. Atwater and A. Polman, "Plasmonics for improved photovoltaic devices," *Nature materials*, vol. 9, no. 3, pp. 205–213, 2010.

[20] H. Xu, E. J. Bjerneld, M. Käll, and L. Börjesson, "Spectroscopy of single hemoglobin molecules by surface enhanced raman scattering," *Physical review letters*, vol. 83, no. 21, p. 4357, 1999.

[21] G. Kucsko, P. Maurer, N. Y. Yao, M. Kubo, H. Noh, P. Lo, H. Park, and M. D. Lukin, "Nanometre-scale thermometry in a living cell," *Nature*, vol. 500, no. 7460, pp. 54–58, 2013.

[22] J. Pendry, "A chiral route to negative refraction," *Science*, vol. 306, no. 5700, pp. 1353–1355, 2004.

[23] J. Gibbs, A. Mark, S. Eslami, and P. Fischer, "Plasmonic nanohelix metamaterials with tailorable giant circular dichroism," *Applied Physics Letters*, vol. 103, no. 21, p. 213101, 2013.

[24] A. Sanchez-Castillo, S. Eslami, F. Giesselmann, and P. Fischer, "Circular polarization interferometry: circularly polarized modes of cholesteric liquid crystals," *Optics express*, vol. 22, no. 25, pp. 31227–31236, 2014.

[25] S. Eslami, J. G. Gibbs, Y. Rechkemmer, J. van Slageren, M. Alarcón-Correa, T.-C. Lee, A. G. Mark, G. L. Rikken, and P. Fischer, "Chiral nanomagnets," *ACS Photonics*, 2014.

[26] D. J. Griffiths and R. College, *Introduction to electrodynamics*, vol. 3. prentice Hall Upper Saddle River, NJ, 1999.

[27] P. J. Mohr, B. N. Taylor, and D. B. Newell, "Codata recommended values of the fundamental physical constants: 2010a)," *Journal of Physical and Chemical Reference Data*, vol. 41, no. 4, p. 043109, 2012.

[28] A. Lakhtakia, *Beltrami fields in chiral media*, vol. 2. World Scientific, 1994.

[29] B. D. Tellegen, "The gyrator, a new electric network element," *Philips Res. Rep*, vol. 3, no. 2, pp. 81–101, 1948.

[30] A. Karlsson and G. Kristensson, "Constitutive relations, dissipation, and reciprocity for the maxwell equations in the time domain," *Journal of Electromagnetic Waves and Applications*, vol. 6, no. 5-6, pp. 537–551, 1992.

[31] I. V. Lindell, A. Sihvola, S. Tretyakov, and A. Viitanen, "Electromagnetic waves in chiral and bi-isotropic media," 1994.

[32] D. Sarid and W. Challener, *Modern introduction to surface plasmons: theory, Mathematica modeling, and applications*. Cambridge University Press, 2010.

[33] E. Hecht, "Optics 4th edition," *Optics, 4th Edition, Addison Wesley Longman Inc, 1998*, vol. 1, 1998.

[34] M. Born and E. Wolf, *Principles of Optics, 7th (expanded) ed.* Cambridge U. Press, 1999.

[35] P. E. Ciddor, "Refractive index of air: new equations for the visible and near infrared," *Applied optics*, vol. 35, no. 9, pp. 1566–1573, 1996.

[36] P. E. Ciddor and R. J. Hill, "Refractive index of air. 2. group index," *Applied Optics*, vol. 38, no. 9, pp. 1663–1667, 1999.

[37] P. E. Ciddor, "Refractive index of air: 3. the roles of co 2, h 2 o, and refractivity virials," *Applied optics*, vol. 41, no. 12, pp. 2292–2298, 2002.

[38] M. Polyanskiy, "Refractive index database, http://refractiveindex.info," 2016.

[39] A. D. Rakić, A. B. Djurišić, J. M. Elazar, and M. L. Majewski, "Optical properties of metallic films for vertical-cavity optoelectronic devices," *Applied optics*, vol. 37, no. 22, pp. 5271–5283, 1998.

[40] R. Brendel and D. Bormann, "An infrared dielectric function model for amorphous solids," *Journal of applied physics*, vol. 71, no. 1, pp. 1–6, 1992.

[41] B. Dold and R. Mecke, "Optische eigenschaften von edelmetallen ubergangsmetallen und deren legierungen im infrarot. 1.," *Optik*, vol. 22, no. 6, p. 435, 1965.

[42] P. Winsemius, H. Lengkeek, and F. Van Kampen, "Structure dependence of the optical properties of cu, ag and au," *Physica B+ C*, vol. 79, no. 6, pp. 529–546, 1975.

[43] G. Leveque, C. Olson, and D. W. Lynch, "Reflectance spectra and dielectric functions for ag in the region of interband transitions," *Physical Review B*, vol. 27, no. 8, p. 4654, 1983.

[44] C. Meierbachtol, "Permittivity of metals at optical wavelengths (brendel-bormann)," *publicly available code at MATLAB central file exchange: http://www.mathworks.com/matlabcentral/fileexchange/26025-permittivity-of-metals-at-optical-wavelengths–brendel-bormann-*, 2009.

[45] E. D. Palik, *Handbook of optical constants of solids*, vol. 3. Academic press, 1998.

[46] P. B. Johnson and R.-W. Christy, "Optical constants of the noble metals," *Physical Review B*, vol. 6, no. 12, p. 4370, 1972.

[47] G. Mie, "Beiträge zur optik trüber medien, speziell kolloidaler metallösungen," *Annalen der physik*, vol. 330, no. 3, pp. 377–445, 1908.

[48] R. L. Lee, "Mie theory, airy theory, and the natural rainbow," *Applied Optics*, vol. 37, no. 9, pp. 1506–1519, 1998.

[49] J. S. Marshall and W. M. K. Palmer, "The distribution of raindrops with size," *Journal of meteorology*, vol. 5, no. 4, pp. 165–166, 1948.

[50] B. T. Draine and P. J. Flatau, "The discrete-dipole approximation and its application to interstellar graphite grains," *The Astrophysical Journal*, vol. 333, pp. 848–872, 1988.

[51] B. T. Draine and P. J. Flatau, "Discrete-dipole approximation for scattering calculations," *JOSA A*, vol. 11, no. 4, pp. 1491–1499, 1994.

[52] B. T. Draine and P. J. Flatau, "User guide for the discrete dipole approximation code ddscat 7.2," *ArXiv.org*, 2012.

[53] B. T. Draine and J. Goodman, "Beyond clausius-mossotti-wave propagation on a polarizable point lattice and the discrete dipole approximation," *The Astrophysical Journal*, vol. 405, pp. 685–697, 1993.

[54] J. Goodman, P. Flatau, and B. Draine, "Application of fast-fourier-transform techniques to the discrete-dipole approximation," *Optics Letters*, vol. 16, no. 15, pp. 1198–1200, 1991.

[55] M. T. Taschuk, M. M. Hawkeye, and M. J. Brett, "Glancing angle deposition," *Handbook of Deposition Technologies for Films and Coatings*, pp. 621–678, 2010.

[56] A. Kundt, "Ueber doppelbrechung des lichtes in metallschichten, welche durch zerstäuben einer kathode hergestellt sind," *Annalen der Physik*, vol. 263, no. 1, pp. 59–71, 1886.

[57] F. Kaempf, "Größe und ursache der doppelbrechung in kundtschen spiegeln und erzeugung von doppelbrechung in metallspiegeln durch zug," *Annalen der Physik*, vol. 321, no. 2, pp. 308–333, 1905.

[58] D. Vick, L. Friedrich, S. Dew, M. Brett, K. Robbie, M. Seto, and T. Smy, "Self-shadowing and surface diffusion effects in obliquely deposited thin films," *Thin Solid Films*, vol. 339, no. 1, pp. 88–94, 1999.

[59] R. Glass, M. Möller, and J. P. Spatz, "Block copolymer micelle nanolithography," *Nanotechnology*, vol. 14, no. 10, p. 1153, 2003.

[60] M. Schäferling, D. Dregely, M. Hentschel, and H. Giessen, "Tailoring enhanced optical chirality: design principles for chiral plasmonic nanostructures," *Physical Review X*, vol. 2, no. 3, p. 031010, 2012.

[61] N. Liu, H. Liu, S. Zhu, and H. Giessen, "Stereometamaterials," *Nature Photonics*, vol. 3, no. 3, pp. 157–162, 2009.

[62] Y. Zhao, M. Belkin, and A. Alù, "Twisted optical metamaterials for planarized ultrathin broadband circular polarizers," *Nature communications*, vol. 3, p. 870, 2012.

[63] M. Hentschel, M. Scha ferling, T. Weiss, N. Liu, and H. Giessen, "Three-dimensional chiral plasmonic oligomers," *Nano letters*, vol. 12, no. 5, pp. 2542–2547, 2012.

[64] J. K. Gansel, M. Thiel, M. S. Rill, M. Decker, K. Bade, V. Saile, G. von Freymann, S. Linden, and M. Wegener, "Gold helix photonic metamaterial as broadband circular polarizer," *Science*, vol. 325, no. 5947, pp. 1513–1515, 2009.

[65] Z.-Y. Zhang and Y.-P. Zhao, "Optical properties of helical and multiring ag nanostructures: The effect of pitch height," *Journal of Applied Physics*, vol. 104, no. 1, p. 013517, 2008.

[66] J. K. Gansel, M. Wegener, S. Burger, and S. Linden, "Gold helix photonic metamaterials: a numerical parameter study," *Optics express*, vol. 18, no. 2, pp. 1059–1069, 2010.

[67] L. Wu, Z. Yang, M. Zhao, P. Zhang, Z. Lu, Y. Yu, S. Li, and X. Yuan, "What makes single-helical metamaterials generate "pure" circularly polarized light?," *Optics express*, vol. 20, no. 2, pp. 1552–1560, 2012.

[68] M. M. Hawkeye and M. J. Brett, "Glancing angle deposition: Fabrication, properties, and applications of micro-and nanostructured thin films," *Journal of Vacuum Science & Technology A*, vol. 25, no. 5, pp. 1317–1335, 2007.

[69] C. M. Soukoulis and M. Wegener, "Materials science. optical metamaterials–more bulky and less lossy.," *Science*, vol. 330, pp. 1633–1634, Dec 2010.

[70] B. Luk'yanchuk, N. I. Zheludev, S. A. Maier, N. J. Halas, P. Nordlander, H. Giessen, and C. T. Chong, "The fano resonance in plasmonic nanostructures and metamaterials.," *Nat Mater*, vol. 9, pp. 707–715, Sep 2010.

[71] J. B. Lassiter, H. Sobhani, J. A. Fan, J. Kundu, F. Capasso, P. Nordlander, and N. J. Halas, "Fano resonances in plasmonic nanoclusters: geometrical and chemical tunability.," *Nano Lett*, vol. 10, pp. 3184–3189, Aug 2010.

[72] M. V. Gorkunov, V. E. Dmitrienko, A. A. Ezhov, V. V. Artemov, and O. Y. Rogov, "Implications of the causality principle for ultra chiral metamaterials," *Scientific reports*, vol. 5, 2015.

[73] J. Jamin, "Neuer interferential-refractor," *Ann. Phys*, vol. 98, pp. 345–349, 1856.

[74] M. Françon, "Optical interferometry," in *Neutron interferometry*, 1979.

[75] D. G. Stavenga, H. L. Leertouwer, and B. D. Wilts, "Quantifying the refractive index dispersion of a pigmented biological tissue using jamin–lebedeff interference microscopy," *Light: Science & Applications*, vol. 2, no. 9, p. e100, 2013.

[76] F. Schäfer and W. Kleemann, "High-precision refractive index measurements revealing order parameter fluctuations in kmnf3 and nio," *Journal of applied physics*, vol. 57, no. 7, pp. 2606–2612, 1985.

[77] V. Drachev, W. Cai, U. Chettiar, H.-K. Yuan, A. Sarychev, A. Kildishev, G. Klimeck, and V. Shalaev, "Experimental verification of an optical negative-index material," *Laser Physics Letters*, vol. 3, no. 1, pp. 49–55, 2006.

[78] P. Yeh, *Optical waves in layered media*, vol. 95. Wiley New York, 1988.

[79] M. Pfeifer, *Novel Approaches to Optical Activity Measurements*. Cuvillier, E, 2014.

[80] P. C. Logofatu, "Simple method for determining the fast axis of a wave plate," *Optical Engineering*, vol. 41, no. 12, pp. 3316–3318, 2002.

[81] G. Galgano and A. Henriques, "Determining the fast axis of a wave plate," *Proceedings do ENFMC*, 2006.

[82] M. Evans, R. Moutran, and A. H. Price, "Dielectric properties, refractive index and far infrared spectrum of cholesteryl oleyl carbonate," *Journal of the Chemical Society, Faraday Transactions 2: Molecular and Chemical Physics*, vol. 71, pp. 1854–1862, 1975.

[83] R. Somashekar and D. Krishnamurti, "Optical anisotropy of cholesteryl oleyl carbonate," *Molecular Crystals and Liquid Crystals*, vol. 84, no. 1, pp. 31–37, 1982.

[84] P. Oswald and P. Pieranski, *Nematic and cholesteric liquid crystals: concepts and physical properties illustrated by experiments*. CRC press, 2005.

[85] H. de Vries, "Rotatory power and other optical properties of certain liquid crystals," *Acta Crystallographica*, vol. 4, no. 3, pp. 219–226, 1951.

[86] H. Stegemeyer and K.-J. Mainusch, "Optical rotatory power of liquid crystal mixtures," *Chemical Physics Letters*, vol. 6, no. 1, pp. 5–6, 1970.

[87] L. Melamed and D. Rubin, "Selected optical properties of mixtures of cholesteric liquid crystals," *Applied optics*, vol. 10, no. 5, pp. 1103–1107, 1971.

[88] R. Ennulat, "The selective light reflection by plane textures," *Molecular Crystals and Liquid Crystals*, vol. 13, no. 4, pp. 337–355, 1971.

[89] C. Kim, K. L. Marshall, J. U. Wallace, and S. H. Chen, "Photochromic glassy liquid crystals comprising mesogenic pendants to dithienylethene cores," *J. Mater. Chem.*, vol. 18, no. 46, pp. 5592–5598, 2008.

[90] V. Belyakov, V. E. Dmitrienko, and V. Orlov, "Optics of cholesteric liquid crystals," *Soviet Physics Uspekhi*, vol. 22, no. 2, p. 64, 1979.

[91] S. Chandrasekhar, *Liquid Crystals*. Cambridge University Press, 1992.

[92] P. De Gennes and J. Prost, "The physics of liquid crystals, 1993," *Oxford University Press, New York, Olbrich E., Marinov O., Davidov D., Phys. Rev. E*, vol. 2713, p. 48, 1993.

[93] P. Yeh and C. Gu, *Optics of liquid crystal displays*, vol. 67. John Wiley & Sons, 2010.

[94] V. G. Veselago, "The electrodynamics of substances with simultaneously negative values of img align= absmiddle alt= eps/img and μ," *Physics-Uspekhi*, vol. 10, no. 4, pp. 509–514, 1968.

[95] R. A. Shelby, D. R. Smith, and S. Schultz, "Experimental verification of a negative index of refraction," *science*, vol. 292, no. 5514, pp. 77–79, 2001.

[96] B. Wang, J. Zhou, T. Koschny, and C. M. Soukoulis, "Nonplanar chiral metamaterials with negative index," *Applied Physics Letters*, vol. 94, no. 15, p. 151112, 2009.

[97] P. Dolganov, G. Ksyonz, V. Dmitrienko, and V. Dolganov, "Description of optical properties of cholesteric photonic liquid crystals based on maxwell equations and kramers-kronig relations," *Physical Review E*, vol. 87, no. 3, p. 032506, 2013.

[98] K. M. McPeak, S. V. Jayanti, S. J. Kress, S. Meyer, S. Iotti, A. Rossinelli, and D. J. Norris, "Plasmonic films can easily be better: rules and recipes," *ACS photonics*, vol. 2, no. 3, pp. 326–333, 2015.

[99] G. K. Larsen, Y. He, J. Wang, and Y. Zhao, "Scalable fabrication of composite ti/ag plasmonic helices: Controlling morphology and optical activity by tailoring material properties," *Advanced Optical Materials*, vol. 2, no. 3, pp. 245–249, 2014.

[100] M. Decker, M. Ruther, C. Kriegler, J. Zhou, C. Soukoulis, S. Linden, and M. Wegener, "Strong optical activity from twisted-cross photonic metamaterials," *Optics letters*, vol. 34, no. 16, pp. 2501–2503, 2009.

[101] M. Decker, R. Zhao, C. Soukoulis, S. Linden, and M. Wegener, "Twisted split-ring-resonator photonic metamaterial with huge optical activity," *Optics letters*, vol. 35, no. 10, pp. 1593–1595, 2010.

[102] M. Gorkunov, A. Ezhov, V. Artemov, O. Rogov, and S. Yudin, "Extreme optical activity and circular dichroism of chiral metal hole arrays," *Applied Physics Letters*, vol. 104, no. 22, p. 221102, 2014.

[103] Z.-Y. Zhang and Y.-P. Zhao, "Optical properties of helical ag nanostructures calculated by discrete dipole approximation method," *Applied physics letters*, vol. 90, no. 22, p. 221501, 2007.

[104] O. Arteaga, J. Freudenthal, B. Wang, and B. Kahr, "Mueller matrix polarimetry with four photoelastic modulators: theory and calibration," *Applied optics*, vol. 51, no. 28, pp. 6805–6817, 2012.

[105] M. Hehn, K. Ounadjela, J.-P. Bucher, F. Rousseaux, D. Decanini, B. Bartenlian, and C. Chappert, "Nanoscale magnetic domains in mesoscopic magnets," *Science*, vol. 272, no. 5269, pp. 1782–1785, 1996.

[106] T. Shinjo, T. Okuno, R. Hassdorf, K. Shigeto, and T. Ono, "Magnetic vortex core observation in circular dots of permalloy," *Science*, vol. 289, no. 5481, pp. 930–932, 2000.

[107] R. Cowburn, D. Koltsov, A. Adeyeye, M. Welland, and D. Tricker, "Single-domain circular nanomagnets," *Physical Review Letters*, vol. 83, no. 5, p. 1042, 1999.

[108] Z. Pirzadeh, T. Pakizeh, V. Miljkovic, C. Langhammer, and A. Dmitriev, "Plasmon–interband coupling in nickel nanoantennas," *ACS Photonics*, vol. 1, no. 3, pp. 158–162, 2014.

[109] J. Chen, P. Albella, Z. Pirzadeh, P. Alonso-González, F. Huth, S. Bonetti, V. Bonanni, J. Åkerman, J. Nogués, P. Vavassori, *et al.*, "Plasmonic nickel nanoantennas," *Small*, vol. 7, no. 16, pp. 2341–2347, 2011.

[110] G. Rikken and E. Raupach, "Observation of magneto-chiral dichroism," *Nature*, vol. 390, no. 6659, pp. 493–494, 1997.

[111] A. Kuzyk, R. Schreiber, Z. Fan, G. Pardatscher, E.-M. Roller, A. Högele, F. C. Simmel, A. O. Govorov, and T. Liedl, "Dna-based self-assembly of chiral plasmonic nanostructures with tailored optical response," *Nature*, vol. 483, no. 7389, pp. 311–314, 2012.

[112] G. Larsen, Y. He, W. Ingram, E. LaPaquette, J. Wang, and Y.-P. Zhao, "The fabrication of three-dimensional plasmonic chiral structures by dynamic shadowing growth," *Nanoscale*, 2014.

[113] M. Schäferling, X. Yin, N. Engheta, and H. Giessen, "Helical plasmonic nanostructures as prototypical chiral near-field sources," *ACS Photonics*, 2014.

[114] Z. Fan and A. O. Govorov, "Plasmonic circular dichroism of chiral metal nanoparticle assemblies," *Nano letters*, vol. 10, no. 7, pp. 2580–2587, 2010.

[115] Z. Fan and A. O. Govorov, "Helical metal nanoparticle assemblies with defects: plasmonic chirality and circular dichroism," *The Journal of Physical Chemistry C*, vol. 115, no. 27, pp. 13254–13261, 2011.

[116] N. Berova, P. L. Polavarapu, K. Nakanishi, and R. W. Woody, *Comprehensive Chiroptical Spectroscopy: Instrumentation, Methodologies, and Theoretical Simulations, Vol. 1.* John Wiley & Sons, Inc., Hoboken, NJ, 2012.

[117] G. Rikken and E. Raupach, "Pure and cascaded magnetochiral anisotropy in optical absorption," *Physical Review E*, vol. 58, no. 4, p. 5081, 1998.

[118] C. Train, R. Gheorghe, V. Krstic, L.-M. Chamoreau, N. S. Ovanesyan, G. L. Rikken, M. Gruselle, and M. Verdaguer, "Strong magneto-chiral dichroism in enantiopure chiral ferromagnets," *Nature materials*, vol. 7, no. 9, pp. 729–734, 2008.

[119] M. Saito, K. Ishikawa, K. Taniguchi, and T. Arima, "Magnetic control of crystal chirality and the existence of a large magneto-optical dichroism effect in cub 2 o 4," *Physical review letters*, vol. 101, no. 11, p. 117402, 2008.

[120] A. Christofi and N. Stefanou, "Strong magnetochiral dichroism of helical structures of garnet particles," *Optics letters*, vol. 38, no. 22, pp. 4629–4631, 2013.

[121] C. Prados, A. Hernando, G. Hadjipanayis, and J. Gonzalez, "Coercivity analysis in sputtered sm–co thin films," *Journal of applied physics*, vol. 85, no. 8, pp. 6148–6150, 1999.

[122] S. Lindsay, T. Thundat, L. Nagahara, U. Knipping, and R. Rill, "Images of the dna double helix in water," *Science*, vol. 244, no. 4908, pp. 1063–1064, 1989.

[123] G. Rikken, J. Fölling, and P. Wyder, "Electrical magnetochiral anisotropy," *Physical review letters*, vol. 87, no. 23, p. 236602, 2001.

[124] G. H. Wagnière and G. L. Rikken, "Chirality and magnetism: Free electron on an infinite helix, ncd, mcd, and magnetochiral dichroism," *Chemical Physics Letters*, vol. 481, no. 4, pp. 166–168, 2009.